PAPER • **OPEN ACCESS**

Interaction of SPI pellets with plasma on JET and associated disruptions

To cite this article: S N Gerasimov *et al* 2024 *Phys. Scr.* **99** 075615

Physica Scripta

PAPER

Interaction of SPI pellets with plasma on JET and associated disruptions

OPEN ACCESS

RECEIVED
28 March 2024

REVISED
2 June 2024

ACCEPTED FOR PUBLICATION
7 June 2024

PUBLISHED
25 June 2024

S N Gerasimov[1], L R Baylor[2], A Boboc[1], I S Carvalho[3], P Carvalho[1], I H Coffey[1,4], D Craven[1], J Flanagan[1], A Huber[5], V Huber[6], S Jachmich[3], I Jepu[1], E Joffrin[7], D Kos[1], S I Krasheninnikov[8], U Kruezi[3], M Lehnen[3], P J Lomas[1], A Manzanares[9], M Maslov[1], A Peacock[1], P Puglia[1], F G Rimini[1], G Sergienko[5], D Shiraki[2], S Silburn[1], R D Smirnov[8], C Stuart[1], H Sun[1], J Wilson[1], L E Zakharov[10,11] JET Contributors[12]

[1] UKAEA, Culham Campus, Abingdon, Oxon, OX14 3DB, United Kingdom
[2] Oak Ridge National Laboratory, Oak Ridge, TN 37831, United States of America
[3] ITER Organization, Route de Vinon, CS 90 046, 13067 Saint Paul Lez Durance, France
[4] Astrophysics Research Centre, Queen's University, Belfast, BT7 1NN, United Kingdom
[5] Forschungszentrum Jülich GmbH, Institut für Energie- und Klimaforschung-Plasmaphysik, Partner of the Trilateral Euregio Cluster (TEC), 52425 Jülich, Germany
[6] Jülich Supercomputing Centre, Forschungszentrum Jülich, 52425 Jülich, Germany
[7] CEA, IRFM, F-13108 Saint-Paul-lez-Durance, France
[8] Department of Mechanical and Aerospace Engineering, University of California San Diego, La Jolla, CA 92093, United States of America
[9] Laboratorio Nacional de Fusión, CIEMAT, 28040 Madrid, Spain
[10] LiWFusion PO Box 2391, Princeton NJ 08543, United States of America
[11] Department of Physics, University of Helsinki, PO Box 43, FIN - 00014, Finland
[12] See 'Overview of JET results for optimizing ITER operation' by Mailloux *et al*, to be published in Nucl. Fus. Special Issue for 28th Fusion Energy Conference (2021), Mailloux et al 2022 (https://doi.org/10.1088/1741-4326/ac47b4) for the JET Contributors.

E-mail: Sergei.Gerasimov@ukaea.uk

Keywords: tokamak, disruption, shattered pellet, VDE

Abstract

The presented data refer to the Shattered Pellet Injector (SPI) experiments carried out at JET in 2019–2020. This paper is a full journal version of the data originally presented as posters at TMPDM_2020 and EPS_2021. This paper presents various aspects of the interaction of pellets with plasma and associated disruptions. The experiment was performed with $I_p = (1.1–3.1)$ MA plasmas and mainly with Ne + D_2 pellet composition, but also with Ar pellets. The Current Quench (CQ) time, τ_{80-20}, is the key characteristic of mitigation effectiveness. A pellet with a high content of Ne or Ar can reduce the CQ duration below the upper required JET threshold. Plasmas with high (thermal + internal poloidal magnetic) pre-disruptive plasma energy require a high content of Ne pellets to obtain a short CQ duration. Pellets with a small amount of Ne (and accordingly large amount of D), instead of causing a mitigated CQ, create the conditions for a 'cold' Vertical Displacement Events (VDE). The SPI was applied to plasma with different status: mainly to normal ('healthy') plasma, i.e. not prone to disruption, post-disruptive and VDE plasma. This study shows that SPI effectiveness in terms of CQ duration and, accordingly, EM loads does not depend on the state of the plasma, whether it is 'healthy' or post-disruptive plasma. SPI has been shown to reduce the axisymmetric vertical vessel reaction forces by about (30–40) % compared to unmitigated disruptions. On JET, the VDE, whether 'hot' or 'cold', always creates the conditions for a toroidal asymmetry in the plasma, so the VDE on the JET is referred to as Asymmetric VDE (AVDE). The interrupting of VDE and prevention of AVDE with SPI has been demonstrated. Thus, the effectiveness of disruption mitigation using SPI has been confirmed.

1. Introduction

Disruptions are an inherent property of tokamak plasmas, which cannot be completely eliminated [1, 2]. The consequences of disruptions are especially dangerous for large machines like JET and even more so for ITER. Disruptions can cause large Electro-Magnetic (EM) loads on the tokamak components and huge thermal loads

on the Plasma Facing Components (PFCs). Moreover, high-energy powerful Runaway Electron (RE) beams may arise during disruptions and cause serious damage to the machine.

On JET, Massive Gas Injection (MGI) has been routinely used in protection mode both to terminate pulses when the plasma is at risk of disruption, and to mitigate the potentially damaging impact of disruptions on the vessel and the PFCs [2–5]. Thus, disruption mitigation is meant to be applied on off-normal or post-disruptive plasmas.

The Disruption Mitigation System (DMS) design for ITER consists of Shattered Pellet Injectors (SPI) that can inject up to 27 pellets (24 from three equatorial ports and 3 from upper ports), which will be dedicated to the mitigation of EM and thermal loads, and the avoidance and suppression of runaway electrons [6–8]. The first demonstration of rapid plasma pulse shutdown using neon SPI for Thermal Quench (TQ) instigation was done on DIII-D [9]. DIII-D still provides valuable SPI studies, especially since it is well equipped with the appropriate diagnostics related to the SPI experiment, see, for example, one of the latest publications [10].

In 2019, the JET was equipped with an SPI through a collaborative effort of EURATOM, the ITER Organization, and the US Department of Energy aiming on strengthening the physics basis for disruption mitigation in ITER. The extensive capabilities of the SPI system allows studies on the efficacy of shattered pellets in reducing the EM and the thermal loads during disruptions and the avoidance/suppression of the formation of RE [11–18]. The fully commissioned system became operational in July 2019.

The SPI system on JET is intended to be used to study the physics of disruptions instigated by pellets and is not intended to be used to protect the machine. Therefore, to avoid interference of MGI with SPI, the MGI protection was disabled for the time window of the SPI experiments.

The Current Quench (CQ) time, τ_{80-20}, where τ_{80-20} is the time extrapolated from the time taken to quench from 80% to 20% of pre-disruptive plasma current I_p^{dis} (i.e. time interval between 80% and 20% of pre-disruptive plasma current I_p^{dis} multiplied by $\frac{5}{3}$) [19], is the key reliable measure of mitigation effectiveness. The axisymmetric vessel reaction forces, asymmetrical vessel displacement, plasma vertical displacement and bolometric energy are other essential measured parameters indicative of mitigation effectiveness.

In the presented experiments, the SPI was applied mainly on normal ('healthy') plasma i.e., plasmas not prone to disruption. However, the effect of SPI on post-disruptive plasma has also been tested, by using MGI to initiate disruptions. The suppression of Vertical Displacement Events (VDEs) and particularly, Asymmetrical Vertical Displacement Events (AVDEs) by SPI has also been studied and demonstrated on JET.

It should be noted that a full comparison of SPI and MGI disruption mitigation is beyond the scope of this paper. The research questions that we need to answer for the ITER DMS are related to SPI specific issues, especially assimilation, pre- and post-TQ. The dynamics of CQ is mainly determined by the impurity content (and possibly the distribution of impurities) in a CQ plasma, so a plasma with the same impurity content (regardless of the source, MGI or SPI) will give the same CQ dynamics. For both SPI and MGI, the assimilation is an open question, but the mechanisms for assimilation have clear differences. Comparing the assimilation of SPI and MGI is interesting and will allow to improve the models, but it is not the scope of this paper. Moreover, comparison of SPI and MGI disruption mitigation, particularly in terms of assimilated injected material, is not trivial, since the interaction of pellets and gas with plasma is quite different, for instance, pellet fragments can fly through the plasma without assimilation. In addition, JET MGI uses a gas mixture (90% D_2 + 10% Ar) to protect machines [2, 20], and only 14 pulses were performed with a gas mixture (D2 + Ne), while to mitigate disruptions in ITER, and therefore in the SPI experiments performed at JET, the composition of pellet (D_2 + Ne) was mainly used. However, where relevant, MGI data has been shown along with SPI data.

This paper is a full journal version of the data originally presented as posters at TMPDM_2020 [12] and EPS_2021 [13]. The remainder of this paper is structured as follows. A brief description of the JET SPI system and basic diagnostics of the SPI experiment are given in section 2. The composition of various aspects of the pellet ablation and assimilation is presented in section 3. The effect of pellet parameters on CQ duration are outlined in section 4. The efficacy of SPI on post-disruptive plasma is provided in section 5. The composition of various aspects of AVDE including SPI effectiveness on AVDE suppression is detailed in section 6. The axisymmetric forces data from a large database, along with SPI data, is given in section 7. The discussion of the presented data and outstanding issues, which are the subject of future investigations, are in section 8. The results of the given SPI experiments are summarised in section 9. A detailed description of the JET Shattered Pellet Injector system is given in the appendix A. Pellet speed data is provided in the appendix B. Some features of the use of Fast Visible Cameras, Interferometry/Polarimetry, Bolometry, Electron Cyclotron Emission (ECE) and High Resolution Thomson Scattering (HRTS) diagnostics in the SPI experiment are covered in the appendix C. 0D simulation of the interaction of the mixture (Ne + D) with plasma is given in appendix D.

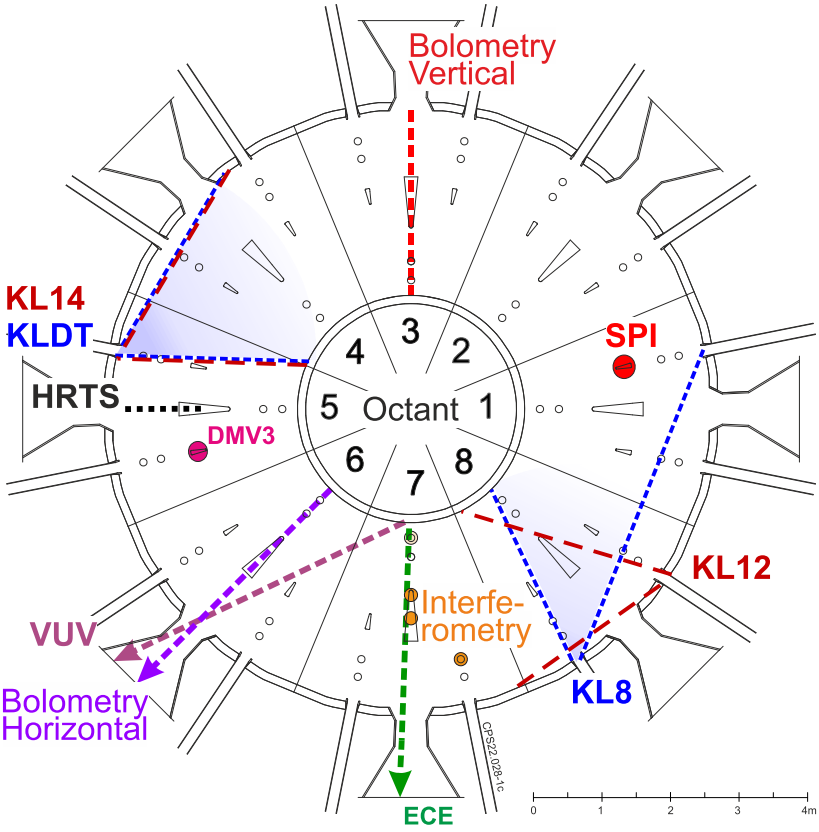

Figure 1. JET vessel plan view: SPI, Fast Visible (KL8 and KLDT) and Infrared (KL12 and KL14) camera views, Bolometry, Interferometry/polarimetry, ECE, VUV, HRTS and DMV3.

2. JET SPI system and diagnostics related to the SPI experiment

In 2019, the three injection barrels of SPI and a gas manifold system supplied by Oak Ridge National Laboratory (ORNL) were installed at JET together with the appropriate vacuum, cryogenic, mechanical and control hardware [14, 16, 21]. The JETILW SPI system is based on the design that was used on DIII-D [22].

The JET SPI is mounted in Octant 1 vertically on the top of the machine, figure 1. The pellet injector is arranged to propel the pellets vertically downwards along a flight tube. A flight tube guides the pellets along the circa 5 metres path to the vacuum vessel. Just before entering the vacuum vessel, the pellet hits the 'shattering element'. The purpose of the 'shattering element' is to fragment the pellet into small shards, increasing the surface area of the pellet material and distributing the pellet material over an increased angle. The spray of shards is directed towards the inner wall of the vessel within a 15-degree half angle cone [16], figure 2.

The SPI system has three different sized barrels in which the pellets are created. Pellet diameters, determined by the internal diameter of the barrels, are d = [4.57, 8.1, 12.5] mm and effective length/diameter ratio are [1.4, 1.6, 1.54] and are denoted here as [C, B, A] respectively. The injector can deliver D_2, H_2, Ne, Ne with D_2 shell, Ne+D_2 mixture, Ar and Ar + D_2 sandwich pellets, see appendix A for more details.

The main diagnostics related to the SPI experiment are the following, figures 1 and 3:

(1) The propellant valve solenoid current diagnostics record the time when SPI pellets were activated [16];

(2) Microwave cavity diagnostic that records the presence, the timing and the integrity of pellets [23];

(3) Two fast visible cameras, named KL8-E8WA and KLDT-E5WE provide 2D imaging of fast event dynamics in a large volume of JET plasmas [24–26] , figures 1 and 4. Both cameras have wide-angle tangential views of the JET plasma from just below the horizontal midplane. KL8 has a direct view of the SPI, so can provide information about the injection timing and material trajectory, while KLDT-E5WE views the part of the plasma toroidally anti-clockwise from the SPI. Typical frame rates of (10–20) kHz were used for SPI experiments, with exposure times (frame duration) in the range 1 μs–100 μs to obtain optimal signal levels. KL8 is equipped with remotely interchangeable narrow band filters to image spectral lines of Ne I atoms (692.9 nm), Ar I atoms (706.7 nm) or Ar II $^+$ ions (611.5 nm), while KLDT-E5WE always receives the light over the visible spectrum (430–730) nm. Infrared Camera's [27] views are shown on figure 1;

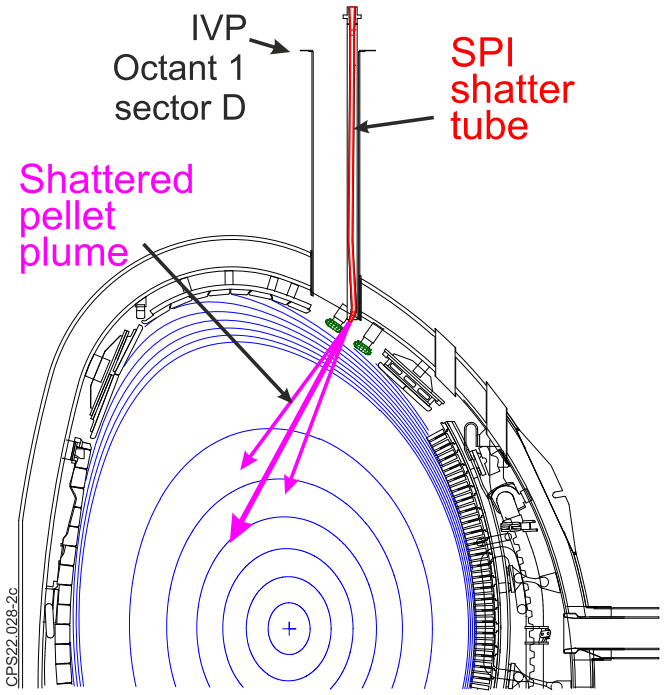

Figure 2. SPI shatter tube (in red) fitted in guiding tube in the Intermediate Vertical Port (IVP) in Octant 1 sector D.

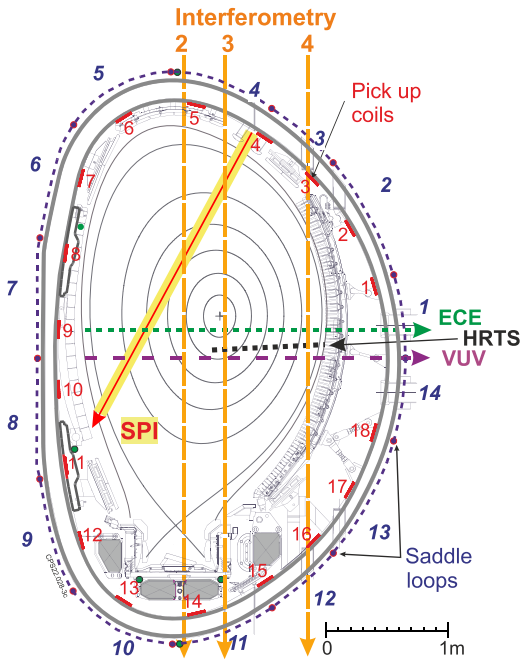

Figure 3. SPI, Interferometry/polarimetry, ECE, VUV, HRTS and Magnetic diagnostic coil and saddle projection on poloidal cross-section.

(4) Vacuum UV (VUV) diamond detector that records radiation with E $>$ 5.5 eV ($\lambda < 226$ nm). The VUV chamber is connected to the JET vacuum vessel by a long (~20 m) vacuum pipe, which enables a horizontal view of the plasma [28];

(5) Interferometry/polarimetry [29–31] with ~195 μm and ~119 μm beams;

(6) Vertical and Horizontal Bolometry Systems [32], figures 1 and 5. Bolometers measure any energy that hits the bolometric detector, namely radiation (photons) and neutral particles;

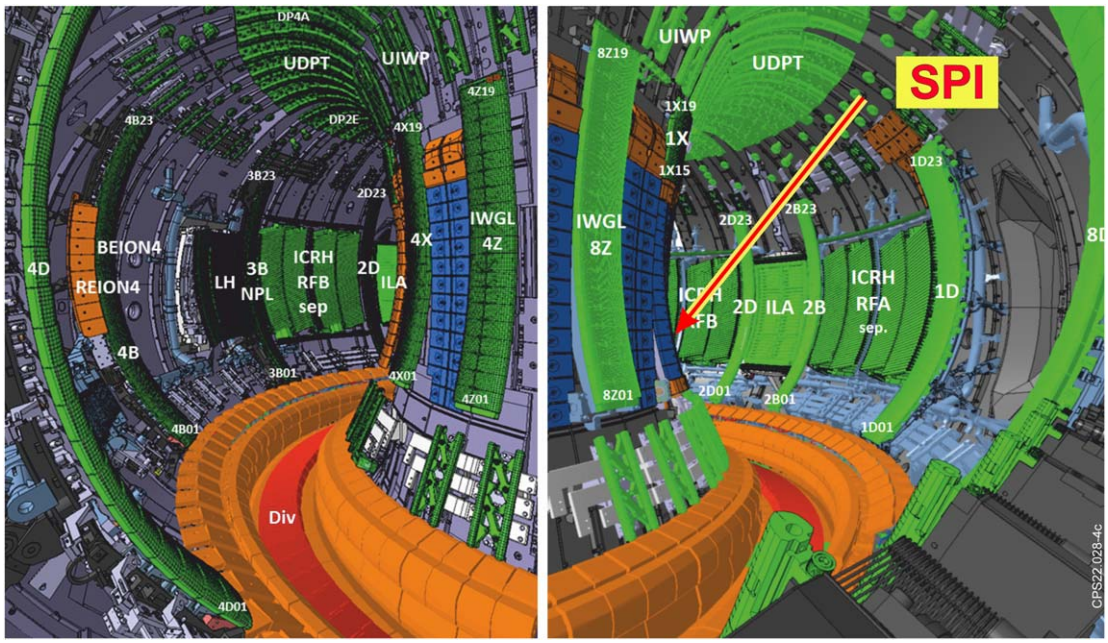

Figure 4. Lines of sight of the fast visible camera views: left is KLDT camera view from Oct.5 to Oct.4 and Oct.3; right is KL8 camera view from close to the midplane in Oct. 8 towards Oct 2.

(7) Electron Cyclotron Emission [33];

(8) High Resolution Thomson Scattering providing 63 spatial data points per profile, with a 20 Hz repetition rate for the duration of a JET pulse [34, 35];

(9) Magnetics [2, 4, 19], figure 3.

Some features of the Fast Visible Cameras, ECE, HRTS and Bolometry that are critical to interpreting SPI experiment data are covered in the appendix C.

3. Effect of pellets on plasma, pellet ablation and assimilation

This experiment was performed with ohmic plasma with $I_p = 1.1$–2.9 MA, average line density $n_e{\cdot}l \approx 2{\cdot}10^{19}$ m^{-2}, which corresponds to total number of plasma electrons $n_e{\cdot}V \approx 6{\cdot}10^{20}$ and mainly pellets with D_2 shell and Ne+D_2 composition. The data presented in this section is for the small pellet C, which is always fired directly by gas, and medium pellet B, fired by mechanical punch. Thus, the pellets C and B are different not only in amount of Ne, but also in speed of the pellet, see appendix B for more details. The typical time it takes for a pellet to travel from the SPI cold head to the plasma is ~20 ms for small pellet C (JPN 95149, JPN is the abbreviation of 'JET pulse number', 0.4 mm D-shell filled with 100% Ne, ~0.11 g; Ne = $3.07{\cdot}10^{21}$ atoms, D = $2.02{\cdot}10^{21}$ atoms: Ne/(Ne+D) = 0.60) fired by gas and ~60 ms for medium pellet B (JPN 95150, a mixture of (Ne+D) without D-shell, ~0.72 g; Ne = $2.04{\cdot}10^{22}$ atoms, D = $1.17{\cdot}10^{22}$ atoms: Ne/(Ne+D) = 0.64) fired by mechanical punch, figure 6.

The pellet release time is given by the peak in the breech pressure signal which is (1–2) ms later than the peak in the current valve. The JET SPI pressure signal is noisy so it may be difficult to do better than just saying that the pellet release time is at the end of the current valve pulse, figure 6.

The estimated speed of the pellet C (#95149) is ~(400–420) m/s, where the speed uncertainty is caused by uncertainty in the diagnostician's determination of the time when the Ne I light becomes 'visible'. The pellet fragments cause cooling of the plasma periphery, then TQ, which is the first part of the MHD phase, followed by CQ, figure 7.

The HRTS provides T_e and n_e profiles every 50 ms during a pulse but is not synchronised with the disruption event. However, by chance in pulse #95149 the T_e and n_e profiles were measured with HRTS during the early pre-TQ cooling phase at t = 24.0326 s, which was the last available HRTS time before disruption, figures 7(e) and 8. There is a good agreement between HRTS and ECE diagnostics in the early pre-TQ cooling phase just before SPI instigated the disruption, which suggests that ECE diagnostics does not suffer from cut-off at this stage. However, it should be noted that the lower T_e threshold for JET HRTS diagnostic until 2022 was about (50–100) eV, so HRTS data are not shown for plasma peripheries with R > 3.7 m.

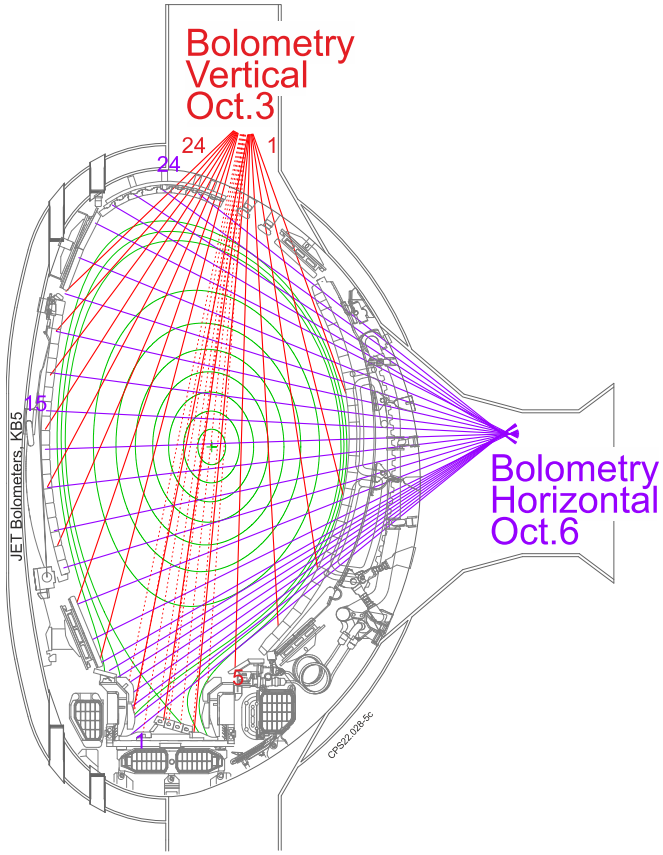

Figure 5. Vertical and Horizontal Bolometry systems, with channel numbering shown.

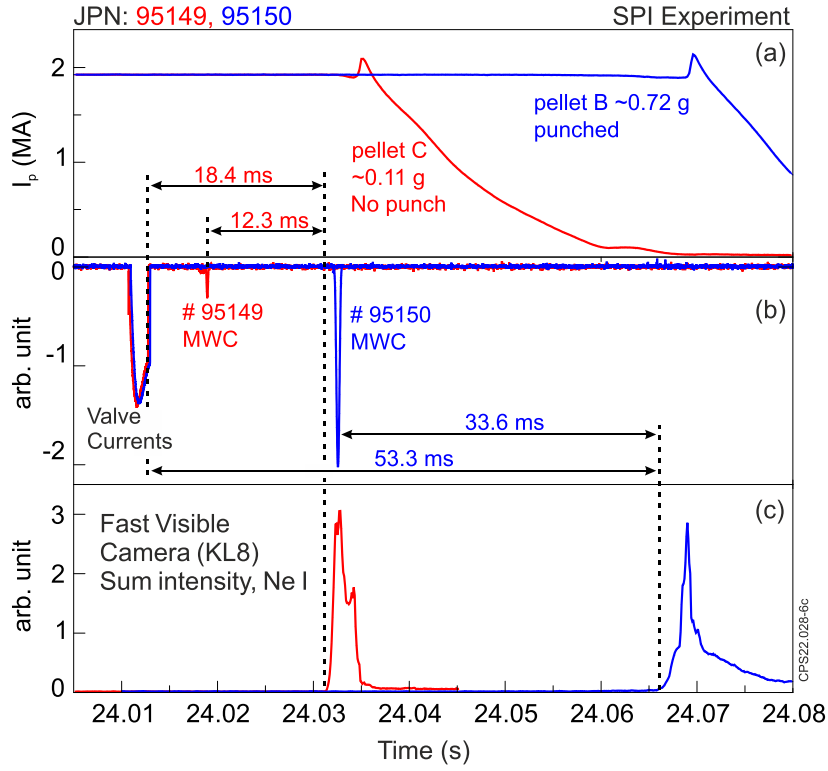

Figure 6. Pellet speed calculated from pellet flight time between MWC and plasma (the time the first shards are seen in the plasma by the high-speed KL8 camera equipped with a Ne I filter): (a) plasma current, (b) valve current and MWC signal, (c) Ne I sum intensity.

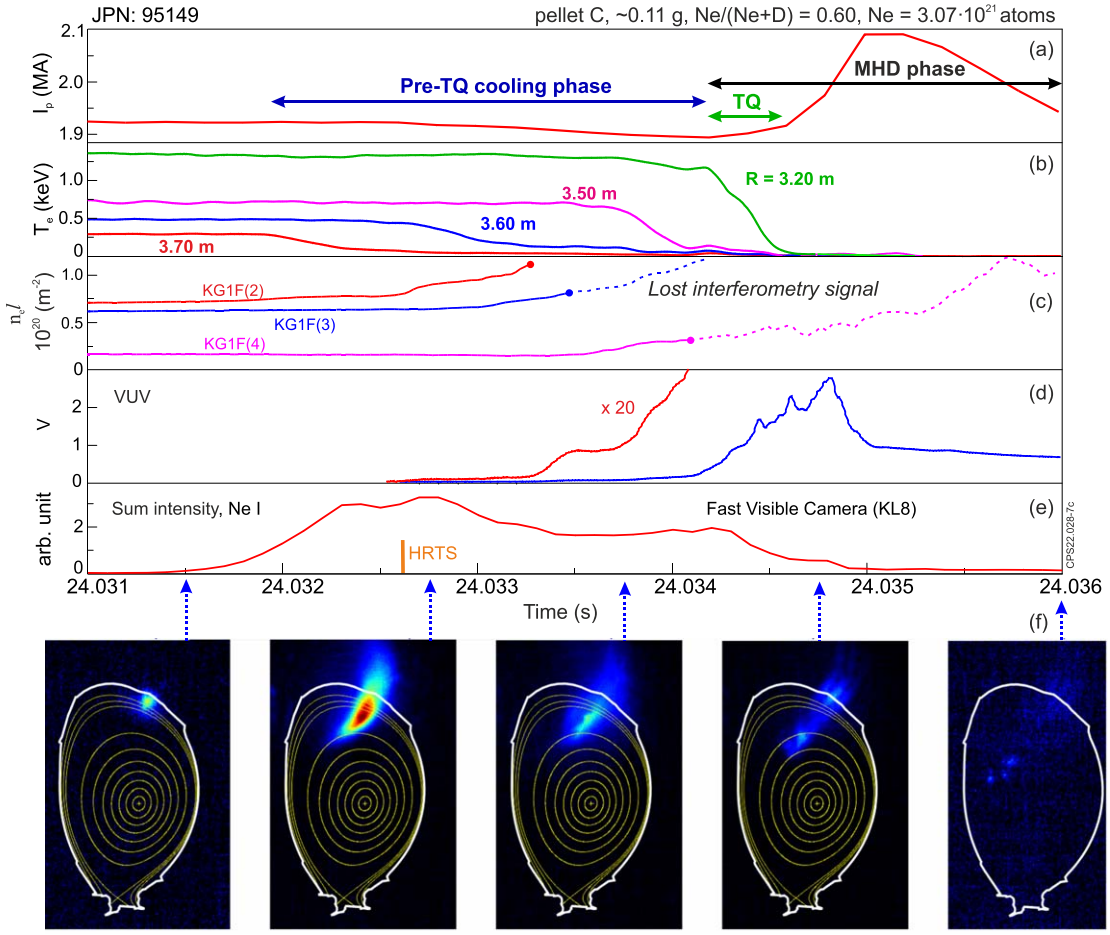

Figure 7. Small pellet C instigated disruption: (a) plasma current, (b) electron temperature, (c) line density, (d) VUV, the same signal with different amplification, (e) Ne I intensity, (f) Fast visible camera KL8-E8WA, 50 μs exposure time, Ne I filter, JUVIL parameter colour map = 5 k for all frames; the equilibrium shown for illustration purpose only.

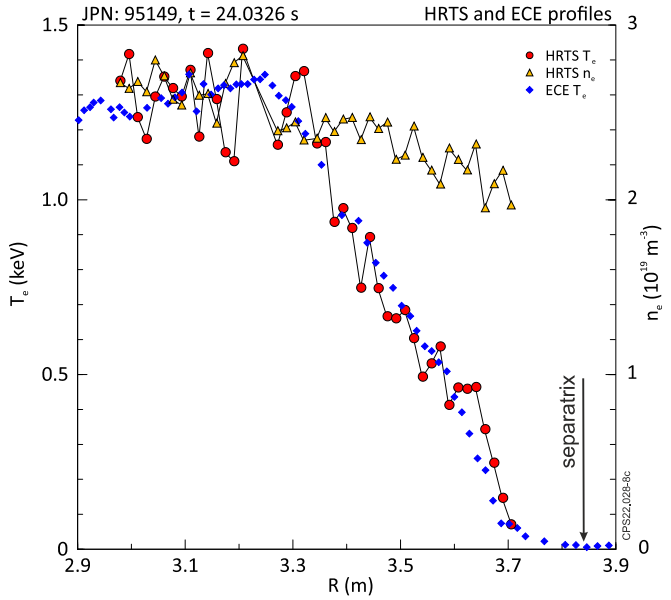

Figure 8. T_e and n_e profiles at the last available HRTS time before disruption. T_e shows good agreement between HRTS and ECE diagnostics. The lower T_e threshold for existing JET HRTS is about (50–100) eV.

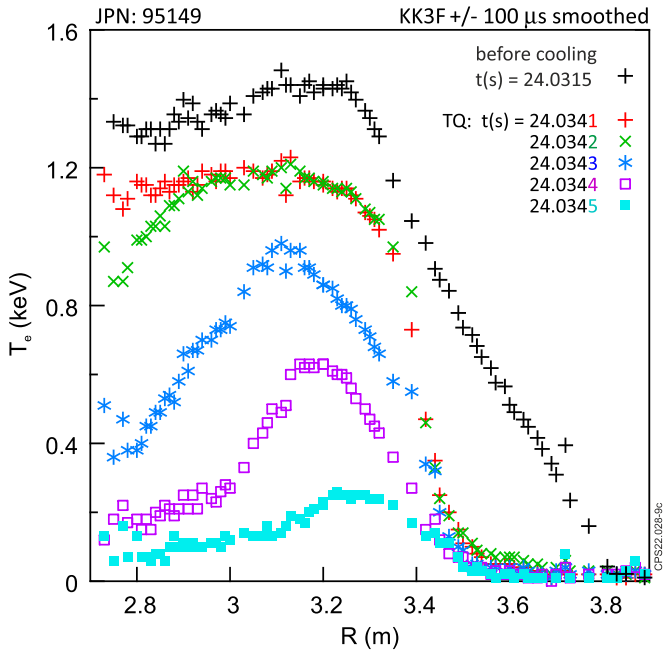

Figure 9. T_e profiles during TQ, ECE diagnostic (KK3F is JET jargon for fast ECE signals). Pre-TQ cooling phase duration is (2–2.5) ms, TQ duration is about 300 μs.

The small fast pellet C (#95149) results in a pre-TQ cooling phase duration of ~2.5 ms and TQ duration less than 0.5 ms. During the pre-TQ cooling phase, $t = (24.0315–24.0340)$ s, T_e degradation occurs at the outer region of the plasma, namely in the range $R \geqslant (3.4–3.8)$ m of the major plasma radius, which corresponds to $\rho \geqslant (0.5–0.6)$ of the normalised minor radius, where T_e drops below the diagnostic operating limit, figures 7(b) and 9. The duration of the pre-TQ cooling phase corresponds to the time required for the T_e cold front, in terms of the Ne I image, to reach the magnetic surface located at ~½ of the minor radius.

Then the T_e centre crashes during TQ, figure 9. The detailed explanation how the duration of TQ can be mathematically determined, is given in the 'Electron cyclotron emission' subsection of appendix C.

It is important to emphasize here that for a small pellet, the ECE diagnostic does not suffer from cut-off, since the ECE signal drop occurs first on the high toroidal field side and then on the low field side of the core.

The TQ phase is also characterised by bursts of MHD which continue beyond the TQ until the end of the distinctive plasma current spike, where we consider TQ and the current/voltage spike as two separate phenomena. At the MHD phase, noticeable plasma interactions with the outer limiters are observed, which is seen on the fast visible camera KLDT-E5WE without any filters, figure 10.

The remarkable observation in JPN 95149 is a very fast, only about 300 μs, collapse of electron temperature in the plasma core, figures 9 and 10.

For a similar pulse (#95150), the interaction of a medium size slow, ~(150–180) m/s, pellet B with the plasma is different, figure 11. The first pellet fragments (in the sense of Ne I image) are seen in the plasma by the high-speed KL8 camera, equipped with the Ne I filter approximately 9 ms before the I_p spike. These pellet fragments cool down the edge of the plasma but does not instigate TQ. Nevertheless, as for small fast pellet C, the duration of the pre-TQ cooling phase for pellet B corresponds to the time required for Ne I front image to reach the magnetic surface located at ~½ of the minor radius.

Then, about 2 ms before the I_p spike, the main cloud of pellet fragments, arrives causing rapid cooling and TQ. We believe that at this phase the ECE diagnostics suffers from cut-off because of the high density, see appendix C.

It is noteworthy that in pulse #95150, pellet fragments, according to the images of Ne I line, are clearly visible throughout CQ even at the end of CQ when the pellet fragments hit the inner wall of the JET, figure 12. Thus, it can be assumed that not all pellet fragments are ablated and far from all neon assimilated into the plasma.

Given a pellet speed for pulse #95150, the pellet can fly $\leqslant$ 10 mm during the exposure time of the frame (50 μs). Thus, each frame can be interpreted as a snapshot. Ne I images of medium pellet B at the beginning and at the middle of CQ are shown in figure 13. It can be seen that the cloud of neutral Ne lengthens with time which indicates a different speed of the pellet fragments. Presumably during shattering of the pellets, the fragments

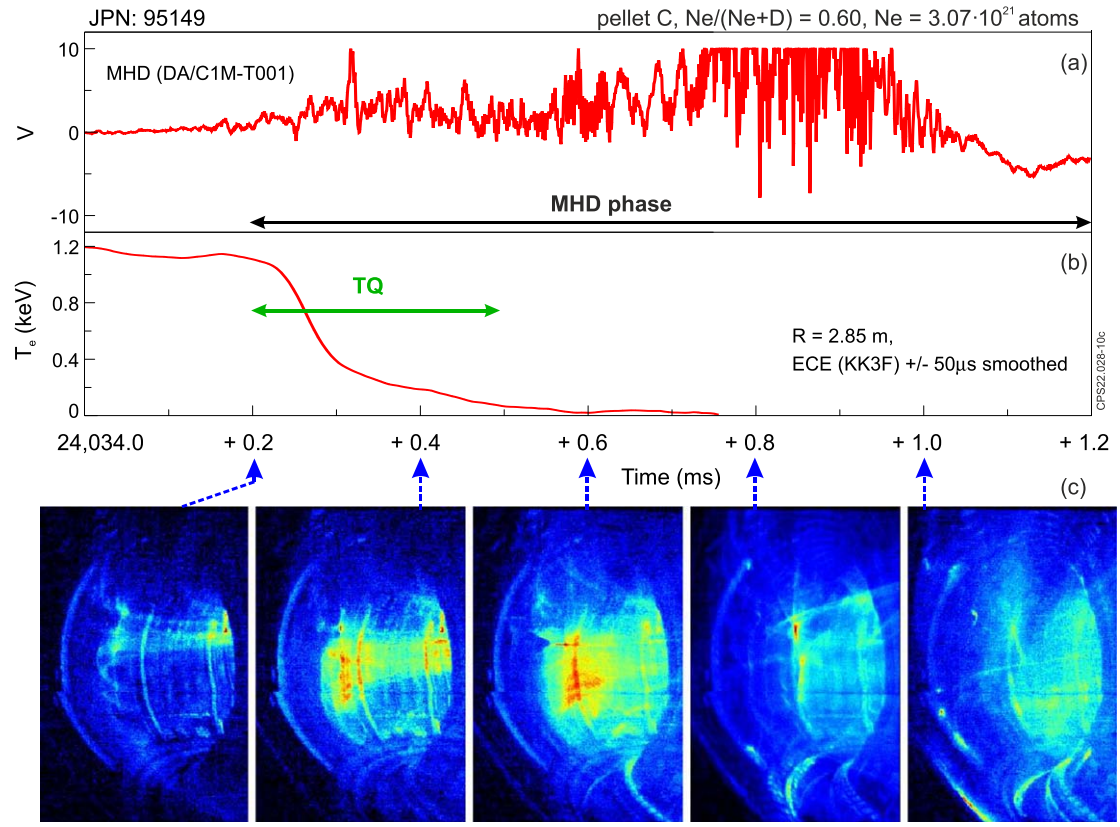

Figure 10. TQ, in which the plasma interacts with the limiter, and subsequent frames before CQ: (a) Mirnov, (b) electron temperature at R = 2.85 m, (c) Fast visible camera (KLDT-E5WE), 2 μs exposure time, no filter.

heterogeneously lost kinetic energy. The speed of the material, visible in the Ne I images was estimated using as detailed geometry mapping. The 'leading' fragments moved about 1.24 m and the 'tail' fragments moved about 0.46 m in 7 ms between two frames at 24.071 and 24.078s, see figure 13. So, the fragment cloud flies with non-uniform speed with a large spread in the range (66–177) m/s. Thus, gas formed during the shattering process affects the speed of fragments, accelerating some and slowing down other fragments [21].

The cloud of neutral Ne lengthens and widens as the cloud of fragments moves through the plasma. It could be assumed that the fragments that entered the plasma early are completely ablated and, therefore, the front of the cloud shown in figure 13 during CQ can be cut off. However, that must be ruled out because the speed of the front of Ne I image do not decrease when the pellet flies through the plasma.

The sum of all Ne I images during the interaction of the pellet with plasma, starting from cooling and further in the process of the CQ for small pellet C (#95149) and medium pellet B (#95150) are shown in figure 14. For small pellet C (#95149), neutral Ne atoms are only visible near the entry point of the pellet into the plasma during the entire process of interaction of pellet with plasma. Thus, this suggests that plasma fully assimilates neutral Ne of the small pellet C. In contrast to this for medium pellet B (#95150), neutral Ne atoms can be seen even near the inner wall of JET. Thus, this suggests that the Ne atoms are not fully assimilated and that the medium pellet B is too large for a 2 MA Ohmic plasma disruption instigation and discharge termination.

Polarimetric plasma density measurements for #95149, #95150 are shown in figure 15. The raw polymetric signal was scaled to match the interferometric signal before disruption and to the end of the CQ, and time was also adjusted to eliminate hardware delay, see appendix C for details. The density peak appears late in the CQ for both pellets, namely 7–8 ms after the TQ, which may have several possible explanations. Perhaps modelling is needed to explain this observation.

Let's try to evaluate the fraction of pellet electrons (*eFrac*) which are assimilated by the plasma. This can be done with several controversial assumptions, namely all pellet materials remain in the plasma at least until the plasma density reaches its maximum value, the shards radial distribution (as a of source of electrons) about the same for small and medium pellets, etc. The *eFrac* quantity is calculated as $eFrac(t) = (N_e(t) - N_{eo})/N_{epellet}$, where $N_e(t)$ is the total number of electrons in the plasma, N_{eo} is the total number of electrons in the plasma before the pellet arrive, and $N_{epellet}$ is the total number of electrons in the pellet. The $N_e(t)$ quantity is calculated as $N_e(t) = n_e l(t) \cdot V/l$, where $n_e l(t)$ is polarimetric measurement and l the measuring chord length in plasma is ≈2.2 m. Taking into account the upwards (~0.1 m) and inwards (~0.2 m) plasma displacements during the CQ, when

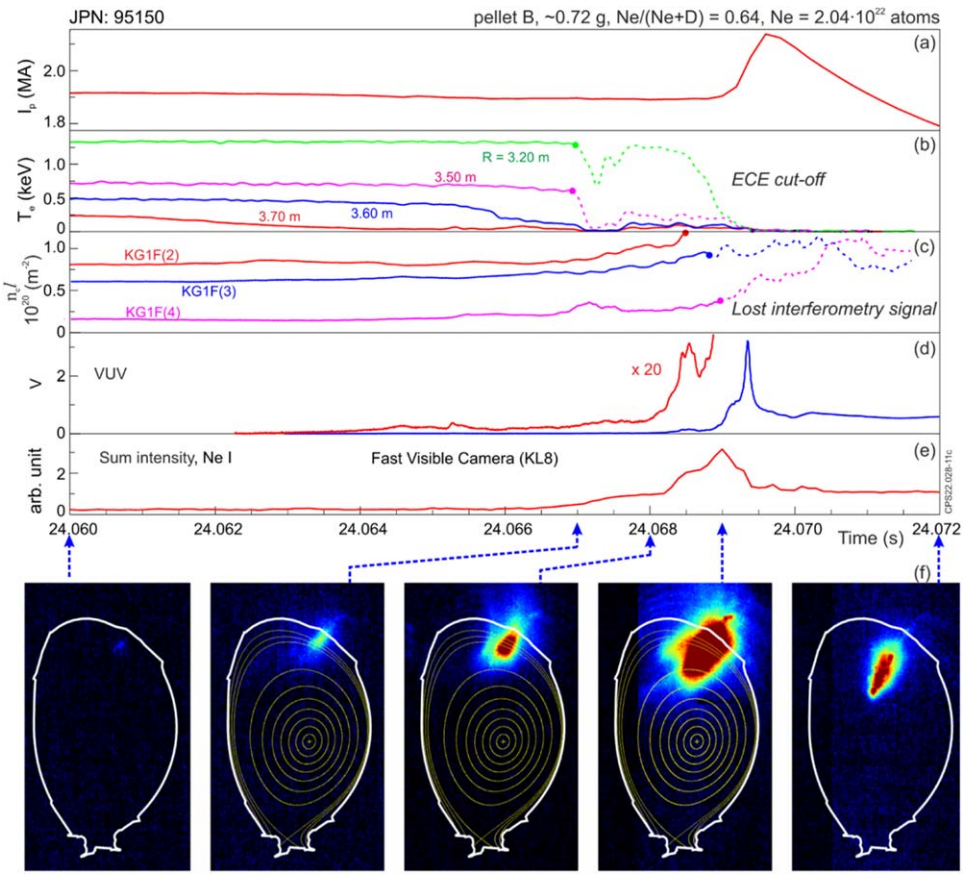

Figure 11. Medium pellet B instigated disruption: (a) plasma current, (b) electron temperature, (c) line density, (d) VUV, the same signal with different amplification, (e) Ne I intensity, (f) fast visible camera KL8-E8WA, 50 μs exposure time, Ne I filter, JUVIL parameter colour map = 5 k for all frames; the equilibrium reconstruction is for illustration purpose only.

polarimetry is at its maximum, the plasma volume V is ≈60 m^3. Table 1 shows an estimate of the fraction of pellet electrons assimilated by plasma at the time when the plasma density is maximum, provided there are no loss of pellet particles. Thus, the estimate of average electron loss of Ne atoms is about (30–35)% or 3–4 electrons out of 10 in the Ne atom at the time when the plasma density is maximum.

However, this estimate also assumed that polarimetry gave a toroidally 'averaged' electron density, which is likely the case given the toroidal arrangement of SPI and polarimetry, figure 1.

Despite the large difference in the parameters of pellets C and B, namely, the number of Ne and D atoms and the speed of the pellets, their efficiency, in terms of τ_{80-20}, measured radiated energy and vessel axisymmetric forces, during SPI instigated disruption is approximately the same, figure 15 (forces are not shown). It is worth mentioning that the bolometric (Processed Pulse File, PPF, name BOLO/TOPI, Oct.3) and VUV shown power assumes toroidal symmetry and therefore can be overestimated or underestimated [36]. However, a similar plasma (JPN: 87548) terminated by MGI fired in Octant 3 (where BOLO/TOPI is taken) shows the bolometric measured energy of only W_{TOPI} ≈3.8 MJ, which may indicate that BOLO/TOPI overestimates the measured energy in SPI experiments.

The tokamak plasma energy consists of the thermal and magnetic energy of the plasma current. During the entire disruption process, both thermal and some part of poloidal magnetic energy of the plasma are released to the wall either with plasma particles or radiation. Magnetic energy can penetrate through the vacuum vessel and affect the energy balance during the CQ, which in turn can affect T_e and, accordantly, CQ duration. In general, Poynting vector can be used to estimate the power flow of an electromagnetic field through the vacuum vessel, but this work has not yet been completed. In addition, estimating entire poloidal magnetic energy is challenging due to the presence on JET of the ferromagnetic iron core. However, the thermal and the internal poloidal magnetic energy just before disruption can be taken from equilibrium reconstruction. Thus, here we use the internal poloidal magnetic energy as an estimate of I_p magnetic energy before disruption, which is expected to be dissipated inside the vessel.

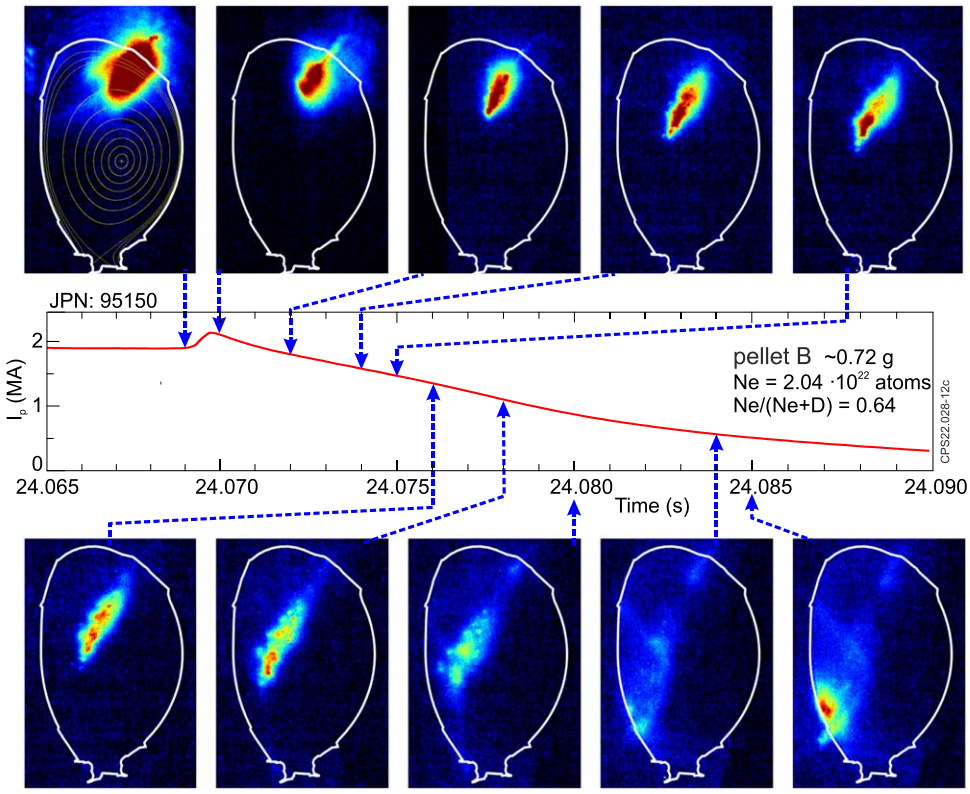

Figure 12. Medium pellet B instigated disruption but is not fully assimilated by the end of the CQ. Fast visible camera, 50 μs exposure time, Ne I filter, JUVIL parameter colour map = 5 k for all frames.

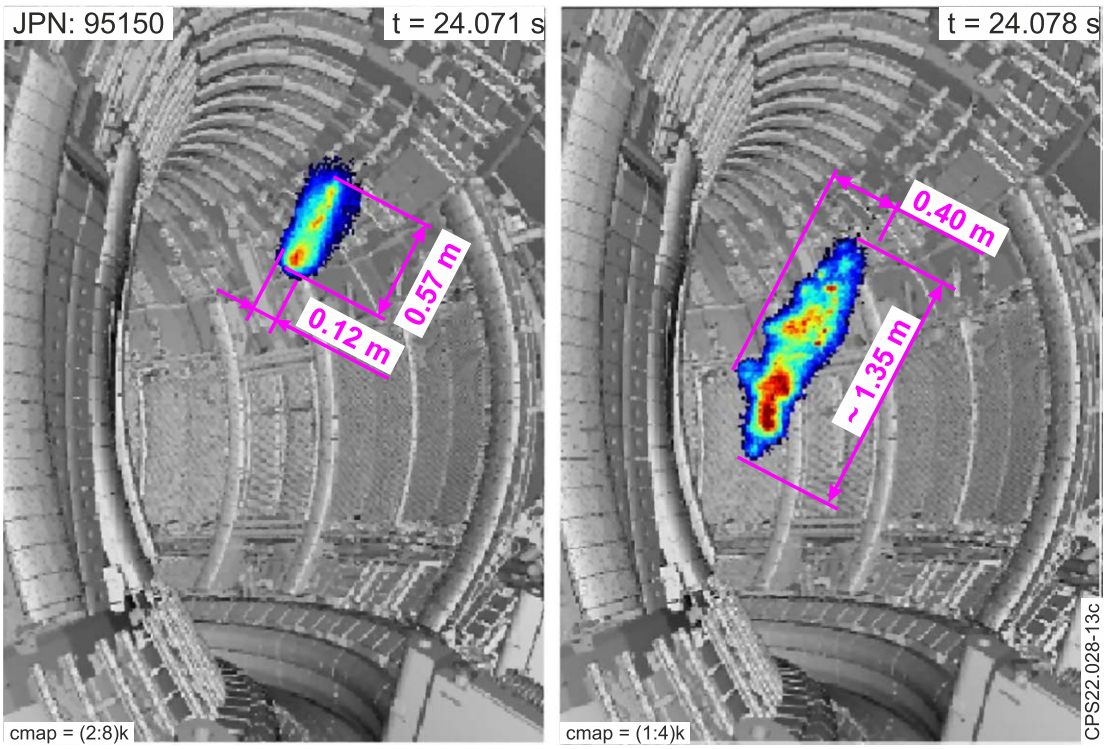

Figure 13. Ne I image of medium pellet B at the beginning and at the middle of CQ, 50 μs exposure time. The cloud of neutral Ne lengthens and widens with time.

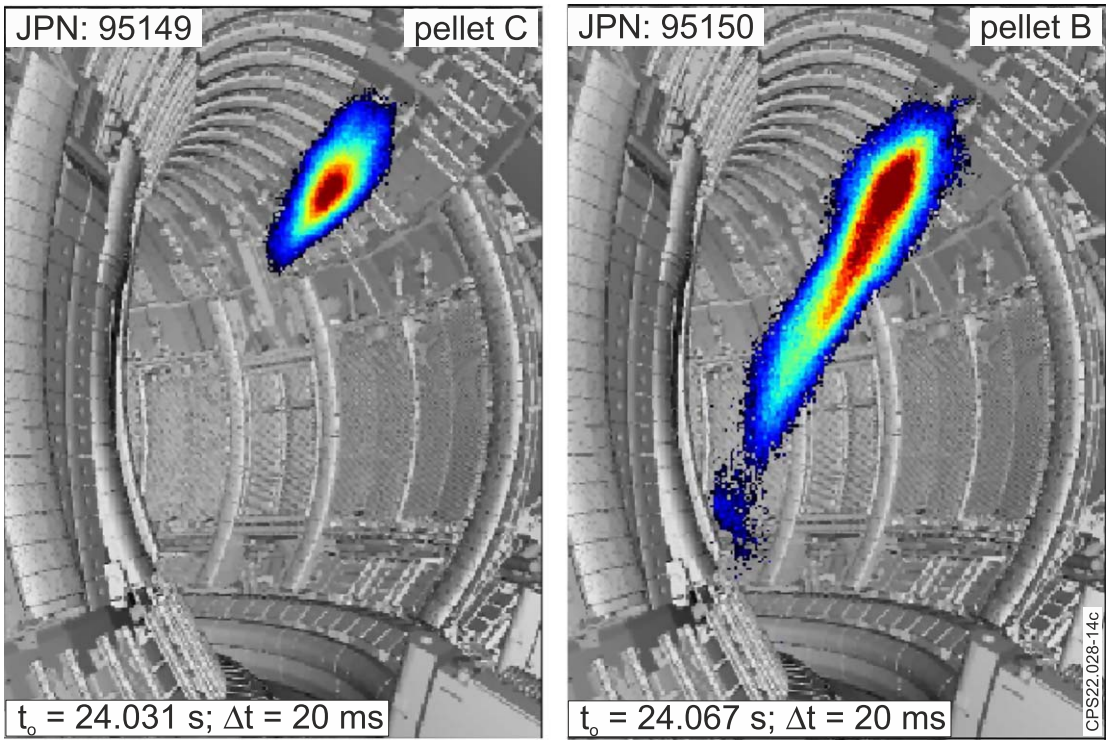

Figure 14. Sum of all Ne I images during the interaction of the pellet with plasma, starting from pre-TQ cooling phase and further in the process of the CQ for small pellet C (#95149) and medium pellet B (#95150).

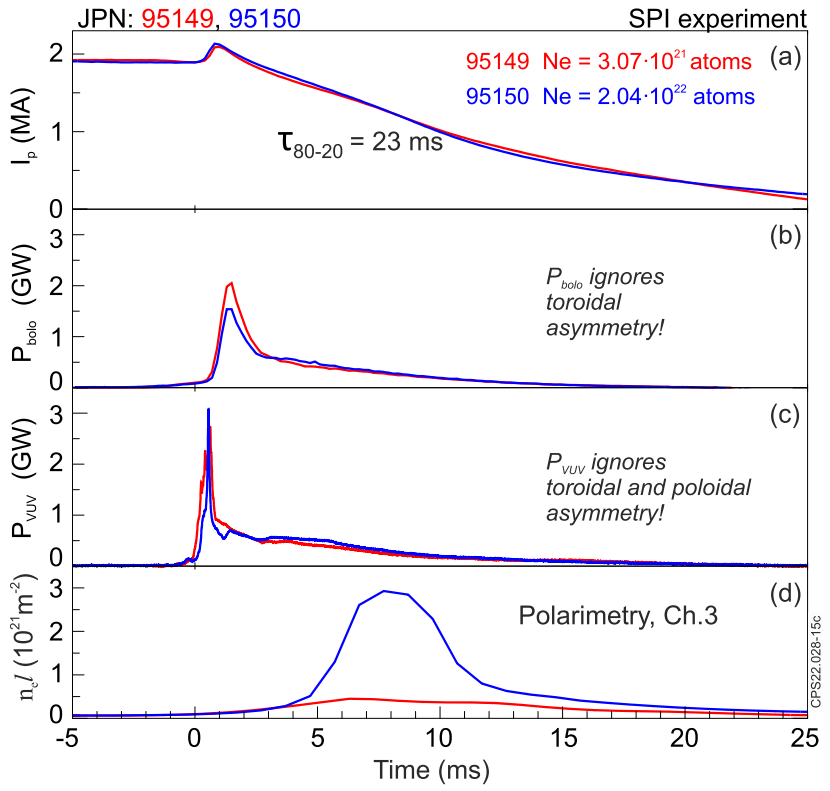

Figure 15. Comparison effectiveness of pellet C [Ne/(Ne+D) = 0.60, Ne = 3.07·10^{21} atoms] with small amount of Ne and pellet B [Ne/(Ne+D) = 0.64, Ne = 2.04·10^{22} atoms] with medium amount of Ne: (a) plasma current, (b) total bulk plasma bolometric power (BOLO/TOPI, Oct.3), (c) VUV energy is normalised to bolometry energy, (d) line averaged electron density. The time axis is zeroed to T_{dis} [2].

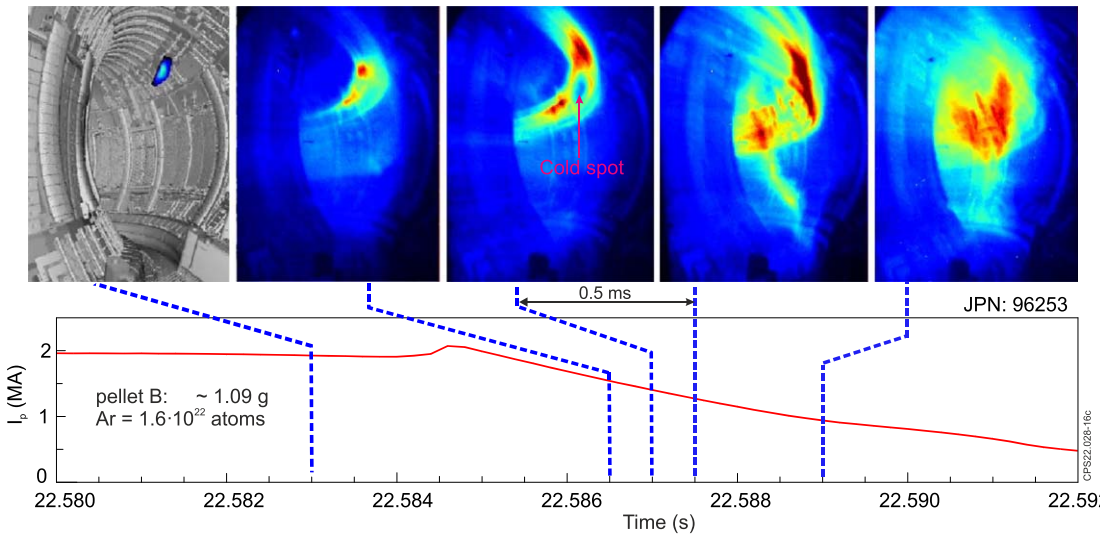

Figure 16. Medium Ar pellet B instigated disruption: Ar II images during pre-TQ cooling phase and CQ. A strong toroidal asymmetry of the Ar^+ ions, which exists during the first half of CQ.

Table 1. The estimate of average electron loss of Ne atoms at the time when the plasma density is maximum during the CQ.

	Pellet						
JPN	Ne atoms	D atoms	Electrons	max pol. (3) $n_e l$ (m^{-2})	max N_e	N_{eo}	max *eFrac*
#95149	$3.07{\cdot}10^{21}$	$2.02{\cdot}10^{21}$	$3.27{\cdot}10^{22}$	$4.5{\cdot}10^{20}$	$1.2{\cdot}10^{22}$	$1.7{\cdot}10^{21}$	31%
#95150	$2.04{\cdot}10^{22}$	$1.17{\cdot}10^{22}$	$2.16{\cdot}10^{23}$	$2.9{\cdot}10^{21}$	$7.7{\cdot}10^{22}$		35%

The thermal + internal poloidal magnetic pre-disruptive plasma energy W_{tot}^{dis} is expressed as $W_{tot}^{dis} = W_p^{dis} + W_{imag}^{dis}$, where W_p^{dis} is plasma thermal energy and $W_{imag}^{dis} = \frac{1}{2\mu_o}\int \vec{B}_p^2 dV$ is internal plasma current magnetic poloidal energy. The W_{imag}^{dis} quantity can be expressed in terms of the output EFIT parameters [37], as $W_{imag}^{dis} = 0.25\ \mu_o{\cdot}li{\cdot}R_o{\cdot}I_p^2$. For #95149 and #95150 the internal pre-disruptive plasma energies are approximately the same, namely, $W_{tot}^{dis} \approx 4$ MJ with $W_p^{dis} \approx 0.4$ MJ and $W_{imag}^{dis} \approx 3.6$ MJ.

Thus, Ohmic plasma, with $I_p \approx 2$ MA and $W_{tot}^{dis} \approx 4$ MJ, can be successfully terminated, providing relatively short CQ duration, by a small pellet C with the amount of neon $\sim 3.07{\cdot}10^{21}$ atoms. Presumably a high plasma current and a high thermal energy plasma requires more Ne atoms in the pellet to obtain efficient plasma termination. The next section 6 contains relevant data for this.

The diagnostic advantage of the Ar pellet is that fast visible camera KL8 can be equipped with an Ar II filter that allows the Ar^+ image to be seen, figure 16. One can see a strong toroidal asymmetry of the Ar^+ ions, which exists during the first half of the CQ. This first half of the CQ is characterised by a highly visible helical structure, as shown in figures 16 and 17.

However, as the plasma current drops from 2 MA below 1 MA and q on the plasma boundary increases from ~5 to approximately above ~10, the helical structure is no longer clearly visible and, in addition, the entire plasma is filled with Ar II light. Thus, at least during the first half of the CQ, the injected impurities are toroidally asymmetrical with the source located in the toroidal plane where pellets are injected. Fine structures are clearly visible, for example a cold spot, where the main pellet fragments should have been located, figures 16 and 17.

The additional electrons created by injected pellet tend to be uniformly distributed toroidally under the pressure gradient. However, the heavy ions slow down the toroidal motion of electrons. Presumably, the plasma moves along the magnetic field at the ion sound.

In the JPN 96253, the 'Ar+ plasma' front moves at a speed of 5 m ms^{-1} in the time interval between two frames 22.5865 s and 22.5870 s (time interval 0.5 ms). Consider a plasma consisting of one type of ions, then the ion sound speed be expressed as $v_s \approx \sqrt{\frac{ZT_e}{m_i}}$, where m_i is an ion mass and Z is ion charge. Then T_e can be

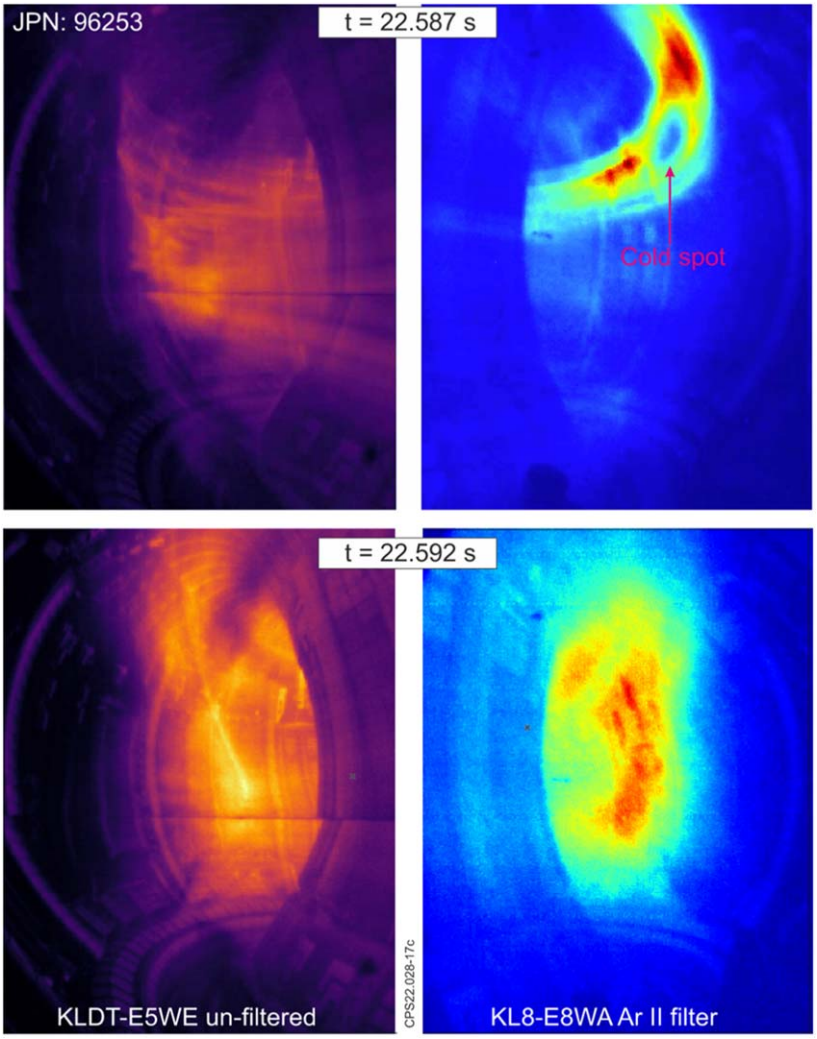

Figure 17. Helical structure is clearly visible in the upper images, it can be seen 'cold spot' on the upper right image. The lower images do not show a helical structure, the entire vessel filled with Ar II. Left KLDT-E5WE, 2 μs exposure time, un-filtered; right KL8-E8WA, 50 μs exposure time, Ar II filter.

estimated from the speed of sound: $T_e \approx 10/Z$ eV. The charge of the Z ion is unknown but can be expected to be in the range Z = 2–5. Thus, T_e during mitigated CQ should be in the range 2–5 eV.

The bolometric measured power shows a spike after TQ with a smooth fall during CQ, figure 15(b). It should be noted that the bolometry (PPF name BOLO/TOPI, Oct. 3) hardware time resolution ~2 ms, see appendix C for more details. The bolometric measured energy at CQ is about (70–80)% of the total measured energy for the entire process of pellet-plasma interaction. A similar estimation of the radiation energy losses with VUV (one channel in the middle plane, Oct.7) gives the fraction of measured energy losses during the CQ in the range of (80–90)%. Thus, the main radiation losses occur during CQ. However, this estimate should be treated with great caution, taking into account that Ar II light (figures 16 and 17 right) and, presumably the radiated energy, at least during the first half of the CQ, are strongly toroidally asymmetric.

4. Effect of pellet parameters on CQ duration

4.1. Using MGI on JET

On the JET-ILW, the MGI is used to protect the machine, namely (a) to terminate pulses when the plasma is at risk of disruption and (b) to mitigate the consequences of disruption [3, 20].

Using MGI for these purposes is mandatory in JET if $I_p \geqslant 2.0$ MA or thermal + internal poloidal magnetic plasma energy $\geqslant 5.0$ MJ [38, 39]. Additionally, for VDEs, the MGI must be used for $I_p \geqslant 1.25$ MA. Moreover, when plasma Vertical position Stabilisation system (VS) signals are polluted by $n = 2$ modes the VS may become inoperable, so the MGI can be triggered by a certain amplitude of $n = 2$ mode or by the signals which detected a technical fault of the VS system.

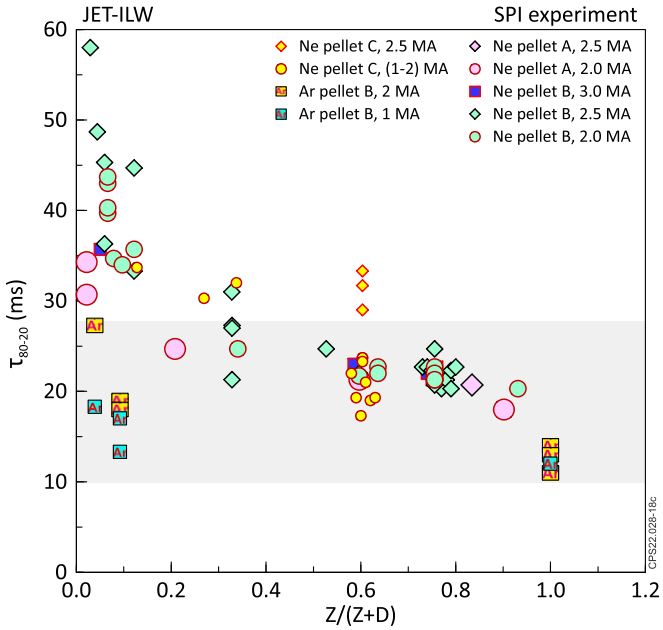

Figure 18. Dependence of CQ duration on Ne or Ar fraction, where Z is Ne or Ar number of atoms. The desirable JET τ_{80-20} is shown by shaded grey area. All are X-point plasmas except 'Ar pellet B, 1 MA', which are a limiter circular plasma.

To terminate the pulses when the plasma is at risk of disruption, the MGI is triggered by an amplitude of $n = 1$ locked mode or an amplitude of $n = 1$ locked mode normalised by I_p that exceeds a threshold [2, 40]. To mitigate the damaging effects of disruption, either dI_p/dt or the toroidal loop voltage or the rate of plasma vertical displacement exceeding threshold values is used as a trigger.

In protection mode, MGI works with an optimum gas mixture of 10% Ar with 90% carrier gas which should be either D_2 or H_2 depending on the dominant plasma components. The CQ time duration, τ_{80-20}, is the key characteristic of mitigation effectiveness. The τ_{80-20} for JET must be in the region of (10–27.5) ms, with the lower threshold given by eddy current force loads [41]. The upper threshold is justified by minimisation of (a) thermal loads on PFCs due to cold VDEs, when plasma position is not controlled vertically during CQ and (b) axisymmetric (and sideways) vessel forces. Thus, on the JET-ILW, the purpose of the PFC protection is to prevent melting of Be at the top and W at the bottom-outer part of the machine.

The recommended amount of gas to be injected depends on the maximum plasma current during an entire pulse $\propto I_p^{\alpha}$, where $\alpha = (2.6–2.8)$ depends on the specific design of the Disruption Mitigation Valve (DMV) [20]. For example, the lower limit of the required amount of gas for DMV3, which satisfies the upper recommended threshold of $\tau_{80-20} \leqslant 27.5$ ms, are 0.7 *bar•l* for 2 MA and 2.2 *bar•l* for 3 MA maximum I_p in the pulse. For further comparison with a pellet, the amount of injected gas is better expressed in atoms: ($1.8 \bullet 10^{21}$ Ar + $3.2 \bullet 10^{22}$ D) and ($5.4 \bullet 10^{21}$ Ar + $9.7 \bullet 10^{22}$ D) for 2 MA and 3 MA maximum I_p in the pulse, respectively.

4.2. Dependence of the CQ duration on pellet content

The effect of SPI pellets on the duration of the plasma current quench has been studied and the data are presented below. The presented data refer to plasmas with $I_p = (1.1–3.1)$ MA, thermal + internal poloidal magnetic pre-disruptive plasma energy $W_{tot}^{dis} = (1.5–14.3)$ MJ, and (Ne + D) pellet with Ne fraction, Ne/(Ne + D), in the range (0.02–0.93), Ar pellet fraction in the range (0.04–1.0).

The dependence of τ_{80-20} on Ne (or Ar) fraction for different pre-disruptive plasma currents is shown in figure 18, where the grey shaded area indicates the desired region for JET. The figure 18 data show strong dependence of τ_{80-20} on Ne (or Ar) fraction, which can also be masked by dependence of CQ duration on number of Ne (or Ar) atoms in a pellet. Moreover, there is a noticeable scatter in the τ_{80-20} data for pellets C, Ne/(Ne+D) ≈0.6 which is discussed in the following paragraphs.

The dependence of τ_{80-20} on the number of Ne or Ar atoms in the pellet is shown in the figure 19. From figure 19 it can be seen that a pellet with a high content of Ne ($\geqslant 2 \cdot 10^{22}$ atoms) can reduce the CQ duration for plasma with $W_{tot}^{dis} \leqslant 15$ MJ to below the upper required JET threshold, namely $\tau_{80-20} \leqslant 27.5$ ms. Also, it was expected, and this is confirmed by figures 18 and 19, that Ar pellets are more efficient than Ne pellets, which follows from the cooling rates for Ar and Ne impurities calculated in 'coronal approximation', see figure 2 in [42] or Fig. 2.14 in [43].

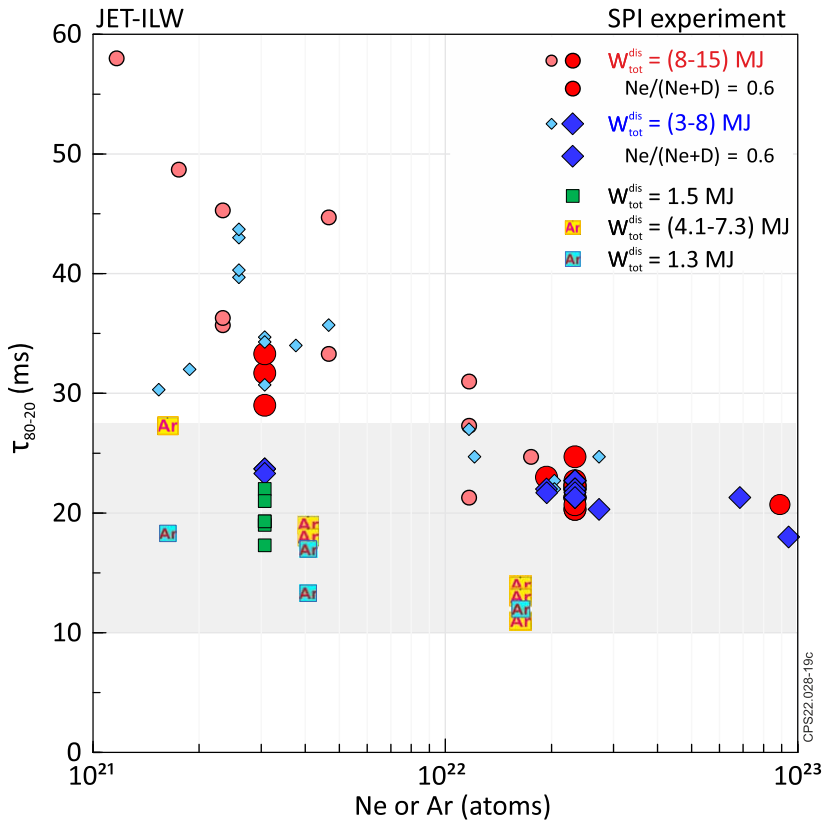

Figure 19. Dependence of the CQ duration on number of Ne or Ar atoms in a pellet, W^{dis}_{imag} is the pre-disruptive internal plasma energy. Small and large circles (and diamond) indicate W^{dis}_{tot} in the (8–15) MJ (and (3–8) MJ) ranges. Large circles and diamonds indicate the large Ne fraction, $\geqslant 0.6$. The desirable JET τ_{80-20} is shown by shaded grey area.

Moreover, for a small amount of Ne $\approx 3{\cdot}10^{21}$ atoms, but still a large Ne fraction ($\geqslant 0.6$), the dependence of τ_{80-20} on W^{dis}_{tot} is visible, figure 19. To better see this relationship, in figure 20 shows this data subset as τ_{80-20} versus W^{dis}_{tot}. The well-marked dependence of τ_{80-20} on W^{dis}_{tot} for the small pellet C presumably reflects the fact that the pellet C is completely assimilated, see also figures 7 and 14 left frame. However, if pellet is large enough, then pellet fragments will fly through the plasma without assimilation (see figures 12 and 14 right frame), since there is no dependence of τ_{80-20} on W^{dis}_{tot} for the medium and large pellets B and A. Thus, a high W^{dis}_{tot} plasma requires a high Ne content (and Ne fraction) in the pellet to obtain a short CQ duration.

It seems that if the injected impurities reduce T_e during CQ to a small value, presumably below (5–10) eV, then an additional increase in the amount of impurities will not lead to a further decrease of the τ_{80-20}, as also shown on figure 15.

The figures 18–20 show that τ_{80-20} never dropped below 10 ms. It is worth mentioning that figures 18 and 19 are similar to published figures 8 and 9 of [Gerasimov EPS 2021] - [13] and figures 8 and 2 of [Jachmich Nucl. Fusion 2022] - [15], but using an extended database. Moreover, our newest interpretation of the observed dependence in figures 18 and 19 differs in some points from that of [15].

Presumably, the thermal energy is mainly released during the TQ or entire MHD phase, while plasma magnetic energy is mainly released during the CQ. Despite this declaration, in figures 19 and 20 uses W^{dis}_{tot}, not W^{dis}_{imag}. However, the dependence of the τ_{80-20} on W^{dis}_{imag} showed a very similar trend as the dependence on W^{dis}_{tot}.

Consider a data cluster where the sum of the thermal and internal magnetic energies, W^{dis}_{tot}, are in the range (3.9–4.1) MJ. Having a plasma with approximately the same W^{dis}_{tot}, the bolometric measured power (PPF name BOLO/TOPI) during the entire CQ is about the same, (5–7) MJ, for large variations in the amount of Ne (red points in figure 21). However, with a small amount of Ne $= 0.8{\cdot}10^{21}$ (and, accordingly, a small Ne fraction and a large amount of D) in the pellet (#95106), the bolometric measured energy can be half as much compared to the cases when number of Ne atoms in pellet $\geqslant 1.5{\cdot}10^{21}$, figure 21.

Figure 22 explains the exceptionally low bolometric measured energy, $W_{TOPI} = 3.3$ MJ, (compared to $W_{TOPI} = 6.0$ MJ in the #95113) in #95106, where a small amount of Ne was used in the pellet. In pulse #95106, the pellet instigates disruption with slow I_p decay and a cold VDE occurs during CQ phase. Most likely, the CQ duration is affected to a greater extent by the plasma motion during cold VDE than by T_e drop. Pulse #94579 in the figure 22 is another example of the use of pellets with a small amount of Ne, where SPI instigated a disruption

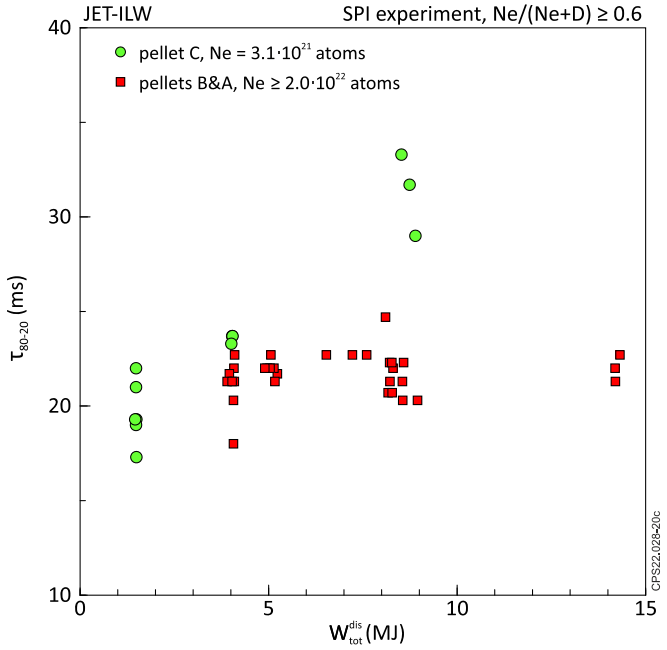

Figure 20. Dependence of the CQ duration on W_{imag}^{dis} on pre-disruptive internal plasma energy for various amounts of Ne in the pellet and Ne/(Ne+D) $\geqslant$ 0.60.

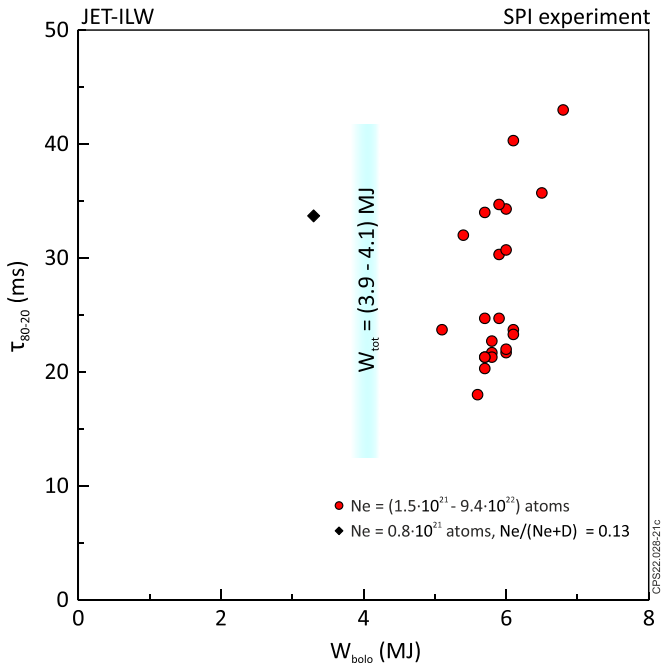

Figure 21. Relationship of the CQ duration on bolometric measured energy, W_{TOPI}, for pulses with W_{tot}^{dis} ≈4.0 MJ and various amounts of Ne atoms.

followed by a cold VDE. Moreover, second full scale (in term of the I_p spike) disruption occurred during cold VDE; this second disruption terminates the cold VDE in terms of the plasma current centroid motion.

Thus, the pellet with small amount of Ne and accordingly large amount of D, instead of causing a mitigated CQ, may cause a 'cold' VDE, which is the worst-case scenario for disruption mitigation. On the other hand, the well mitigated disruptions with the high content of Ne may have 3-fold difference in the CQ duration with approximately the same deposited energy (figure 21). Accordingly, the power deposited to the PFCs may differ by the same factor 3 and can affect the lifetime of the plasma facing components.

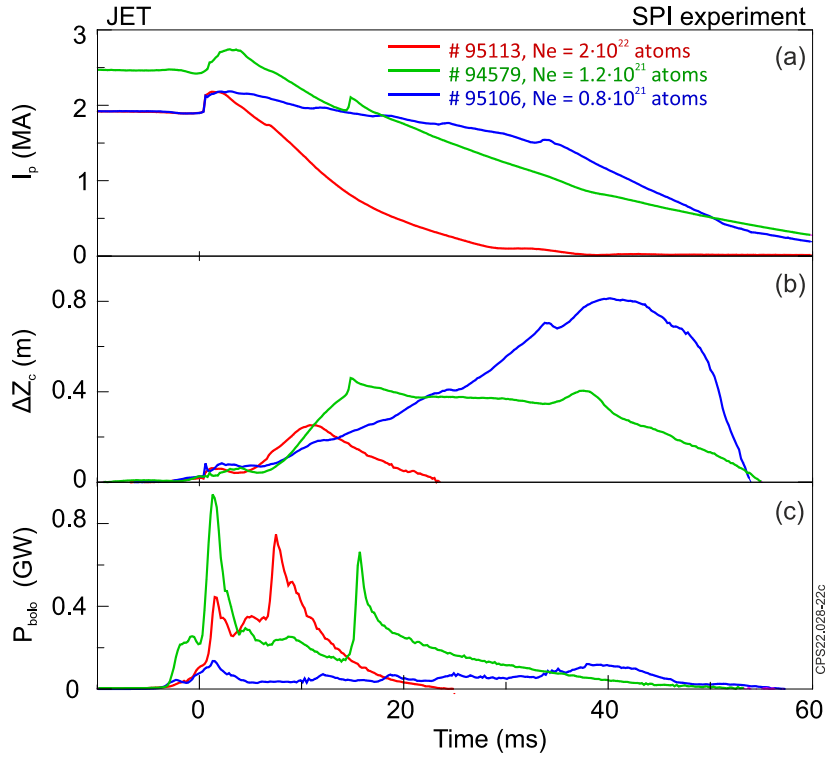

Figure 22. SPI instigate mitigated disruption (#95113 and #94579), but a small amount of Ne results in a 'cold' VDE (#95106): (a) plasma current, (b) plasma current vertical displacements, (c) total bulk plasma bolometric power (BOLO/TOPI). The time axis is zeroed to T_{dis}.

Table 2. The estimate of the plasma temperature in CQ.

τ_{80-20} (ms)	12	18	23	29	41	59
T_{eCQ} (eV)	2	3	4	5	7	10

4.3. T_e estimate during CQ

Let us estimate the plasma electron temperature (T_e), assuming that a decay time, $\tau_{L/Rsp}$, of the plasma current depends on the ratio of the inductance and resistance of the plasma considering that resistance and inductance do not change during CQ. Here *Rsp* is Spitzer resistance, and $L = \mu_o R_o \left[\ln\left(\frac{8R_o}{a}\right) - 2 + \frac{l_i}{2}\right]$ is inductance of the plasma torus. It is worth noting that total plasma inductance depends on the plasma elongation and is affected by JET ferromagnetic iron core and plasma - PF coils mutual inductances. Here we use a simple expression for the total plasma inductance.

The parallel Spitzer resistivity is expressed as $\eta_{\|} = 5.15{\cdot}10^{-5}\frac{Z_{eff}\ln\lambda}{T_e^{3/2}}$ (Ω·m), where $ln\lambda$ is the Coulomb logarithm. The relationship between CQ linear extrapolation, τ_{80-20}, and exponential decay, $\tau_{L/R}$, is $\tau_{80-20} = \frac{5}{3}(\ln 0.8 - \ln 0.2)\tau_{L/R} \approx 2.3\,\tau_{L/R}$. Here we take Z_{eff} from the simple 0D model as $\langle Z_{eff}\rangle = 0.78\ T_{eCQs}^{0.5}$, see appendix D. An estimate of T_{eCQ}, the plasma temperature in CQ, for $ln\lambda = 10$ is given in table 2.

The calculated value of T_{eCQ} is quite reasonable if we take into account the dependence of the cooling rates on the electron temperature. Thus, the estimated temperature during CQ for the pulses shown in figure 15 is $T_e \approx$(3–5) eV. In 2022, the JET HRTS has been upgraded to allow low T_e (down to 1 eV) measurements during CQ and validate the methods used. It can be noted here, that the upgraded HRTS diagnostic, generally confirmed our assessments.

5. Effectiveness of SPI on post-disruptive plasma

In the presented experiments, the SPI was applied mainly on normal ('healthy') plasma i.e., not prone to disruption. However, the disruption mitigation is meant to be applied on off-normal (including VDE) or post-disruptive plasmas. The data presented here refers to the Shattered Pellet Injector (SPI) experiments conducted

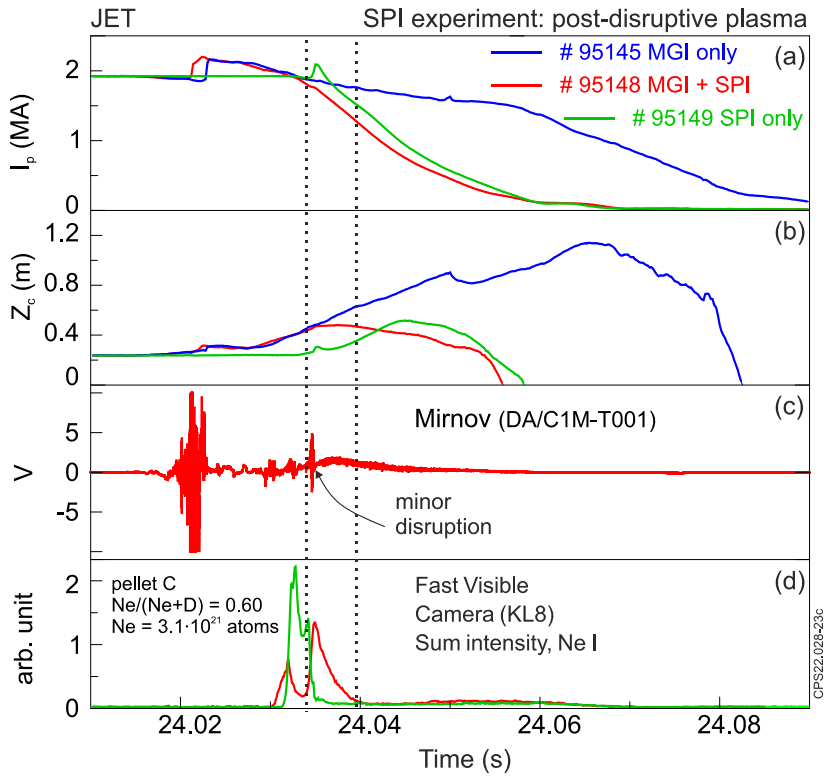

Figure 23. Effectiveness of SPI on post-disruptive plasma: (a) plasma current, (b) plasma current vertical position, (d) Mirnov signal, (c) Ne I intensity summed over the frame. For #95148, Ne I images for the time indicated by the dotted line are shown in figure 24.

at JET in 2019–2020, where only a few pulses were dedicated to the experiment with post-disruptive plasma and there was only one successful pulse #95148, which was mentioned in [12–15]. Considering that nothing like this was done in JET until 2022, here we present a fresh look at this unique experiment.

In this experiment the disruption was initiated by injection of D_2 using the DMV3 (see figure 1). The DMV3 was filled with a small amount of D_2, namely ~0.1 *bar•l*, which corresponds to ~$4\bullet10^{21}$ deuterium atoms. The injected gas led to an increase in density from ~$6\bullet10^{19}$ m^{-2} to ~$10\bullet10^{19}$ m^{-2} (channel 3 on figure 3) which led to a major disruption, see #95145 on figure 23. The amount of D_2 injected was chosen as a minimum amount of injected D_2 that resulted in a major disruption. A small, ~20%, decrease in injected D_2 caused only minor disruption without CQ.

The #95145 pulse was used as a reference pulse for SPI mitigation. The small pellet C, which will no longer be available on JET after 2020, with Ne = $3.1\bullet10^{21}$ atoms, Ne/(Ne+D) = 0.60 was fired into the post-disruptive plasma so that the pellet entered the plasma ~10 ms after the disruption was initiated by MGI, see #95148 in figure 23. It should be noted that pulses shown on figure 23 were originally presented in [12–15], but more details are given here.

In fact, the pellet in #95148 pulse was split into two large fragments (and possibly another small fragment in front), which can be seen on figure 23(d) and left frame on figure 24. In the reference pulse #95149, in which SPI fired at the 'healthy' plasma, the pellet looks like a single fragment with perhaps an additional small fragment in the tail. Although the SPI fired in different plasmas in #95148 and #95149, the pellet integrity is also different, the CQ rates are very similar, in figure 23(a) shows by the red and green curves. In pulse #95148, the first large fragment of the pellet flew through the plasma, which indicates that the cold post-disruptive plasma cannot fully assimilate even less than half of the small pellet C, right frame on figure 24. The second large fragment become invisible (Ne I radiation) when I_p drops to about 1 MA, but the pellet is still in the bulk plasma, which may indicate that most of the Ne atoms are ionized. However, more data and modelling are needed to better understand this observation. Moreover, taking into account that the CQ in pulses #95148 and #95149 has approximately the same I_p rate, it can be concluded that both hot and cold plasmas will 'digest' the amount of injected material to maintain the lowest possible plasma temperature, which ultimately determines the duration of the CQ.

During the CQ (after major disruption initiated by MGI), the pellet causes a minor disruption, which is accompanied by a characteristic MHD burst, figure 23(c). Here we can assume that a minor disruption followed by a fast CQ interrupts the vertical motion of the plasma centroid. It is worth mentioning that, like #95106

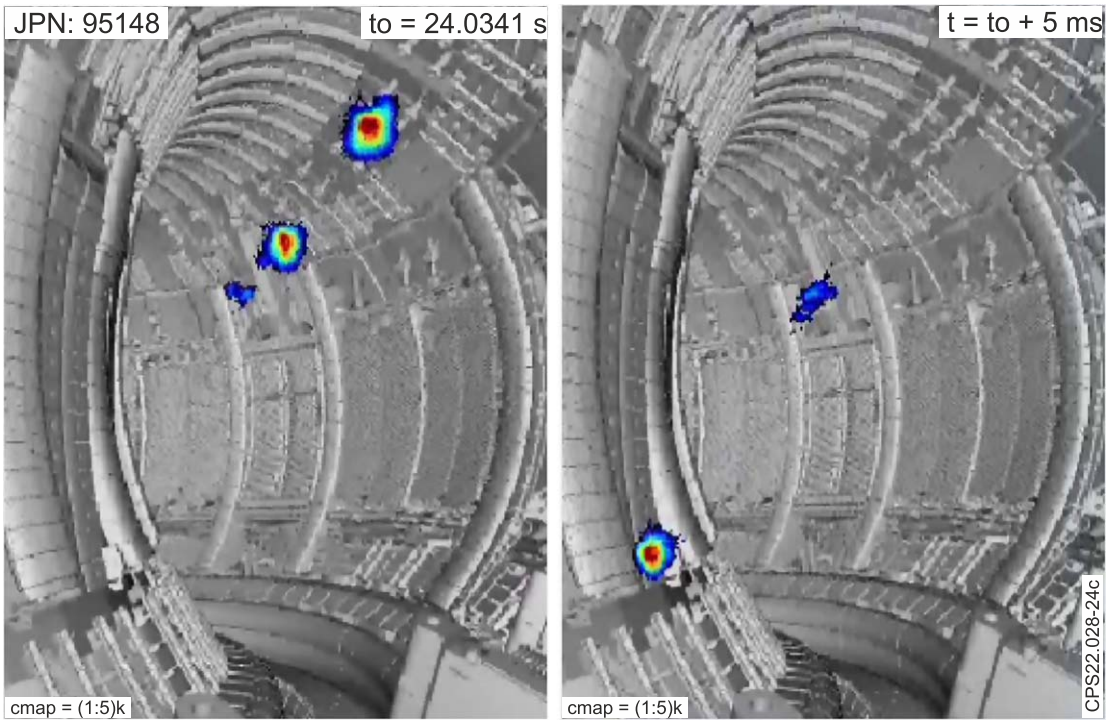

Figure 24. Ne I image of small broken pellet C. The time corresponds to the vertical dotted lines in figure 23.

(figure 22(b)) a cold VDE also developed during the slow CQ in the reference #95145 pulse, figure 23(b). A similar effect, namely, the loss of plasma vertical stability due to a minor disruption caused by a small amount of MGI gas in the AUG, was noted in [44].

Comparing two pulses when the identical pellets are fired at post-disruptive (#95148) and 'healthy' plasma (#95149), it can be seen that SPI efficiency, in terms of τ_{80-20}, does not depend on the state of the plasma, figure 23.

Thus, post-TQ plasma can be effectively mitigated, thereby prevent first wall melting. It can also be tentatively concluded that cooling and TQ phases are not significant for efficiency of the SPI to mitigate CQ when pellets content a sufficient amount of Ne for a given plasma.

The following section 6 presents data from demonstration of suppression of a VDE with SPI.

6. Suppression of AVDE by SPI

In JET, the non-mitigated disruptions usually occur as asymmetrical disruptions that are accompanied by sideways forces and in turn cause noticeable sideways displacements of the JET vacuum vessel [4, 19, 45–47]. Moreover, the sideways force can rotate and if the frequencies are close to the structural natural frequencies of the machine components, this can cause major dynamic amplifications of the loads [19, 48]. On JET, the duration of the CQ and, accordingly, the duration of rotation is short compared to resonance period of the vessel [49]. Thus, dynamic amplification of the sideways force is not an issue on JET. However, in ITER the situation can be reversed, namely the duration of rotation can be greater than the resonance period [50], so there may be a problem of resonant amplification of the sideways force.

Direct measurement of sideways forces on JET (and any other machines) is not possible, however the sideways forces can be estimated from the first plasma current vertical moment (M_{IZ}) which are directly measured by magnetic diagnostics:

$$F^{Noll} = \frac{\pi}{2} B_T \Delta M_{IZ}, \tag{1}$$

where

$\Delta M_{IZ} = \sqrt{\Delta M_{IZ51}^2 + \Delta M_{IZ73}^2}$ is the modulus of the first vertical plasma current moment with $\Delta M_{IZ51} = M_{IZ5} - M_{IZ1}$ and $\Delta M_{IZ73} = M_{IZ7} - M_{IZ3}$, where M_{IZI} for octant 1, etc. Formula (1) was proposed by Noll in [45] and neatly deduced by Riccardo in [51]. Later it was shown by Zakharov that formula (1) gives the upper estimation for sideways force [52].

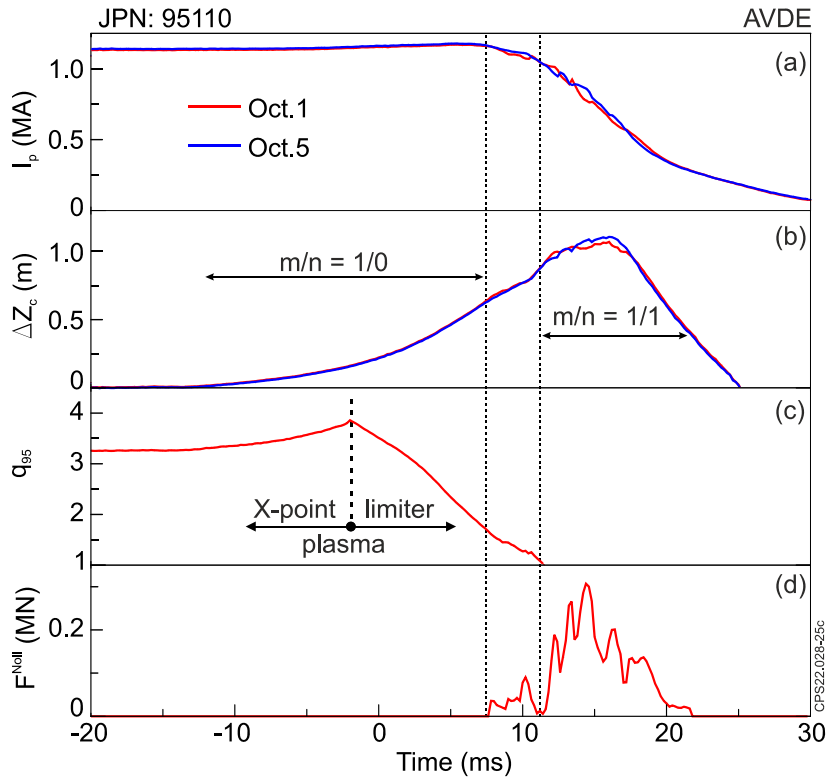

Figure 25. Two phases of VDE: axisymmetric ($m/n = 1/0$) and asymmetric ($m/n = 1/1$): (a) plasma currents, (b) plasma current vertical displacements, (c) safety factor from standard EFIT reconstructions, (d) sideways force calculated by Noll's formula. The time axis is zeroed to T_{dis}.

As mentioned above a direct measurement of sideways forces is not possible, however the sideways forces are responsible for the sideways displacements of the vessel. The vessel sideways displacements are measured at vertical ports of each octant with respect to the JET mechanical structure [51]. The large database on JET shows sideways vessel displacement with proportionality to the directional impulse of sideways forces, calculated by expression (1), thus, JET data confirm the validity of Noll's formula [4].

Noticeable sideways vessel displacement and sideways forces exist in a large proportion of JET non-mitigated disruptions, where the development of the plasma toroidal asymmetry precedes the drop to unity of q_{95} [4]. The VDE always creates conditions for plasma toroidal asymmetry, i.e., sideways forces, and because of this a VDE on JET is called an Asymmetric VDE, seen in figure 25. The safety factor q_{95} starts to decrease after plasma transition from X-point to limiter configuration, which creates the conditions necessary to grow the low m, n kink mode. The AVDE has two phases, namely a first axisymmetric phase which is mainly pure vertical displacement ($m/n = 1/0$ mode) and a second asymmetrical phase characterised by $m/n = 1/1$ dominated mode [4, 19]. Therefore, sideways force and vessel sideways displacement start in the second phase of AVDE [4]. Sometimes between these two phases one can see a weakly pronounced toroidal asymmetry in the region $2 > q_{95} > 1$, presumably an $m/n = 2/1$ mode, figure 25. The plasma current centroid vertical position calculated as $Z_{c1} = I_{p1}/M_{IZ1}$ with I_{p1} = octant 1 plasma current and M_{IZ1} = octant 1 first plasma current vertical moment etc, then plasma current centroid vertical displacements $\Delta Z_{c1} = Z_{c1} - Z_{oc}$ with Z_{oc} = pre-VDE plasma current centroid vertical position.

Since 2011, JET-ILW has been operating with an all metal Be/W composition wall which was originally planned for ITER [53]. In JET-ILW, high heat fluxes (or alternatively runaway electrons or arcs) have led to damage of PFC by beryllium melting and thermal fatigue of tungsten [39, 54]. The AVDEs are especially dangerous due to high heat flux density and plasma surface currents that the plasma shares with the 'wall' in wetting zone [4, 19, 47, 55].

Early operation of the JET-ILW can be divided into three slots: 2010–2012 (ILW-1), 2012–2014 (ILW-2) and 2014–2016 (ILW-3). The first indications of melting of beryllium were mentioned in [55], and consistent data on Upper Dump Plate (UDP) melting with focus on the ILW-2 (2012–2014) operational campaign was described in [54]. There were 14 upward VDEs between JPN 84408–84950, and the visual inspection of UDP tiles performed before and after JPN 84408 shows signs of melting, as shown in figure 7 of [54].

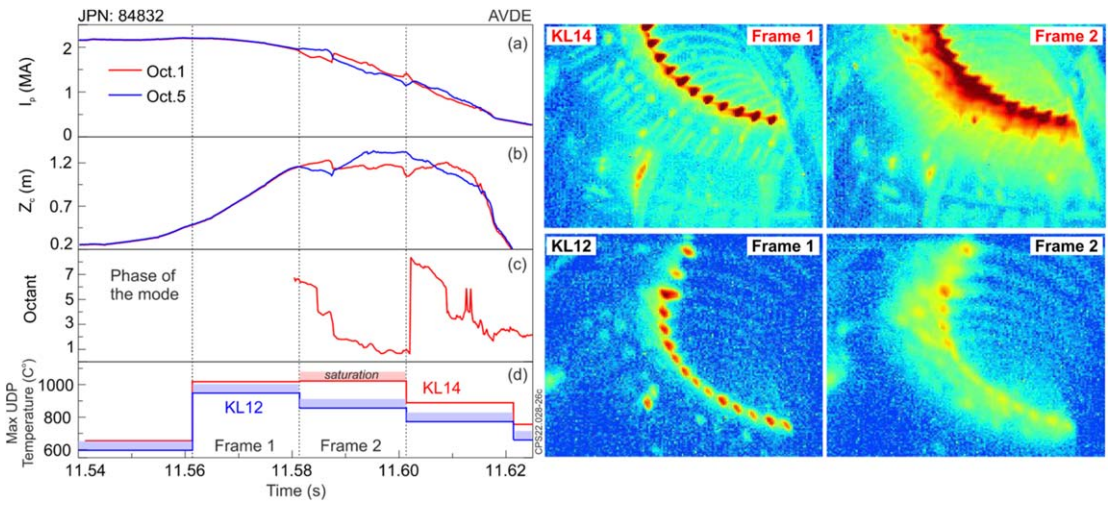

Figure 26. Asymmetric VDE heating of beryllium UDP, left: (a) plasma currents, (b) plasma current centroid vertical position, (c) phase of the mode, (d) maximum temperature of the UDP recorded by the cameras KL14 and KL12. Right images: Frame 1 and Frame 2 of KL14 and KL12 infrared cameras, Be temperature range: (500–1000)°C.

JPN 84832 provides a unique opportunity to demonstrate the effect of AVDE on UDP, figure 26. The VDE on this pulse arose due to a fault of the plasma vertical position control system. The first phase of the VDE with duration of ~15 ms leads to an increase in the temperature of the beryllium UDP but still below the melting point of 1278 °C. At this phase the temperature rises approximately evenly on opposite sides of the machine (specifically in octants 3,4 and 7,8), which is recorded by calibrated infrared cameras, figure 26(d). The second asymmetrical phase of VDE starts at about t = 11.581 s, where the slowly rotating clockwise mode exists for about ~36 ms, figure 26(c). Thus, a toroidal asymmetric plasma-UDP wetting zone arises.

The mode phase calculated from the difference of the first current vertical moments of two pairs of orthogonal octants ΔM_{IZ51} and ΔM_{IZ73} shows the toroidal angle at which plasma touches the 'wall', namely a centre of wetting zone (figure 26(c)). The exposure time for Frame 2 covers a portion of the asymmetrical phase of the VDE during which the mode (a centre of wetting zone) rotated from Octant 6 through to Octant 1, passing through Octants 4 and 3 where it could be observed by the KL14 infrared camera.

In the plasma-UDP wetting zone, in addition to heat flux, the plasma surface current, that are necessary for plasma equilibria, must be shared by the plasma with the edges of the UDP. Presumably, on the opposite side, the plasma detached from the UDP. The asymmetric temperature behaviour is clearly observed during asymmetrical phase of AVDE, seen in comparison between Frame 2 of each camera in figure 26.

The standard ('intershot' in JET jargon) EFIT reconstruction at the last stage of the VDE axisymmetric phase shows that plasma sits on the low field site of the UDP, figure 27(a). Figure 27(b) highlights the total melt accumulation on the low field site of the UDP as an effect of all VDEs during the ILW-2 (2012–2014) JET operational campaign.

To avoid plasma toroidal asymmetry and correspondingly sideways forces and asymmetric thermal load on the wall, it is necessary to prevent q_{95} dropping below ~1.5 by interrupting uncontrollable vertical motion of the plasma.

JET shows that massive gas injection (MGI) is a reliable tool to mitigate plasma toroidal asymmetry during the CQ. The MGI, which is compulsorily used to mitigate disruptions, significantly reduces the I_p asymmetries in JET [4].

Testing the effectiveness of SPI on the upper AVDE was done using ohmic #95110 (where the pellet fired but missed the plasma) as a reference pulse with $I_p = 1.14$ MA and $B_T = 1.2$ T, seen in figure 25. A small pellet C with Ne/(Ne+D) = 0.60 was fired prior to the preprogramed VDE so that the pellet arrives at a desirable time during the VDE, figure 28. The arrival of the pellet obviously causes a TQ, followed by a fast CQ. As result of this, the exponential vertical movement of plasma current centroid vertical displacement is interrupted, namely vertical displacement evolution goes into a stationary state or reverses with a slow motion. Moreover, the drop of q_{95} is reversed, which prevents the development of AVDE, and therefore completely eliminates (up to the noise level) or significantly reduces the sideways forces. The effectiveness of SPI can be estimated from the modulus of impulse of sideways force, $Imp = \int F^{Noll} dt$. Table 3 summarises the effectiveness of SPI on AVDE, where $\Delta T_{zs\text{-}pa} = T_{zs} - T_{pa}$ is difference between the time the pellet interrupts a VDE (T_{zs}) and when the pellet arrives in the plasma (T_{pa}), ΔZ_{ca} is plasma current centroid vertical displacement at T_{pa} and ΔZ_{zs} is plasma current

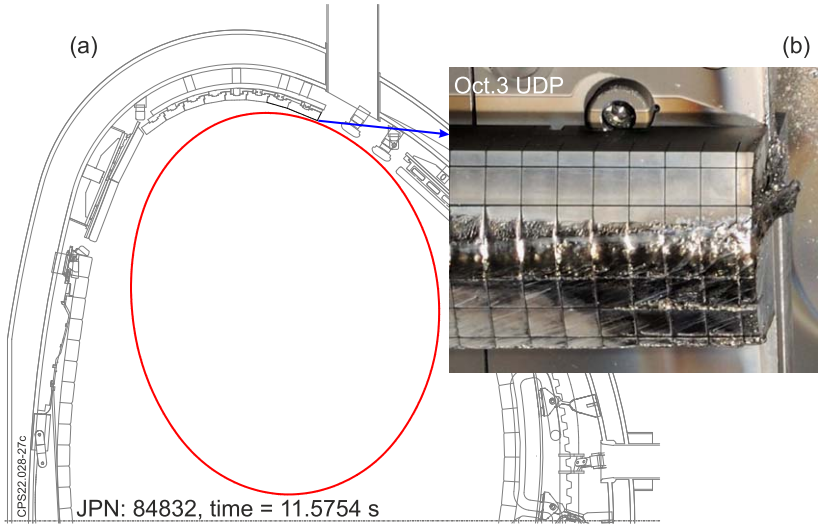

Figure 27. (a) EFIT reconstruction shows in the end of axisymmetric phase of VDE, see figure 26. (b) shows the cumulative melted damage on the low field side of the UDPs during the inspection performed at the end of the 2012–2014 JET operational campaign.

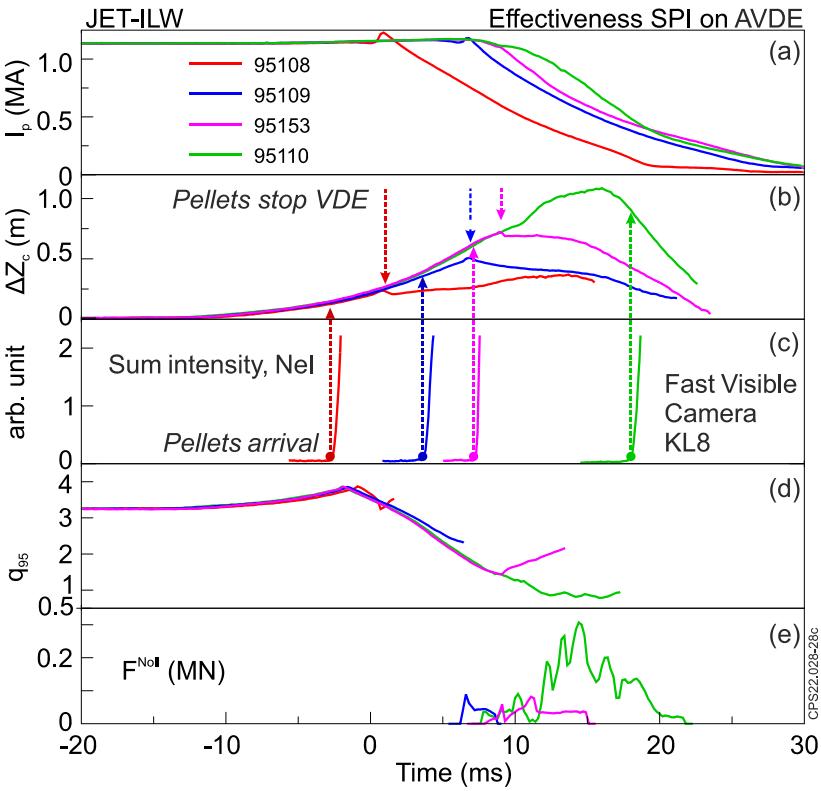

Figure 28. The suppression of VDE by SPI, pellets instigate TQ followed by fast CQ. Pellets stops exponential vertical movement of plasma: (a) plasma current, (b) vertical displacement of plasma current centroid, (c) Ne I intensity, (d) safety factor, (e) Noll's sideways force. The time axis is zeroed to T_{dis}.

Table 3. Effectiveness of the SPI, pellet C with Ne/(Ne+D) = 0.60, on AVDE.

JPN	$\Delta T_{zs\text{-}pa}$ (ms)	ΔZ_{pa} (m)	ΔZ_{zs} (m)	$\Delta Z_{pa}/a$	$\Delta Z_{zs}/a$	Imp (kNs)
95108	3.50	0.12	0.23	0.13	0.24	0
95109	3.20	0.36	0.50	0.38	0.53	0.01
95153	1.80	0.64	0.72	0.67	0.76	0.2
95110	N/A	0.98	N/A	1.03	N/A	1.4

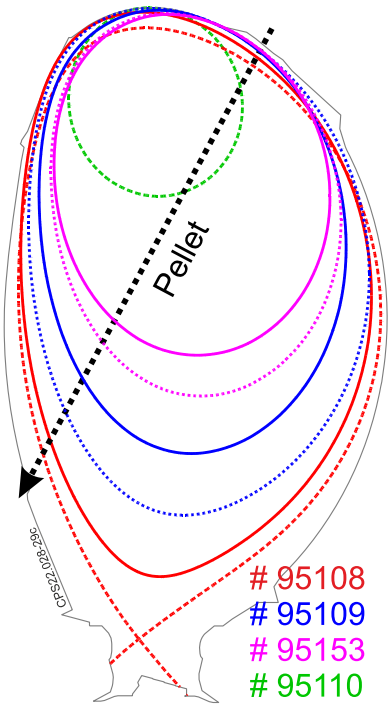

Figure 29. Plasma configurations at the time of the arrival of the pellets (dotted line) and stoppage of the vertical movement of plasma (solid line). The direction of the pellet's trajectory is shown by the black dotted line.

centroid vertical displacement at T_{zs}, here ΔZ is relative to pre-VDE plasma vertical position and $\Delta Z/a$ is ΔZ normalised on pre-VDE minor plasma radius.

The JET pellet trajectory was optimal for the upwards VDE, figure 29. Thus, the shattered pellet plume flies in direction of the plasma centre even with a large vertical displacement of the plasma. From table 3 it can be seen that the pellets which arrive in the early phase of the VDE (#95108 and #95109, $\Delta Z_{pa}/a \leqslant 0.38$) significantly eliminate the sideways impulse: more than 100 times reduction in sideways force impulse compared to non-mitigated VDE. Even when a pellet enters a developed VDE (#95153, at $\Delta Z \approx 0.67a$) a decrease in impulse is still noticeable, namely by a factor of 7. It is worth mentioning that there is a delay of several milliseconds (table 3, ΔT_{zs-pa}) between the moment the pellet enters the plasma, and the moment pellet instigates a disruption, which is effectively terminates the hot VDE. Moreover, the $\Delta T_{zs\text{-}pa}$ delay decreases for a plasma with a large vertical displacement, apparently due to the fact that the plasma and the pellet move towards each other.

7. Effectiveness of SPI on axisymmetric forces

Electro-magnetic loads are due to the current flowing during the CQ in the conductive vessel [4, 5, 19, 46]. On JET, the consequence of EM loads is a complex oscillatory deformation of the vessel with main axisymmetric roll and asymmetrical sideways modes of movement of the vessel [49]. The vessel reaction forces are measured by 4 strain gauges installed on the restraints between vessel and the mechanical structure in each octant, respectively, 32 gauges in total. The vertical vessel reaction force is calculated as the average projection of all measured octant forces onto the vertical axis. Then, for each pulse, the magnitude of the axisymmetric vertical vessel reaction force, F_z, is defined as a maximum peak to-peak in measured force over time.

Here it is necessary to emphasize the difference between the vessel reaction force and force acting on vessel during disruption, F_v. The F_v depends on the instantaneous value of the plasma current, as $F_v \sim I_p^2$. However, the integral effect of the F_v force on a vessel depends on the force impulse. Nevertheless, the measurable magnitude of the vertical vessel reaction force, F_z, is a parameter that has been used as one of the essential criteria for the safe operation of JET.

The magnitude of the vertical vessel reaction forces as a function of pre-disruptive plasma current I_p^{dis} over the large JET disruption database is shown on figure 30. It was thought that F_z depends mainly on the $(I_p^{dis})^2$. In figure 30, the black dotted line is the upper bound of non-mitigated disruptions and the blue dashed line is the upper bound of SPI and MGI mitigated disruptions, where both lines use the functional relationship $\sim I_p^2$. We believe that for $I_p^{dis} \geqslant 2.5$ MA the experimental points do not rise to the upper bound of non-mitigated disruptions because the database is limited for large plasma current. Data such as that shown in figure 30 was

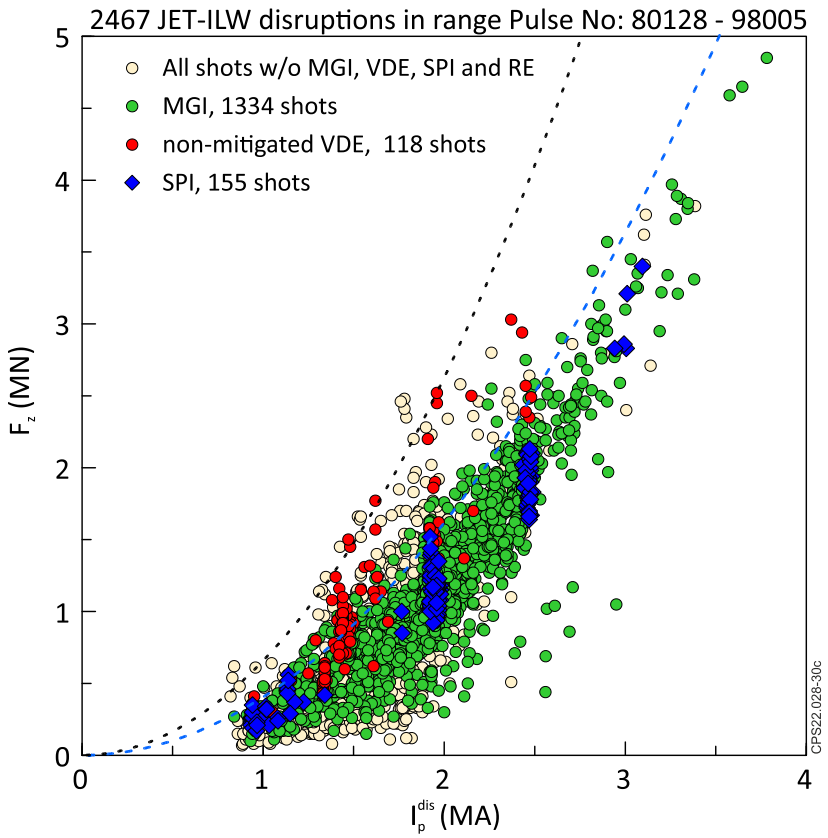

Figure 30. The magnitude of the vertical vessel reaction force as a function of pre-disruptive plasma current. Black dotted line is the upper bound of non-mitigated disruptions. Blue dushed line is the upper bound of SPI and MGI mitigated disruptions.

used by the JET Machine Protection Working Group (MPWG) to make the case for using MGI to mitigate disruption. The difference between upper bound of non-mitigated disruptions (black dotted line $f_1 = 0.65 \cdot I_p^2$) and the upper bound of SPI and MGI mitigated disruptions (blue dashed line $f_2 = 0.4 \cdot I_p^2$), which are two parabolas, is 38 %, figure 30.

Thus SPI (and MGI) reduce the axisymmetric vertical vessel reaction forces by about (30–40)% compared to unmitigated disruptions, which the MPWG considered to be a significant benefit. Here, we can conclude that the mitigation of vertical force F_z can be equally performed by both SPI and MGI.

However, it should be noted here that JET MGI mainly uses a gas mixture of 90% D_2 + 10% Ar (corresponding to 95.7% D atoms + 4.3% Ar atoms) [2], while SPI experiment mainly carried out with pellet (D_2 + Ne) which is intended for use at ITER. Also, according to JET's experience, the effectiveness of an MGI depends on the particular design of the MGI [2], but on the other hand, pellet fragments can fly through the plasma without assimilation. Therefore, a direct comparison of SPI to MGI is not trivial, and any attempt to compare SPI to MGI should be treated with great caution.

8. Discussion

This paper presents various aspects of the SPI experiments conducted with 'healthy' and post-disruptive plasma at JET in 2019–2020. The pellet plasma interaction started with pre-TQ cooling phase, when pellet material cause cooling of the plasma periphery, then an MHD phase, which includes the TQ as the initial phase followed by current quench.

Plasma disruptions cause large mechanical stresses on the tokamak components, which are detected on JET as a complex, damped vessel oscillation, where the main motion modes are axisymmetric roll and asymmetric sideways displacement. There is a peak displacement of the vessel in the order of several millimetres, while the vessel can also experience violent mechanical forces in excess of a few MN [2, 4].

Both 'hot' and 'cold' AVDEs are dangerous for two reasons: firstly, the plasma surface currents that the plasma shares with the 'wall' can melt beryllium PFCs [56], and secondly, AVDEs can create large sideways forces acting on the vessel. Both destructive impacts were observed on JET-ILW. On JET the VDE always creates conditions for plasma toroidal asymmetry and because of this the VDE on JET is called an Asymmetric VDE.

The VDE has two phases, namely axisymmetric with dominant mode $m/n = 1/0$ and asymmetric with dominant mode $m/n = 1/1$. Thus, VDE mitigation must be performed at the initial axisymmetric phase.

JET experiments have demonstrated the interruption of a hot VDE with SPI. A small pellet C was fired prior into 1.2 MA Ohmic plasma with the preprogramed VDE so that the pellet arrives at a desirable time during the VDE. The pellet instigates a disruption, namely TQ followed by fast CQ. Presumably, the current which the plasma shares with the 'wall' (and maybe the induced vessel current), completely changes the time evolution of the plasma current centroid vertical position (Z_c). The exponential Z-movement is interrupted, and vertical movement goes into a stationary state or reverses with a slow motion. At the same time, the rate of I_p drop increases, which leads to an increase or stops the drop in safety factor q_{95}. This apparently excludes the excitation of the $m/n = 1/1$ kink mode responsible for AVDE which causes a large sideways displacement of the vessel. Thus, the main result of the experiment was prevention of AVDE by SPI: the exponential growth of the plasma current centroid vertical position is interrupted and Z_c stabilised. In this regard, the effect of SPI is similar to the effect of MGI [2].

The reason why a disruption 'stops' VDEs is still an open question, and it is a subject of the future experiments and simulations. However, two hypotheses have been proposed so far, both related to the current shared by the plasma with the 'wall', which are briefly described below.

Hot VDEs are usually not associated with conventional plasma disruptions, i.e., the thermal quench and current/voltage spikes. On JET, conventional plasma disruptions, regardless of the cause of the disruption (SPI, MGI or 'natural'), have been found to interrupt VDEs in terms of plasma current centroid vertical motion (the subject for other publication).

It is believed that a conventional plasma disruption is associated with kink modes $m \geqslant 2$. Thus, a possible reason for such VDE stabilization could be the contact of the plasma with conducting plasma facing components ('wall') due to the developed $m/n = 2/1$ helical deformation of the plasma boundary. At some toroidal angle the plasma surface touches both low and high field sides of the conducting 'wall'. The result is an electrical circuit (in fact, two of them: below and above the plasma) which embraces the magnetic flux of a strong toroidal field. Fast vertical displacement becomes prohibited due to the conservation of the toroidal magnetic flux. The inductively excited plasma-wall currents compensate the vertical driving force and provide the force balance in vertical direction, thereby considerably slowing down the vertical motion.

Another possible explanation, proposed by Artola based on the 2D JOREK modelling [57], is that during the VDE, even after TQ, the exponential motion of the core plasma continues in the same direction. However, due to the fact that the temperature of the core plasma drops and becomes similar to the temperature of the halo plasma, a flat toroidal current profile fills the entire area inside the 'wall'. Thus, plasma core and plasma current centroid motions become independent. This means that SPI (or the TQ) stops the VDE only from the point of view of the plasma current centroid, but not from the point of view of the plasma core. Recent 2D simulations with the extended MHD code JOREK generally support Artola's explanation [58]. Both experimental evidence and meticulous modelling are needed to confirm these hypotheses.

Now we want to touch on the topic of TQ as the initial disruption phase, which is not only important for experimenting with SPI, but is of more fundamental importance. The internal MHD instabilities (such as internal reconnections [59]), as a widespread explanation are associated with a single toroidal wave number n (typically $n = 1$) of Neoclassical Tearing Mode (NTM) or Resistive Wall Tearing Mode (RWTM) [60], which drives islands on separate resonant surfaces $nq = m$.

Numerical modelling of #95149 pre-TQ cooling and TQ phases using M3D-C1 was presented in [61]. The modelling uses an extended-MHD code developed for the study of non-linear transient events in tokamaks, together with a neutral gas shielding model for the ablation of frozen pellets within the plasma, and the non-coronal equilibrium model KPRAD for tracking impurity charge states and radiation. In both 2D and 3D, this modelling shows a pre-TQ evolution of radiation and temperature profiles consistent with experiment. According to simulation, only a very small amount (~4%) of neon is ablated during pre-TQ cooling phase. In the 3D simulation, a progressive destabilisation of 2/1 and 3/2 MHD modes was observed in the pre-TQ cooling phase, then instability causes the onset of TQ.

Simulation of radiation response and the MHD destabilization during the TQ, with 3D non-linear MHD simulation using the JOREK code, can be found in [62]. According to simulation of JET, with almost no $q = 1$ surface and a lower shear near the $q = 2$ surface, the 2/1 mode is able to nonlinearly couple with the 3/2 mode in the core thus triggering the TQ when the fragments arrive on the $q = 2$ surface. A strong radiation toroidal asymmetry was found before and during the TQ which gradually relaxes during the TQ and is completely eliminated by its end. However, this simulation result appears to be inconsistent with the JET observations, as shown in figures 16 and 17, where a strong toroidal asymmetry of the Ar^+ ions is visible even during the first half of the CQ. According to JOREK simulations, the global field line stochasticity exists even at the onset of the TQ, however it still takes many turns to travel between the core and the edge region along the field lines. Thus, high parallel electron thermal conduction is able to lower the core temperature, on the other hand the parallel

transport of injected materials from the edge into the core is slow. Later as stochasticity grows, the core becomes easily accessible from the edge. According to simulation of JET case (figure 4 in [62]), only 10% of the injected Ar accumulates at the end of TQ, which seems to be consistent with figure 16.

According to the JOREK and M3D-C1 models, stochasticity of magnetic field can happen only due to non-linear effects of the internal mode as a result of pre-TQ cooling. It is worth noting here that plasmas can exist with low $q(a) \approx 1.5$ in tokamak discharges, including on JET [2]. Moreover, a full-scale (in term of the I_p spike) disruption can occur even after the TQ i.e. in a cold plasma, see #94579 in figure 22. Thus, pre-TQ cooling and TQ are not absolutely necessary conditions for the onset of the MHD phase of a disruption.

The remarkably fast thermal quench in the plasma centre (#95149, figures 7 and 9) distinguishes the Wall Touching Kink Mode (WTKM) [52, 63] as the reason of TQ from other interpretations based around internal reconnections [59]. The WTKM mode is a free boundary kink mode which is the strongest and fastest kind of MHD instability in tokamaks. The WTKM is also consistent with JET observations of visual wall touching throughout the entire MHD phase (from the beginning of TQ to the end of the plasma current spike) when magnetic perturbations are also detected.

This mode makes plasma touch the wall structure in a toroidally localized zone, which generates a wide spectrum of both poloidal and toroidal wave numbers m, n. The WTKM generates electric currents in the wall (called Hiro currents) which are always opposite in direction to the bulk plasma current. This generates the well-known 'negative' voltage spike in disruptions, while the resistive decay of the 'negative' Hiro currents leads to the positive spike visible in plasma current measurements.

9. Summary

The presented data refer to the SPI experiments (with the pellet diameter of [4.57, 8.1, 12.5] mm and mainly Ne+D_2 composition) carried out at JET in 2019–2020. This study provides extensive experimental data on the interaction of pellets with plasma and associated disruptions. Below we list the key findings of this study:

- SPI efficiency, in terms of τ_{80-20}, does not depend on the state of the plasma, 'health' or post-disruptive.
- A pellet with a high content of Ne or Ar can reduce the CQ duration to below the upper required JET threshold, $\tau_{80-20} < 27.5$ ms, for plasma up to 3 MA and the pre-disruptive internal plasma magnetic energy up to 15 MJ. However, τ_{80-20} never dropped below 10 ms that the lower required JET threshold.
- Injecting additional amount of Ne does not provide any further reduction of the τ_{80-20} for 'healthy' plasma (Ohmic, $\leqslant 2$ MA). If pellet is large enough then pellet fragments will fly through the plasma without assimilation.
- Plasmas with a high pre-disruptive plasma energy require pellet with a high content of Ne or Ar to obtain a short CQ duration, provided that the pellet does not fly through the plasma.
- The Ne fraction in the pellet does not affect the CQ duration except for pellets with a small fraction of Ne, namely when Ne/(Ne+D) < 0.5. Moreover, pellets with a very small amount of Ne ($\sim 1 \cdot 10^{21}$) and low Ne fraction, Ne/(Ne+D) ≈ 0.1, instead of causing a mitigated CQ, create the conditions for a 'cold' VDE.
- The duration of the pre-TQ cooling phase depends mainly on the speed of fired pellet, the duration corresponds to the time required for T_e cold front (in terms of Ne I image) to reach the magnetic surface at ~½ of the minor radius.
- The interrupting of VDE and prevention of AVDE with SPI has been demonstrated.
- The disruption mitigation with SPI or MGI reduces the axisymmetric vertical vessel reaction forces by about (30–40)% compared to unmitigated disruptions, which is considered a significant benefit.

JET unique experimental data that can help to improve the understanding of disruptions and to develop and to calibrate models, which could be used to predict the loads with future machines, such as ITER.

Acknowledgments

This work has been carried out within the framework of the EUROfusion Consortium, funded by the European Union via the Euratom Research and Training Programme (Grant Agreement No 101052200 - EUROfusion) and from the EPSRC [grant number EP/W006839/1]. To obtain further information on the data and models underlying this paper please contact PublicationsManager@ukaea.uk. Views and opinions expressed are

however those of the authors only and do not necessarily reflect those of the European Union or the European Commission. Neither the European Union nor the European Commission can be held responsible for them. The JET SPI experiments have been carried out as collaboration between EUROfusion and the ITER Organization. The JET SPI has received funding through the ITER project. The views and opinions expressed herein do not necessarily reflect those of the ITER Organization. The work was also supported in part by the U.S. Department of Energy under Contracts No. DE-AC05-00OR22725, grant DE-SC0023274 and by the US Department of Energy, Office of Science, Office of Fusion Energy Sciences under Award No. DE-FG02–06ER54852 . The authors would like to acknowledge G Szepesi, V Drozdov and P Abreu for support in providing and interpreting EFIT data, YuF Baranov for help in assessing ECE, L N Khimchenko and R Henriques for help in interpreting the radiation data. The authors would like to acknowledge O Sauter, A Javier, R Khayrutdinov and E Nardon for fruitful discussions on the impact of SPI on VDE.

Data availability statement

All data that support the findings of this study are included within the article (and any supplementary files).

Appendix A. JET shattered pellet injector system

In 2019, the three injection barrels of SPI and a gas manifold system supplied by Oak Ridge National Laboratory (ORNL) were installed at JETILW together with the appropriate vacuum, cryogenic, mechanical and control hardware [14, 16, 21]. The JETILW SPI system is based on the design that was used on DIII-D [22].

The SPI is mounted in Octant 1 vertically on the top of the machine, see figure 1 and figure 31 (see also figure 1 in [14], figure 3 in [16]). The pellet injector replaced Disruption Mitigation Valve (DMV) #1, the original fast acting valve of the JET MGI system [3, 4, 64].

The SPI system has three different sized barrels in which the pellets are created. The injector can deliver D_2, H_2, Ne, Ne with D_2 shell, Ne+D_2 mixture, Ar and Ar + D_2 sandwich pellets. The geometric parameters of the pellets are presented in table 4.

Pellets are formed in the cold head area in the injector barrels, figure 32(a). The length of the cold head zone determines the pellet length. The pellet injector is arranged to propel the pellets vertically downwards along a flight tube through the Microwave Cavity (MWC), figure 32(c).

The SPI shatter tube, which fits into a guiding tube, is in the Intermediate Vertical Port in Octant 1 sector D. A flight tube guides the pellets along the circa 5 metres path to the vacuum vessel. The flight tube is not

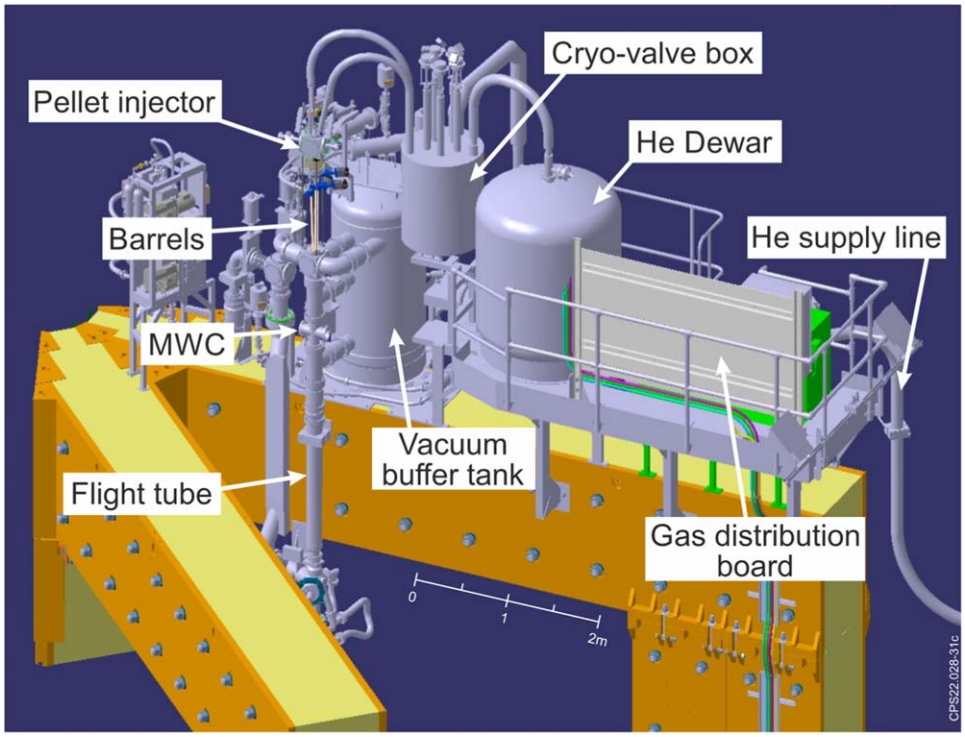

Figure 31. General view of the SPI installation in Octant 1.

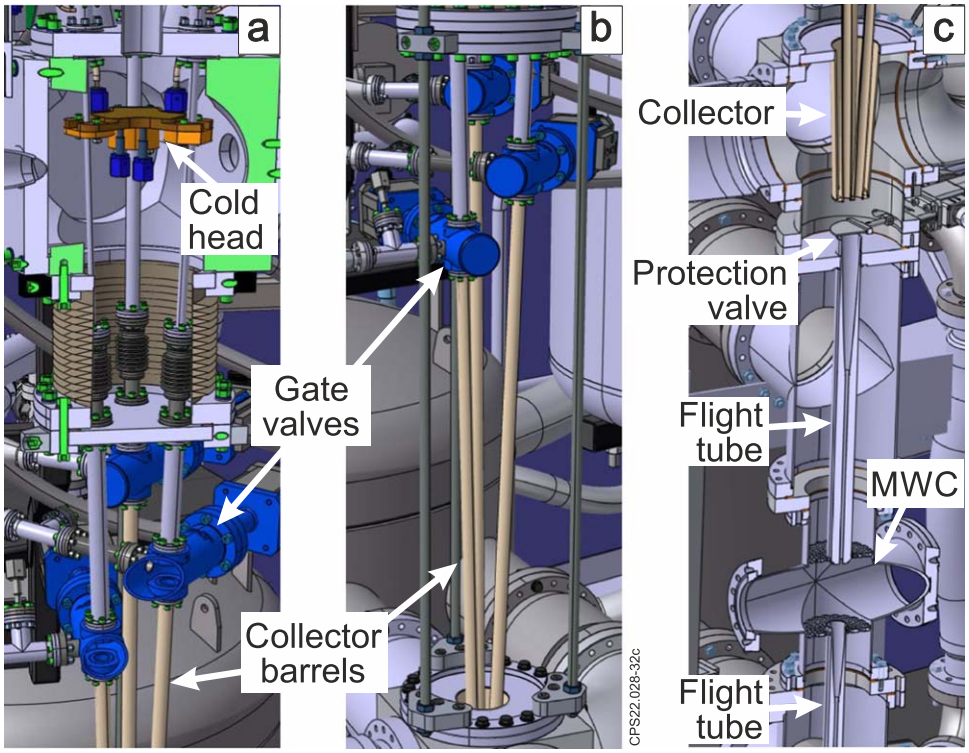

Figure 32. The sequence of the pellet route from (a) Cold head of the injector, then (b) through Gate valves and Collector barrels to (c) Collector and Flight tube with Protection valve to the Microwave Cavity (MWC) and next Flight tube to the vacuum vessel.

Table 4. Pellet geometrical parameters.

Pellet	Diameter (mm)	length/diameter ratio
C	4.57	1.4
B	8.1	1.6
A	12.5	1.54

continuous but has several breaks to allow for a MWC diagnostic, pumping gaps for removing the propellant gas and valves (see for details [16]). The sequence of the pellet route starts with the cold head of the injector (figure 32(a)), then through gate valves and collector barrels (figure 32(b)) to the collector, where pellets are collimated with a shallow funnel into a single injection line, to the flight tube with a protection valve before the MWC and then to the next flight tube (figure 32(c)). After that the pellet enters the SPI shatter tube which has an S-bend and a final sharp bend at its exit to shatter the pellet just before its entry into the JET vacuum vessel at an angle of ~28.4 degrees to vertical, figures 2 and 35. The purpose of the 'shattering element' is to fragment the pellet into small shards, increasing the surface area of the pellet material and distributing the pellet material over an increased angle. The spray of shards is directed towards the inner wall of the vessel within a 15-degree half angle cone [16].

The total path of the pellets from the cold head of the SPI (where the pellets are formed) to the vessel (the point of exit of the pellets) is 6654 mm, which consists of 1932 mm passage from the cold head to the MWC and 4722 mm from MWC to the point of entry to the vessel.

The pellets are fired by high-pressure propellant gas, where the ejection of a pellet occurs either due to the gas blow itself, or with the help of a mechanical punch driven by the propellant gas. The propellant gases are removed as much as possible to avoid propellant gas influencing the plasma before the solid shattered pellet material arrives. On JET SPI experiments the propellant valves are operated with propellant gas pressures of 50–58 bar D_2.

Initial commissioning was carried out without pellet firing, with the propellant gas alone being fired into the empty JET vacuum vessel. With valves closed on the pumping ducts, less than 0.4% of the propellant gas fired with no pellet was measured in the torus. Thus, most of the propellant gas being pumped away by the vacuum system from several points along the flight tube [16]. Another test was carried out when propellant gas was fired

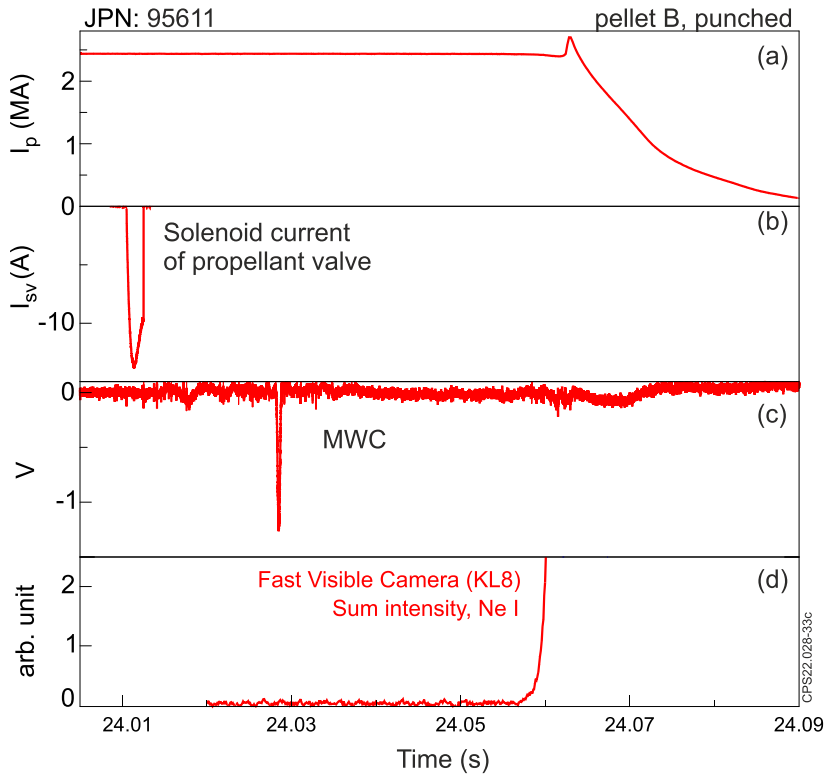

Figure 33. The sequence of events during SPI experiment from propellant valve opening to disruption: (a) plasma current, (b) solenoid valve current, (c) MWC diagnostic records pellet presence and time, (d) fast camera shows the arrival of a pellet in the plasma.

into an empty torus, where 2 mbar•l was measured. With a pellet it will be even less since the pellet helps deflect the gas sideways when crossing the gaps.

Operation of the cryo-system showed it was possible to reach temperatures of 7 K in the SPI cold head. Pellet formation was typically performed between (7–9) K for Neon and Deuterium to ensure pellet reproducibility. It takes four hours to pressurise the liquid He (LHe) dewar and then a further 2 h for the cold head to reach the operational temperature from room temperature once the gaseous He (GHe) flow is switched on. The temperature obtained is very stable with some slight drift due to the changing pressure in the LHe dewar.

In the initial stage of commissioning, pellets of different species were formed without firing them. Known quantities (volume and mass) of gas were fed into the cold head barrels which then corresponds to the volume (and mass) of the solid material contained in the pellet. These test pellets were sublimated by closure of the return line of the GHe to raise the temperature of the head to 30 K. The rapid sublimation of the largest pellets was a challenge for the vacuum system, necessitating the isolation of the turbo-pump. Formation of pellets that were not subsequently fired was generally avoided, where possible.

Firing the pellet without a punch had a reliability issue, namely the pure D_2 pellets fired reliably but a large fraction ($\geqslant$ 10%–20%) of Ne mixture pellets did not fire and were assumed to be stuck in the cold head of a barrel. This is due to the fact that the shear strength of neon is many times (~5) higher than that of deuterium (the shear strength of argon is three to four times stronger than neon at much warmer temperatures) [65].

Ne pellets could be fired with or without a shell being formed. However, Ne pellets prepared with 0.4 mm shell of deuterium fired mostly reliably and any pellets fired with the punch were fully reliable. Punches can be mounted on the two largest barrels, A and B; barrel C cannot be fitted with a punch. The punches were originally developed for use with Argon pellets, where in our experience it is not possible to obtain an Ar pellet with a deuterium shell. In our experience, attempting to create a D-shell Ar pellet results in Ar deposition at the outer ends of the pellet in contact with the barrel, and the argon does not fill the centre of the pellet.

The three barrels operate independently, thus the pellets in the three barrels can be fired independently or at the same time. The pellet may break during the acceleration process, which can potentially affect fragmentation during the shattering process [11].

To allow the pellet to be fired easily a heater in the head is switched on prior to the trigger to heat the pellet up to ~12 K. It should be noted that the head heating technique before pellet fire may not be possible to use for SPI in protection mode in a long pulse machine such as ITER.

The SPIs on JET utilize custom fast acting solenoid valves (figure 36) developed at ORNL for pellet applications. The valves have an internal plenum volume of 5 cm^3 and an external 75 cm^3 close coupled volume to provide enough gas to accelerate the pellet and to close the valve when the current pulse ends. These ORNL valves can open in less than 1 ms when actuated by a 180 V Field Effect Transistor switched power supply that provides a 30 A current pulse to the solenoid coil [16].

On JET, when the plasma and machine are ready, a trigger is given to the SPI control system and the solenoid coil is opened for the propellant valves to fire the pellets, which is achieved with a 2 ms 15 A solenoid current pulse, figures 36 and 33.

In 2022, the SPI has been upgraded to improve the integrity of pellets, arrival jitter of the pellets and better pellet speed control. The expected nominal pellet speeds are ~300 m s^{-1}, however, the speed can be increased by adjusting the propellant valve opening time to deliver more gas. The main 2022 changes are:

- barrels A-12.5 mm and C-4.57 mm have been replaced with new barrels with 10 mm diameter to allow multiple injection with identical pellets;
- the punches have been removed and inserts have been installed into all three-barrel breeches to reduce the breech volume for better pellet speed control.

One of the main changes with the SPI is the production of slower pellets that will result in larger fragments and much less gas formation when the pellet is shattered. The penetration of these fragments is predicted to be greater and therefore may change the mitigation characteristics.

The data presented in this paper refers to JET operations in 2019–20 only. It is worth noting that some parts of the JET SPI system are not compatible with tritium, therefore SPI was not tested during TT and DT operations.

Appendix B. Pellet speed

The pellet speed is an essential SPI parameter because when mitigation is needed, the mitigation action must be taken as soon as possible. On the other hand, the speed of the pellet affects how it shatters and how fragments of the pellet interact with the plasma. The distance of the pellet source from the plasma combined with the speed determine how quickly the mitigation can be performed.

The central length of the pellet trajectory from the centre line of the MWC (figure 34) to the exit point (figure 35) is 4722 mm. To enter the bulk plasma, pellets must also fly through the shadow of the limiters and the Scrape Off Layer (SOL) where the plasma has low density and temperature, figure 38. For a typical divertor configuration, the total thickness of the limiter shadow region and SOL is about 400 mm ≈130 mm (thickness of a shadow of the limiter region) + 270 mm (thickness of a SOL), thus the length of the pellet trajectory from the centre line of the MWC to the SOL is 4852 mm and to the separatrix is ~5122 mm.

The time of entry of pellets into the plasma can be determined using various diagnostics, namely the high-speed KL8 camera equipped with a special filter (Ne I filter for Ne+D_2 pellets or Ar I (Ar II) filter for pellets containing Ar), ECE, VUV and Mirnov coil, figure 39. However, VUV, MHD, interferometry and bolometry signals are not good candidates for detecting pellet entry into plasma, since these diagnostic data reflect the status of plasma sometime after pellet entry into the plasma. In addition, bolometry also involves an intrinsic delay due to thermal inertia (see also appendix C).

The Fast Visible Camera, KL8, and ECE edge channel ($\rho \equiv r/a = 0.96$, where a is the plasma minor radius) detect the arrival of the pellet at about the same time with diagnostic time resolution of +/− 100 μs, figure 39, whereas it would be expected that edge cooling would be delayed with respect to visual evidence of the pellet plume. One possible explanation could be that a small fraction of propellent gas may travel in front of the shattered pellet plume because the gas sound speed exceeds the speed of the pellet fragments [16]. However, this cause was ruled out by a test where propellant gas (He at nominal pressure) was fired without a pellet into a JET plasma. The plasma was not affected and none of the diagnostics showed any indication. A small amount of He, namely 2 mbar•l that was measured when propellant gas was fired into an empty torus, would not be expected to have influenced the plasma.

There are other sources of the gas, namely, the gas that formed during the flight of the pellet when interacting with the flight tube and funnels and the gas that formed during the shattering process [21, 66]. The pellets interaction with the funnels is extremely brief and in lab tests does not change the pellets so the amount of gas generated from such interaction is likely quite small, but we have no way to measure it. The main source of gas is clearly from the pellet shattering process and has been measured to be a significant fraction of the pellet for fast pellets.

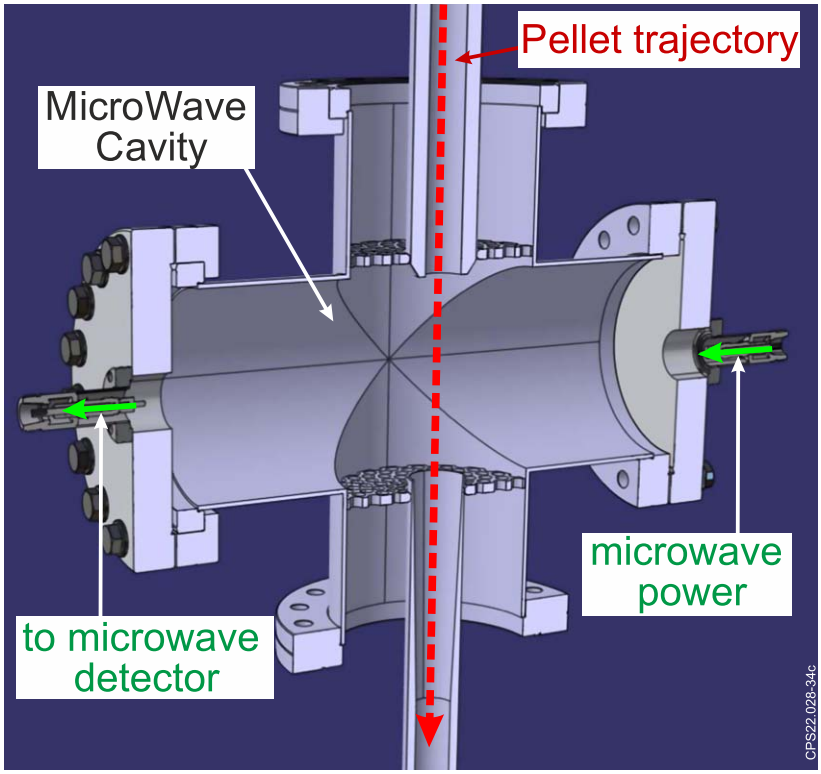

Figure 34. Microwave Cavity (MWC) diagnostic records pellet presence and time. It also allows the integrity of the pellet to be shown.

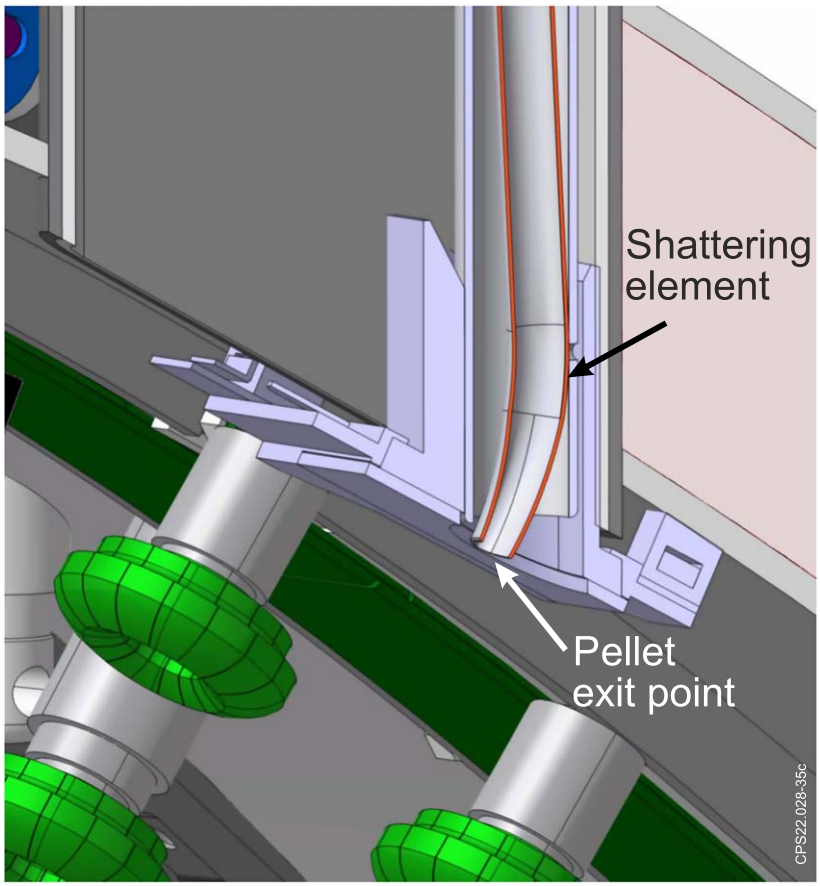

Figure 35. The entry point of the pellet into the JET vacuum vessel. The shatter tube with the shattering element is in red. (The green objects are mushroom limiters).

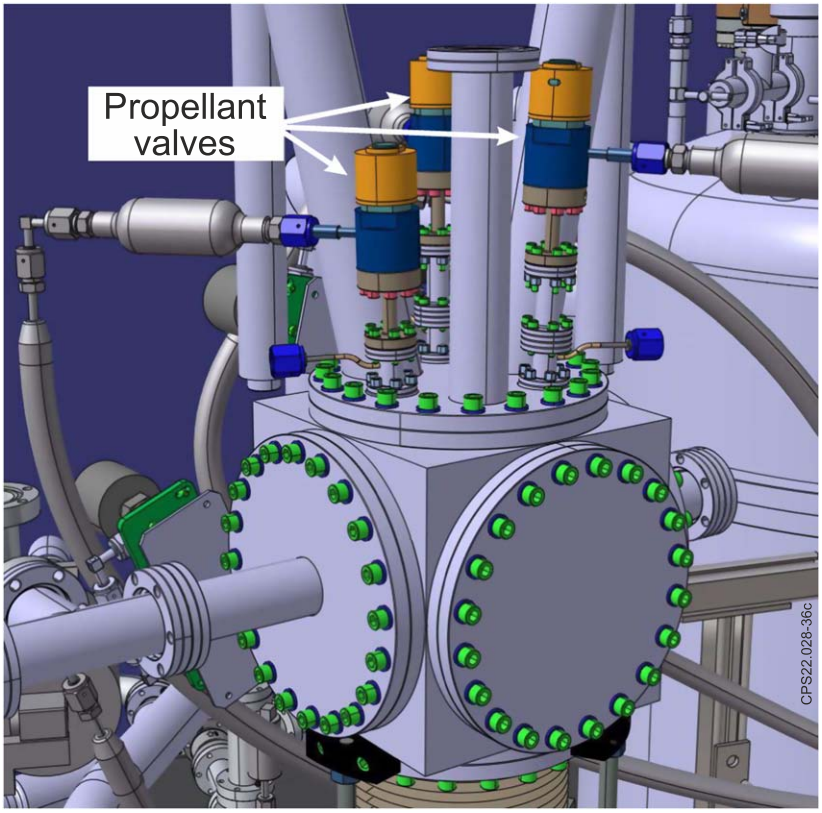

Figure 36. The propellant valves (shown in orange, blue, and brown) are opened to fire the pellets. The solenoid coils are under the orange covered part of the valves.

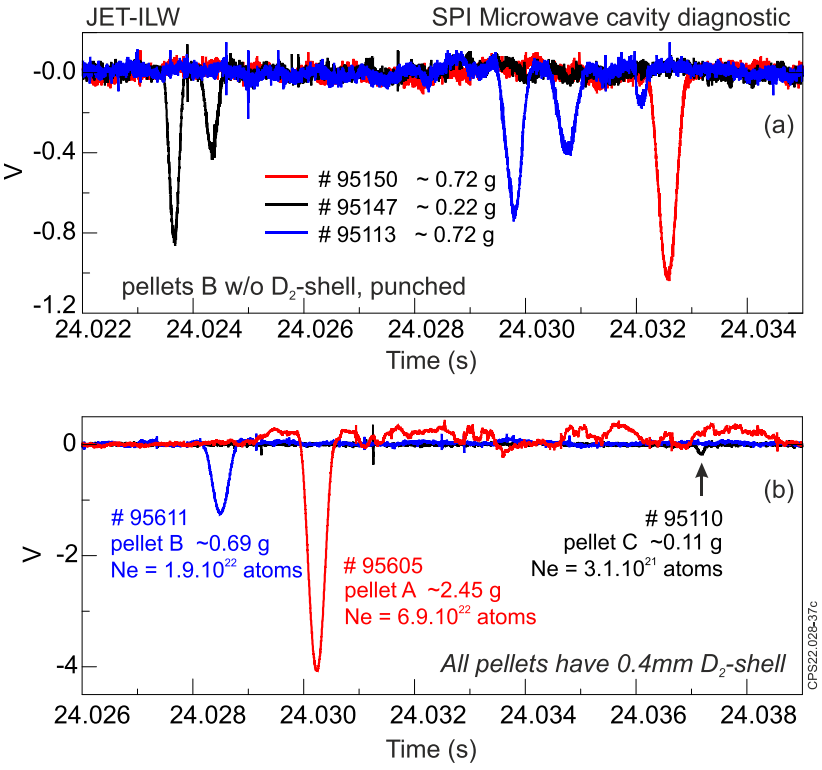

Figure 37. MWC indicates (a) the number of intact/broken pellet pieces, (b) for given substance the MWC amplitude is proportional to pellet mass.

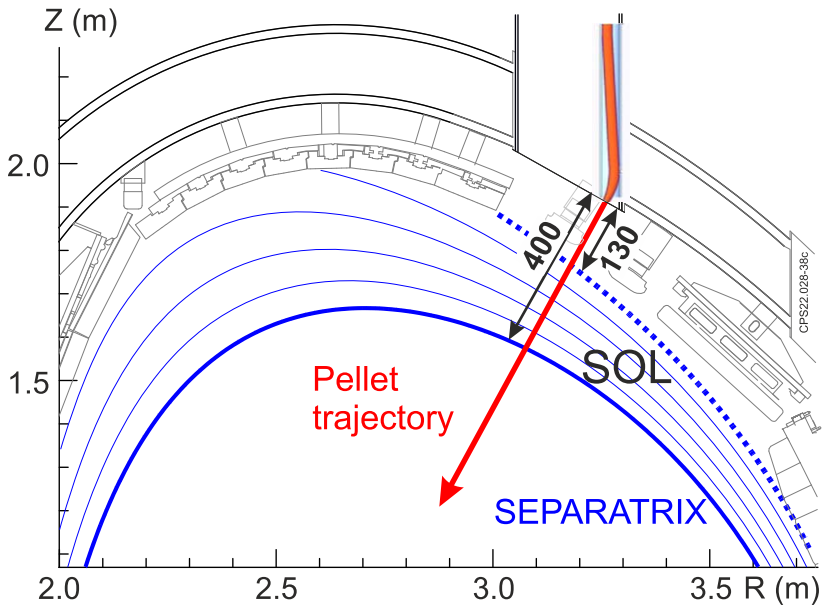

Figure 38. Shattered pellet plume trajectory. To enter the bulk plasma, pellets must fly through the shadow of limiter and the SOL.

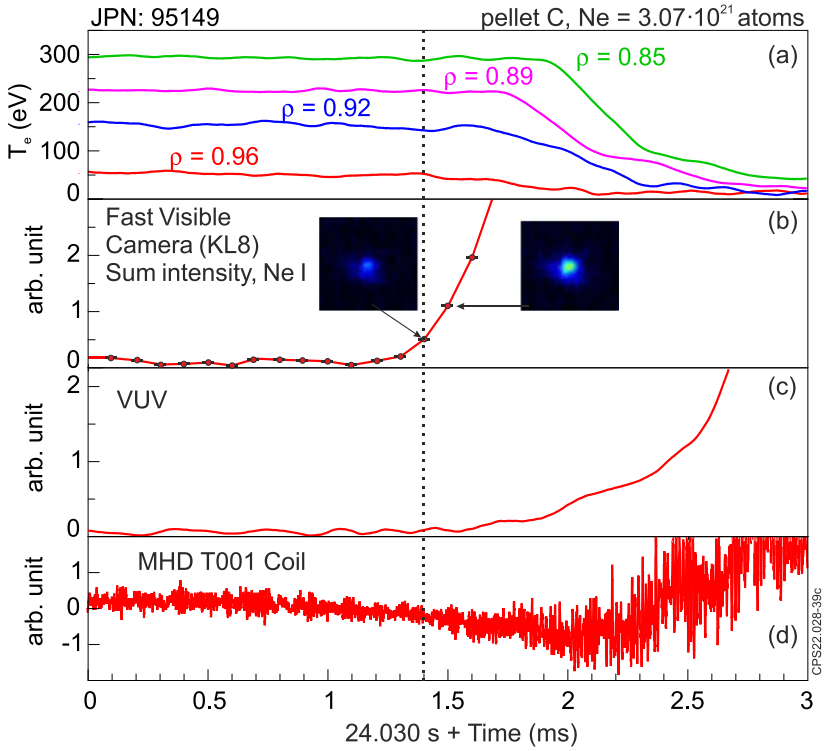

Figure 39. Pellet arrival in plasma detected by various diagnostics: (a) T_e edge channels of ECE, (b) Ne I sum intensity, insets are KL8 camera cut images, (c) VUV light in the mid-plane, (d) Mirnov signal.

Therefore, cooling of the plasma edge may occur when the gas crosses the separatrix, but the shattered pellets are still in the SOL. It is reasonable to assume that the intensity of Ne I line becomes visible when Neon atoms appear in the SOL. However, small size pellet C can fly at ~500 m s^{-1} speed (see this section below), allowing the pellet to cross half of the SOL width (~100 mm) in 200 μs, which is the timing accuracy of the KL8 diagnostics, i.e., the time between two frames. Another possible explanation, is that some of small pellet fragments accelerated by the gas generated by fragmentation process [21]. These fragments can travel ahead of the main cloud of fragments, reach the plasma without producing enough light to be visible above the noise level in the KL8 images. This explanation is supported by the observation in pulse #95150 with medium size pellet B, as

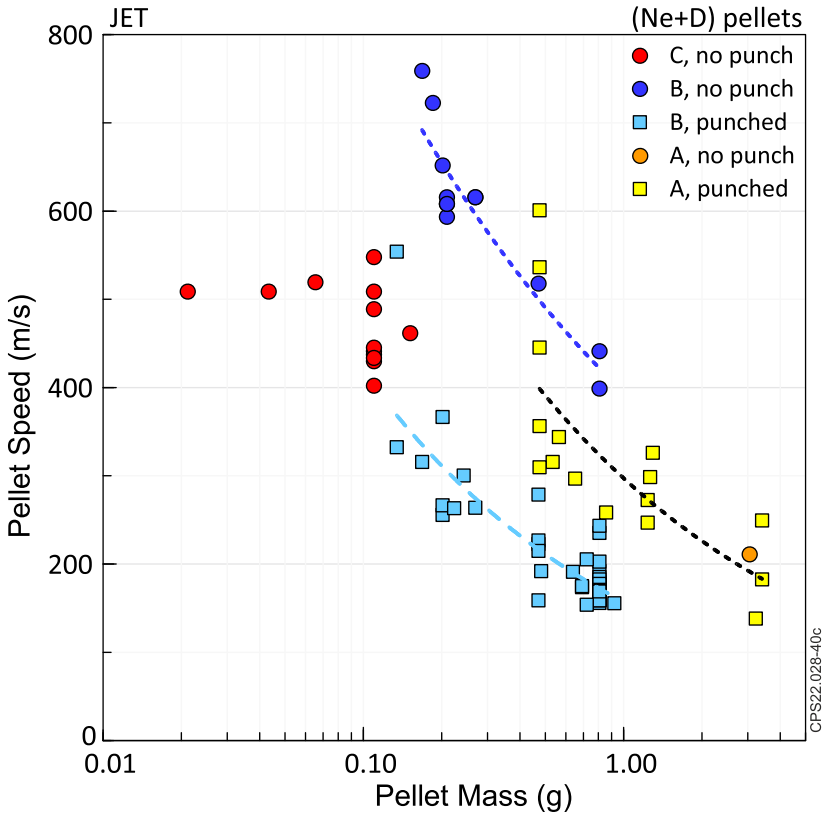

Figure 40. The pellet speed for pellet C (4.5 mm), pellet B (8.1 mm), pellet A (12.5 mm) as a function of pellet mass.

covered in the next section. Moreover, the detection of the pellet arrival requires a visual analysis of the image by a diagnostician, which can introduce additional and, rather, the main error in determining the moment of the arrival of the pellet.

In this paper, the time of flight of the Ne+D_2 pellet is measured by recording the time of passage of the pellet through the MWC and the time the first shards are seen in the plasma by the high-speed KL8 camera equipped with a Ne I filter, figure 6. Further, the distance from the from the centre line of the MWC to the middle of the SOL, namely 4987 mm, was used to calculate the speed of the pellet.

The gas generated during the shattering process affects the speed of fragments, accelerating some and slowing down other fragments. Here, the measured speed refers to the fastest leading cloud of Ne surrounding pellet fragments which, first becomes visible. The calculated speed of the pellet when it enters the plasma exceeds the calculated speed of the unbroken pellet when passing between cold head and the MWC by (30–50)%, where data is taken from figure 6. Moreover, a more significant increase (50%) is observed for the slow pellet. This confirms that the acceleration of the pellet by the gas formed during shattering significantly increases the speed of the leading edge of the Ne cloud.

The dependence of the speed of pellets on the mass of pellets for various compositions and sizes of pellets is shown in figure 40. The speed of a pellet depends on various factors, namely the mass of the pellet, the diameter of the barrel, and whether a mechanical punch is used. In general, low mass pellets should be faster than high mass pellets. Thus, for a given size of pellet (i.e. barrel), large Ne fraction makes the pellets heavier and therefore slower.

However, comparison between barrels can be very misleading. The larger barrel has less restriction for the propellent gas, and the propellant valves gas flows are not the same despite being operated with the same current pulse of 2 ms and initial propellant gas pressure. Thus, a medium size pellet B is faster than a small size pellet C with the same mass, see red and deep blue points in figure 40.

Punches can be mounted on the two largest barrels, A and B. Barrel C cannot be fitted with a punch. The use of the mechanical punch significantly reduces the speed of the pellets compared to pellets propelled directly by gas, but only for the medium size pellet B. However, there is no difference in speed for the large pellet A observed for both punched and non-punched pellets, figure 40.

This is because the punch is driven by the propellant gas and some of the propellant gas energy is lost when the punch is driven, and also due to flow restriction caused by the mechanical punch. For medium pellets B the

speed is reduced by a factor of two compared to the non-punch pellets, see deep blue and light blue points in figure 40.

Appendix C. Features of the use of some diagnostics in the SPI experiment

Microwave cavity diagnostic

The pellet is fired down a flight tube passing through an MWC diagnostic (figures 32(c) and 34), which records its temporary presence and the integrity of the pellet (figures 33(c) and 37) and then the pellet travels further along its flight tube to the vacuum vessel, figures 2 and 35. The MWC diagnostic includes a passive resonant cavity, low power microwave source and a microwave detector, figure 34. The low power uses coaxial microwave cables to connect to a vacuum feedthrough on the actual cavity. The return from the cavity goes to a microwave detector whose signal is amplified and then digitised. The microwave source is a dielectric resonator oscillator that provides some tunability to adjust to the cavity Q resonance. The MWC changes resonance when the pellet dielectric material is in the cavity, typically for less than a millisecond. The resonance change is proportional to the mass of the pellet and that is what the MWC measures.

The amplitude of the MWC signal does not solely depend on the mass of the pellet. The dielectric constants for solid D_2, Ne and Ar are different and that is what changes the Q-factor of the cavity and determines the magnitude of the signal. If the pellets were all D_2 then the magnitude would be proportional to the D_2 mass.

When the pellets pass through the MWC, the number of peaks in the MWC signal reliably indicates the number of intact/broken pellet pieces. Figure 37(a) shows an intact pellet (JPN 95150, red curve) and the broken pellets of two (JPN 95147, black curve) and three (JPN 95113, blue curve) fragments. Due to the noise level on the cavity signal in the current MWC diagnostic setup, a pellet integrity diagnosis was only possible for pellets A and B. Barrel C pellets, which have the smallest diameter, could be observed but broken pellets were either never observed or hidden in the noise, figure 37(b). In principle if the cavity were tuned properly to be in the linear regime of sensitivity (frequency) the sum of the fragment amplitudes would be equal to the single pellet amplitude.

Fast visible and infrared camera diagnostics and analysis

Fast visible cameras. Two fast visible cameras, named KL8-E8WA and KLDT-E5WE provide 2D imaging of fast event dynamics in a large volume of JET plasmas [24–26].

Both cameras have wide-angle tangential views of the JET plasma from just below the horizontal midplane (figure 4). KL8 has a direct view of the SPI, so can provide information about the injection timing and material trajectory, while KLDT-E5WE views the part of the plasma toroidally anti-clockwise from the SPI, as shown in figures 1 and 4. Typical frame rates of (10–20) kHz were used for SPI experiments, with exposure times (frame duration) in the range 1 μs–100 μs to obtain optimal signal levels. KL8 is equipped with remotely interchangeable narrow band filters to image spectral lines of Ne I atoms (692.9 nm), Ar I atoms (706.7 nm) or Ar II $^+$ ions (611.5 nm), while KLDT-E5WE always receives the light over the visible spectrum (430–730) nm.

Fast visible cameras are Photron APX-RS high speed CMOS cameras. For SPI experiments these were typically operated at frame rates of (10–20) kHz. The exposure time (frame duration) can be set independently of the frame rate to optimise the camera signal level, and values between 1 μs–100 μs were used depending on the plasma and pellet configurations and species being observed.

KL8 views the plasma using a lost-light pick-off from an infrared viewing endoscope [67], and due to the use of gold coated mirrors in the endoscope is mainly sensitive to wavelengths $>$ 500 nm. It is equipped with a motorised filter wheel which allows selection of 'un-filtered' imaging or one of 3 narrow band interference filters for specific spectral lines – for SPI experiments particularly Ne I (692.9 nm), Ar I (706.7 nm) or Ar II (611.5 nm). The endoscope is located 28.5 cm below JET's geometrical midplane, 67.5° clockwise toroidally from the SPI (viewed from above) and views anti-clockwise around the torus, figure 1. This gives KL8 a direct view of the SPI injection, viewing the poloidal plane of the injection at an angle ~18° away from purely 'side-on', and therefore providing good localisation of the injected material within the plasma cross-section (figure 4, right). The effective focal length of the optical system is ~4.7 mm, giving an image scale at the SPI injection plane between 18 mm/pixel near the low field side to 26 mm/pixel near the high field side.

KLDT-E5WE views the plasma via another mirror-based endoscope [68], 28.5 cm below the midplane and 168.75° clockwise toroidally from the SPI location, viewing clockwise around the torus, figure 1. Due to being almost toroidally opposite the injector it does not have a direct view of the SPI but can observe the effect on the plasma and transport of material. It integrates over the whole visible spectrum between ~430–730 nm. The design of the in-vessel optics are the same as in [69], with the top and bottom halves of the view formed using two separate entrance pupils and first mirrors. This results in the KLDT-E5WE image having a horizontal split, with some volume of the plasma reproduced twice on the camera sensor close to the image centre, figure 4 left. The

effective focal length of the optical system is ~4.2 mm, giving a spatial scale of ~2.8–3 cm/pixel in the part of the plasma where the transported SPI material is first seen.

To make measurements of injected material position, speeds and size of the shatter plume, features in the images must be mapped to 3D real space in the plasma. To do this the viewing geometry of both cameras was calibrated using the Calcam code [70], which uses well known computer vision models to relate image coordinates to real space vectors. For measuring the shard plumes from KL8, since the camera data are only 2D, an additional assumption is required to constrain the position along camera's viewing direction. In this work we have taken, for each pixel, the position where that pixel's sight-line makes its closest approach to the nominal centre line of the SPI trajectory. This assumption is chosen based on cylindrical symmetry of the injection, and in principle gives a reasonably symmetric error bar on the obtained positions which depends on the width of the shatter plume at that location.

Infrared cameras (analogue). The infrared cameras are named KL12 (views octants 6, 7 and partially 8) and KL14 (views octants 4, 3 and partially 2). The main purpose of the infrared cameras is real-time PFC temperature assessment. The cameras typically operate at 50 Hz rate and 20 ms exposure time.

Frames of visible and infrared cameras can be visualised and analysed with the specific software JUVIL (JET Users Video Imaging Library) created to handle all the cameras of the JET viewing system [27].

Interferometry and polarimetry

The multi-channel Far Infrared (FIR) Interferometer/polarimeter has 4 vertical and 4 lateral channels, 3 of which are shown on figure 3. The system measures line-integrated electron plasma density and Faraday rotation angle/Cotton Mouton angle phase shift for interferometry and polarimetry respectively [30]. The FIR employs two types of Far Infrared lasers: Deuterated Cyanide (DCN) type operating at a wavelength of 194.7 μm and Methanol laser operating at 118.8 μm. The interferometry uses both lasers, either as independent measurements (for vertical channels) or as a two-colour system for lateral channels with the second laser as compensation laser for vibrations. The FIR system provides typical measurements with a 1ms time resolution, but it has the ability to provide very fast measurements for interferometry up to 10 microseconds for the entire JET pulse duration.

Over the years the JET in-vessel machine has evolved, reducing the beam apertures for vertical channels from about 120 mm, required for beams of ~20–35 mm in diameter, to 12–60 mm clearance apertures. Channels 3 and 2 have 60 mm square and 40 mm circular apertures at the beam exits, respectively. However, channel 2 is unreliable for most of the pulses because the laser beams are limited in the divertor by a 12 mm hole and pass through a very perturbative part of plasma at the X-point region.

The key problem of the FIR interferometer is mainly associated with the strong refraction of laser beams at high density gradients, figure 41. The refraction effect varies with the square of the wavelength, hence a Methanol laser with a shorter wavelength was introduced in 2012 with the expectation of being more reliable in high density plasmas.

This is a sufficient improvement for use of the FIR interferometer during most of the events which induce high density gradients (e.g. type I ELMs, impurity seeding experiments, fuelling and pacing pellets) but not for SPI and disruption studies. The JET Interferometry with ~195 μm and ~119 μm beams both suffer from signal loss when the SPI pellet enters the plasma due to the high plasma density and plasma density gradient causing a so-called 'fringe-jump'. This is a measurement error due to the loss of tracking of phase, with interferometry being a history dependent measurement. The polarimetry does not suffer from 'fringe-jumps' and can be operated even with reduced beam amplitude compared to interferometry. The absolute calibration of JET polarimetry is performed using an approximation of a real magnetic field by a vacuum toroidal field. Thus, in order to obtain the correct amplitude of the polarimetry signal, the JET polarimetry must be re-calibrated offline to match the corresponding interferometry signal prior to the disruption event. The time response of polarimetry is about 1 ms due to integration of raw signals.

However, the JET polarimetric signal has a hardware delay, to correct for which the tail of the interferometric signal was matched with the polarimetric signal. Thus, to correct the raw polarimetric signal, a shift of −4.5 ms was applied, figures 42(b), (c).

The density waveform shown in figure 42 is taken from channel 3 (with the line-of-sight seen in figure 3). For the specific pulse #95150, the corresponding polarimetry Faraday Rotation and Cotton-Mouton angles were both about 5 degrees prior to the application of SPI. During the SPI instigated disruption, the Faraday Rotation and Cotton-Mouton angle increase to about 45 and 140 degrees respectively.

Vertical and horizontal bolometry systems

Two bolometry systems, vertical and horizontal, are located in the Octant 3 Main Vertical Port (MVP) and the Octant 6 Main Horizontal Port (MHP), respectively [32]. Each system consists of 24 channels, figures 1 and 5.

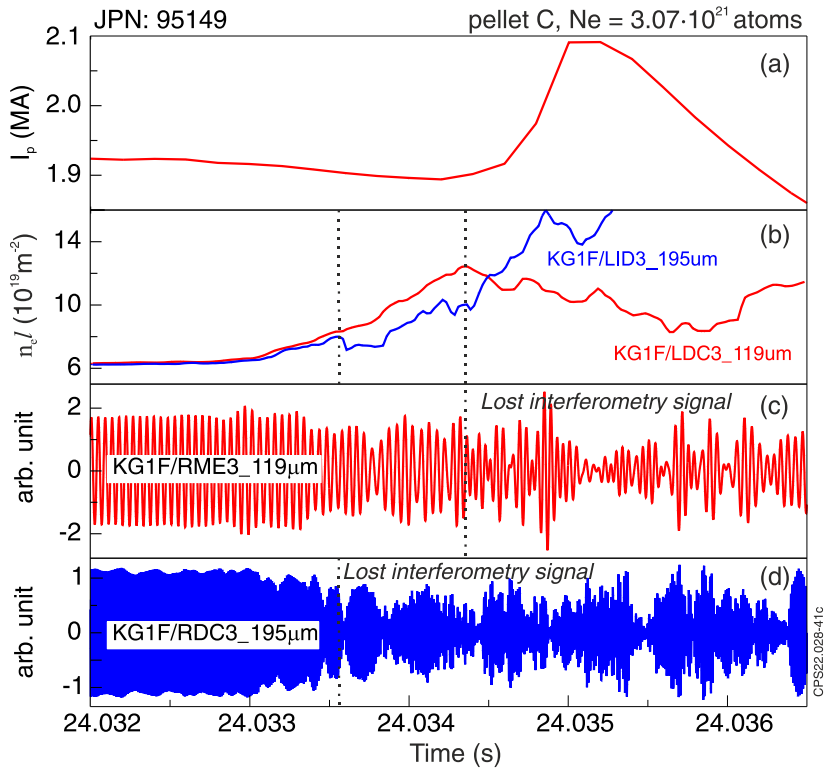

Figure 41. The interferometer suffering from beam bending, which leads to a loss of signal amplitude: (a) plasma current, (b) line density, (c) and (d) beam amplitude.

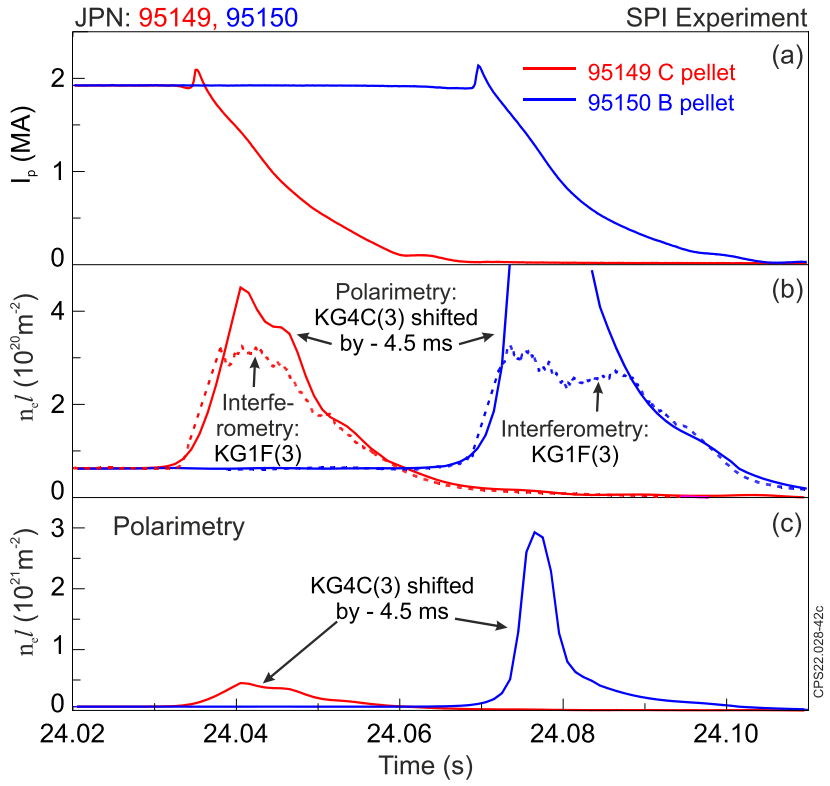

Figure 42. Plasma line averaged electron density measured using polarimetric diagnostics: (a) plasma current, (b) line averaged electron density on an enlarged scale, (c) line averaged electron density.

Table 5. Time delay between soft x-ray and bolometric signals obtained from ELMy JPN 77946.

Cut-off frequency of the Bessel filter (Hz)	Delay (ms)
2000	0.58
1000	0.80
200	2.56
50	8.00

The JET bolometers are gold foil absorbers with an 8 μm-thick gold-absorbing layer on a 20 μm-thick mica substrate and interwoven gold meanders on the rear side each with a typical resistance of 1.2 kOhm [32, 71, 72]. The finite thickness of the foil determines the hardware time resolution which is about ~2 ms. The detector is sensitive to photon energy in the 2.5 eV to 10 keV range, which corresponds to a wavelength of 480 nm to 0.1 nm. The bolometer sensors are in the primary vacuum, so they also measure energy brought by neutral particles. The bolometers are located deep inside the ports (~300 mm for the vertical and 500 mm for the horizontal bolometers), so the bolometer sensors are not affected by charged particles.

The absorbed power onto the foil is monitored by its temperature change and the consequent change in resistance of the gold meander. To compensate for both temperature drifts and electromagnetic disturbances, and background pressure changes, a second reference bolometer is employed which is optically shielded from the plasma. The "background pressure" is the neutral gas pressure in the vessel. Just having some gas in contact with the bolometer sensors will change its temperature, cooling, or heating it.

The two reference meanders and two measurement meanders are coupled in a Wheatstone bridge circuit such that the output voltage is proportional to any instantaneous temperature deviation of the measuring absorber. Four such units are combined to form a bolometer head. The active area of the absorber foil is 3.8 mm $\times$ 1.3 mm with a 5 mm spacing between detectors. A thin heat-conducting layer of gold 0.2 μm thick provides contact between the absorbing foil and the body of the bolometer head.

The vertical camera at JET is comprised of 8 bolometer heads (2 of them being spare) and the horizontal camera is comprised of 6 bolometer heads, thus providing a total of 24 vertical and 24 horizontal usable channels. They form two fan fields of view across the plasma, figure 5.

To measure the change in resistance of the bolometer a sinusoidal voltage of 40 V (peak-to-peak), 50 kHz is applied independently to each bolometer sensor, and the response is measured by a homodyne detector.

The signal passes through an amplifier with a selectable gain ranging from 20 to 5000, followed by a 4th order active analogue low-pass Bessel filter with a choice of different cut-off frequencies. Then the signals are digitised with a 5 kHz sampling rate.

For disruption experiments the filter cut-off frequency is set to 1 kHz (this information is written in the JET Pulse File, JPF, with the JPF name DB/B5HFLTR:0NN, where NN is the channel number).

Based on SPICE (Simulation Program with Integrated Circuit Emphasis) simulation, the 1 kHz filter introduces a 0.51 ms group delay, constant up to 2 kHz. The simulated delay is in good agreement with laboratory measurements. The attenuation at a frequency of 2 kHz due to the filter leads to a decrease in the voltage amplitude by about 80%.

There is an additional signal delay due to the finite thickness of the foil (heat transfer effect) of about 0.338 ms. Finally, the delay of the bolometric signals was estimated by comparing it with soft x-rays, which have a faster response, for the ELMs in JPN 77946, table 5.

However, the transfer function of the bolometers is not just a time shift. For faster events, comparable to the filter cut-off frequency, different harmonics will be affected differently.

The signal is then processed in order to calculate the incident power, P(t), on the bolometer according to the bolometer equation [73]

$$P(t) = \frac{\tau_C}{S_{bolo}}\left(\frac{d\Delta U(t)}{dt} + \frac{\Delta U(t)}{\tau_C}\right) \tag{C1}$$

where U(t) is the output voltage, S_{bolo} (V/W) the sensitivity and τ_c (s) is the cooling time constant of the foil. The quantities S_{bolo} and τ_C are determined by the calibration of the instrument, where $\tau_c \approx 0.2$ s and $S_{bolo} \approx 6$ V W^{-1}.

The total plasma radiation power is calculated from the weighted sum of vertical channels 1–8 and 17–24, which are shown with solid lines on figure 5, using the method described in [74]. It is written in the PPF with name BOLO/TOPI. The vertical channels are chosen because they have more complete plasma coverage, including the divertor, but it is unlikely that the radiation from the divertor will make a difference during SPI. The weights for the sum are determined by the difference between the bolometer lines of sight to parallel ones in a projection space.

There are two standard bulk (non-divertor) radiated power estimates. One estimate uses channels 1 to 5 from the vertical camera, assumes poloidal symmetry and uses an interpolated virtual channel for the centre. Because of this choice, any outboard side impurity accumulation (common in high performance experiments) leads to an overestimate of the bulk radiated power. This data is written in the PPF with name BOLO/TOPU. The other estimate uses channels 15 to 24 from the horizontal camera and assumes poloidal symmetry, ignoring the divertor facing channels and is written in the PPF with name BOLO/TOPH. All these estimates, TOPI, TOPU and TOPH, assume toroidal symmetry and therefore overestimate or underestimate the radiation of toroidally asymmetric plasma, as in the SPI experiment. Moreover, the usage of local gas supply into the plasma within the field of vision of the horizontal camera results in an overestimating the bulk power.

It should be emphasized that further PPF processing of the signal after registration (in addition to the sensor response time and the low-pass filter) change the signal shape for the fast events, as ELM and disruptions. PPF processing used smoothing procedure that is why a simple time shift, as in table 5, will give a bolometric signal rising before the fast event.

Tomographic reconstruction makes it possible to visualize plasma radiation [75]. JUVIL software provides tomographic reconstruction images every 10 ms with an averaging window of ±5 ms. However, tomography assumes a toroidal symmetry of the radiation, since it uses vertical and horizontal bolometry systems located in two different JET octants. In [36], two methods for estimating the radiated power in SPI instigated disruptions in JET are described.

Electron cyclotron emission

The radiation temperature is measured by an ECE heterodyne radiometer at the frequency of the 2nd electron cyclotron harmonic of X-mode. The X-mode and O-mode are both electromagnetic perpendicular propagating waves with electric field mostly perpendicular to total magnetic field $\vec{B}$. They have different (almost circular if away from hybrid resonances) polarisations: X-mode rotates in electron gyration direction and O-mode rotates in ion gyration direction.

The ECE radiation is collected from the tokamak low field side, almost perpendicular to the total magnetic field along the major radius [33]. The antenna is located at the MHP of Octant 7 at a height of 0.133 m above the vessel mid-plane, figures 1 and 3. The number of channels is 96, with a frequency separation corresponding to 1 cm for JET magnetic field gradient, see example in figure 8.

The output of the detector is amplified by a low noise video amplifier with a 1 MHz bandwidth and sent to the standard (2.5 kHz) and fast (200 kHz) acquisition systems. The fast ECE signals should be used to study high-speed event such as SPI instigated disruptions. However, the raw fast ECE signals are still noisy, which requires additional signal smoothing, figure 43. The +/− 100 μs triangular smoothing gives good noise removing while still providing decent representation of the temporal temperature behaviour caused by the injected pellet.

ECE temperature measurements can be influenced by various reasons, however increasing the electron concentration to the cut-off level is the principal measurement problem one would expect in SPI experiments.

The solution of the dispersion equation for ECE X-mode radiation, which provides an expression for cut-off frequency, see equation (11.40) in [76], is:

$$\omega_R = \frac{1}{2}[\omega_{ce} + \sqrt{\omega_{ce}^2 + 4\omega_{pe}^2}], \tag{C2}$$

where

$\omega_{pe} = \sqrt{\frac{e^2 n_e}{\varepsilon_o m_e}}$ is the electron plasma frequency, and $\omega_{ce} = \frac{eB}{m_e}$ is the electron cyclotron frequency; e is the electron charge, m_e is the electron mass, ε_o is the vacuum electric permittivity, and n_e is the electron density. The left-hand side of (3) is the frequency of the source, that is the 2nd electron cyclotron harmonic at the emission point R, namely $\omega_R = 2\omega_{ce}(R)$ [77, 78]. The right-hand side of (3) should be calculated at the point where n_e reaches the cut-off value, R_{dh}. Then by rearrangement (3), we get a formula for local cut-off of the density as a function of R and R_{dh} (where $R_{dh} \geqslant R$) [79]:

$$n_{cut-off} = 4\frac{\varepsilon_o}{m_e}\left(\frac{B_o R_o}{R}\right)^2\left[1 - \frac{1}{2}\frac{R}{R_{dh}}\right], \tag{C3}$$

where

JET major radius $R_o = 2.98$ m. For the case when local electron density at the emission point reaches the cut-off level, $R_{dh} = R$, then the radiation cannot leave the source and we get well-known expression:

$$n_{cut-off} = 2\frac{\varepsilon_o}{m_e}\left(\frac{B_o R_o}{R}\right)^2. \tag{C4}$$

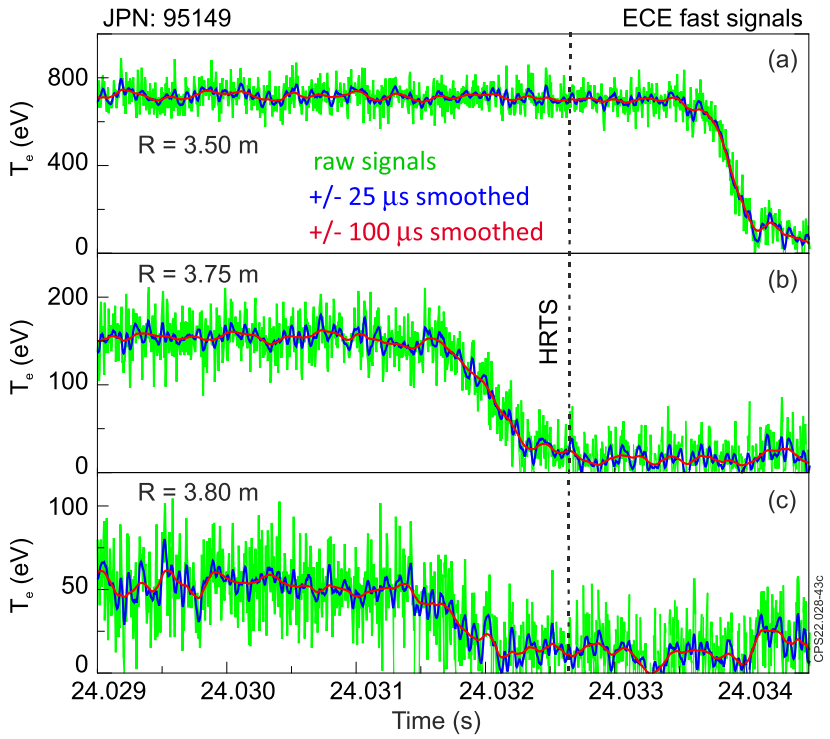

Figure 43. ECE fast signals (raw and triangular smoothed) during the cooling just before disruption: (a) R = 3.50 m, (b) R = 3.75 m, (c) R = 3.80 m; see ECE and HRTS profiles in figure 8.

On JET, the condition (5) is achieved for a high-density plasma close to the Greenwald limit [80]. An example of an ECE cut-off for a high-density plasma shown in figure 44. The plasma density is higher than cut-off value for the R = [3.3–3.75] m, where the channels affected by the ECE cut-off are shown with red triangles. The ECE 'temperature' differs from the actual T_e measured by HRTS.

The figure 45 illustrates the (4) and (5) formulas, where (5) is shown with a blue curve and (4) is shown with a red curve for given $R = R_{ece}$. The 2nd ECE harmonic cut-off region is marked with a greenish tint. The real n_e profile is measured by HRTS diagnostic for Ohmic plasma as an example shown on the figure 45. Thus if n_e increased dramatically up to (7–8)$\bullet 10^{19}$ m^{-3} then radiation is reflecting at high density region, and it is unable to propagate to the detecting system.

The question of the start and end points of the TQ and, accordingly, the duration of the TQ is currently of great interest to the scientific community. Here we used a mathematically rigorous procedure for calculating the time parameters of the TQ, using the same procedure used to calculate the duration of the CQ. First, the $sum(T_e)$ of all ECE T_e channels in the plasma is calculated. This can be the sum of all ECE channels or the sum of the ECE channels of the central region. However, during SPI-induced disruptions, the outer region of the plasma is cooled to TQ, so here we used the sum over the ECE channels of the central region for $\rho \leqslant 0.3$.

Then the fall in $sum(T_e)$, approximated by linear extrapolation between 80 % and 20% of pre-TQ $sum(T_e)$. The duration of the TQ phase defined as the time interval between 80 % and 20% of pre-TQ $sum(T_e)$ multiplied by $\frac{5}{3}$. In addition, the start and end points of the TQ can be defined as intersection of two corresponding lines.

High resolution thomson scattering

HRTS provides 63 spatial data points per profile, with a 20 Hz repetition rate for the duration of a JET pulse [34, 35]. The HRTS data typically runs from R = 3.0 to 3.9 m, figure 3. The system has a spatial resolution of ~1.6 cm in the core region and ~0.8 cm in the pedestal region, figure 46(a).

Two sorts of polychromators, 4 spectral channels in each, are used for Core (b) and Edge (c) measurements figure 46. Each 4-channel spectrometer by using two delayed optical paths allows three spatial point data to be addressed by one spectrometer. The core uses dual fibers to increase photon statistics by compromising spatial resolution; high plasma density also increases the raw signal.

The T_e and n_e for each spatial point are determined by a signal distribution in the corresponding spectral channels. Spectral distribution is obtained by a Gaussian fit to the raw data of the scattered laser light, for each spectral channel and each spatial point (figures 46(b), (c)). However, raw data usually contains noise due to limited photon statistics. The diagnostic requires good signal on a minimum of two channels to determine T_e

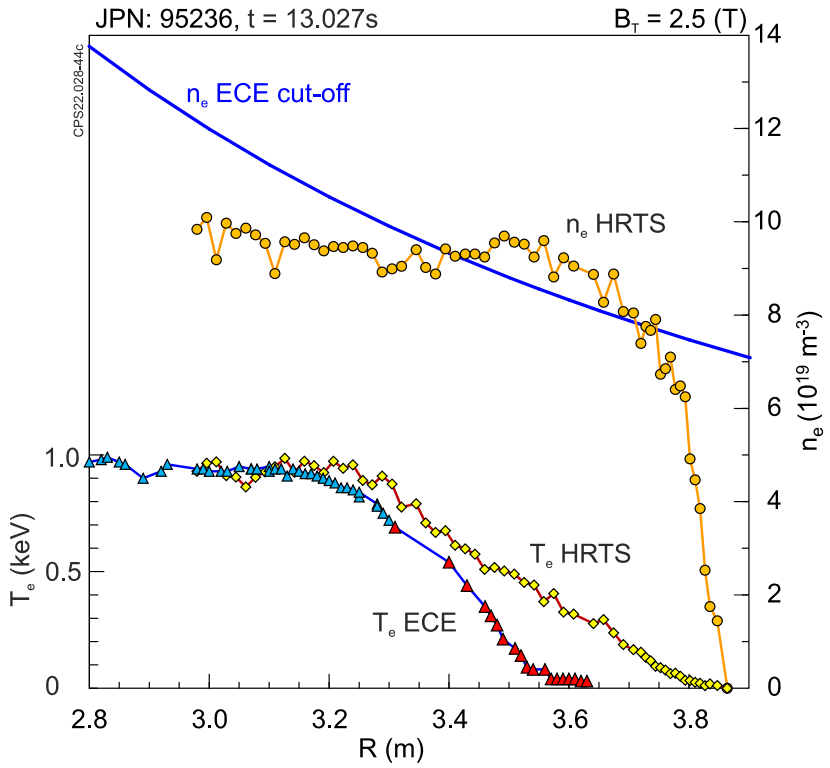

Figure 44. An example of an ECE cut-off for a high-density plasma, the affected channels are shown with red triangles.

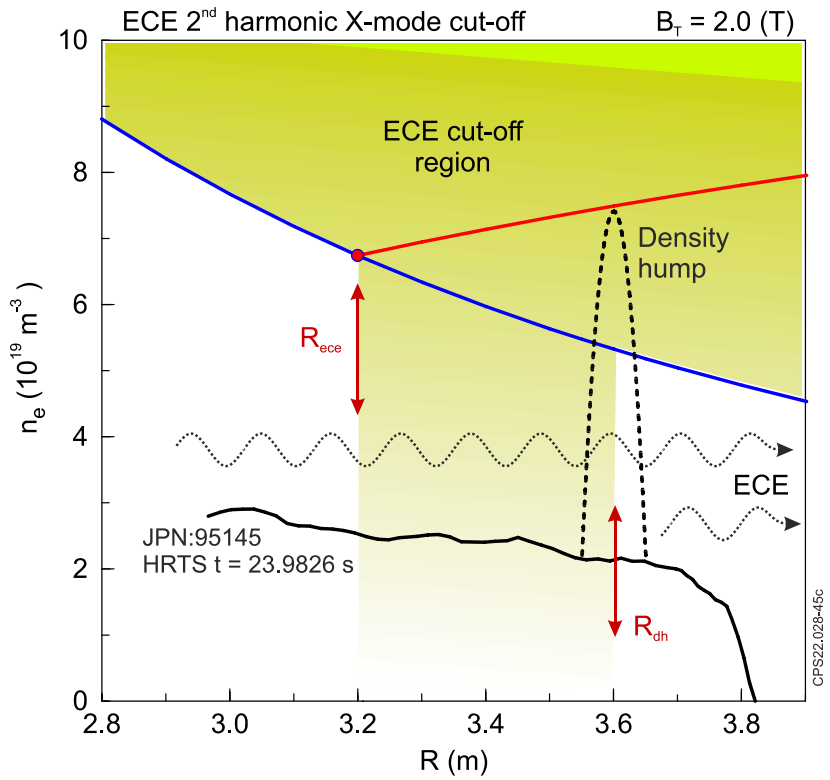

Figure 45. Illustration of the 2nd ECE harmonic cut-off: the blue curve is the local density threshold; the red curve represents the density at point R_{dh}, which cuts off the radiation coming from point R_{ece} in the $R_{ece} < R < R_{dh}$ region; the HRTS density profile in JPN 95145, t = 23.9826 s.

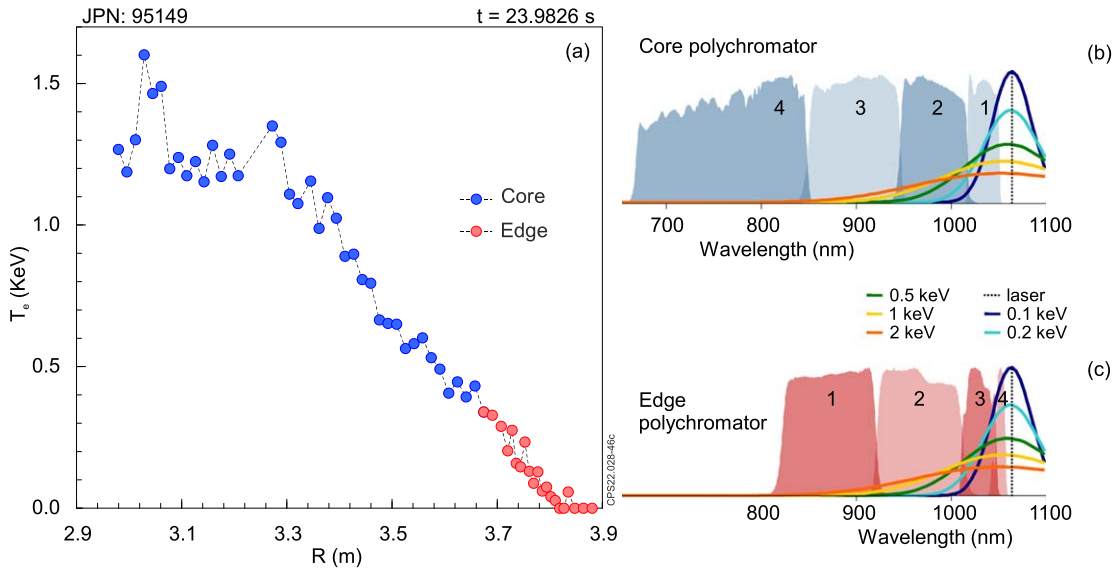

Figure 46. (a) HRTS gives 63 spatial data points. Two types of polychromators, 4 spectral channels in each, are used for Core (b) and Edge (c) measurements.

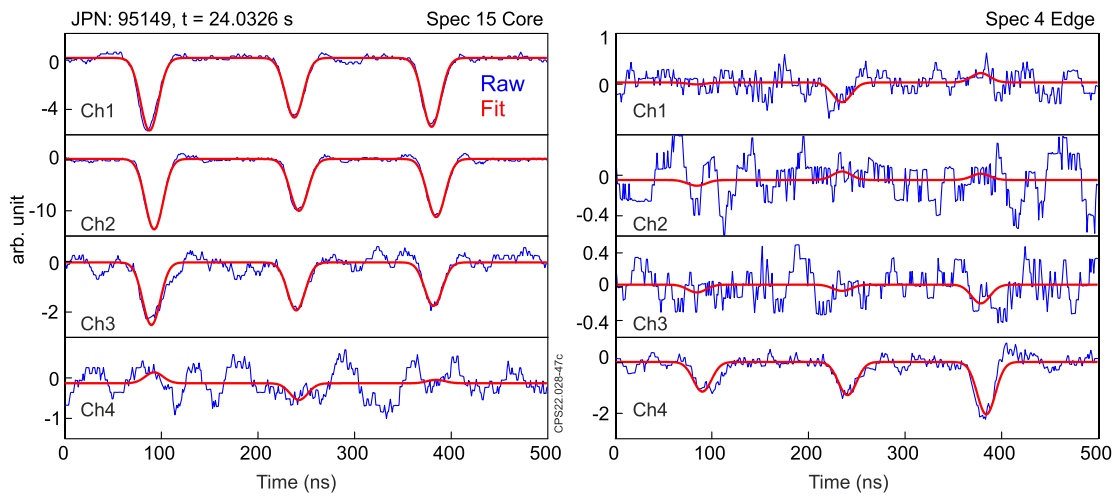

Figure 47. HRTS raw data for one core and one edge spectrometer with 3 signals combined via delay lines: noisy lines (in blue) are recorded raw signals. Gaussian fits of scattered laser light (in red) are used to determine signal levels per spectral channel. Left: Core spatial points, good signal on three spectral channels. Right: Edge spatial points, good signal only on one spectral channel 4.

and n_e (figure 47), therefore, until the 2022, reliable HRTS T_e and n_e were only available for Te $\geqslant$ (50–100) eV. In 2022, the JET HRTS has been upgraded to allow low T_e (down to 1 eV) measurements during CQ.

Soft x-ray. It should be noted that the lower T_e threshold for the JET soft x-ray diagnostic (since 2017, JPN 92505, all Be windows are 250 μm thick) is about 2–3 keV. In particular, the x-ray signal is reduced by a factor of 2 at 3 keV and by a factor of 20 at 2 keV compared to 10 keV plasma, so the soft x-ray diagnostic cannot be used to characterise TQ when $T_e < 2.5$ keV.

Appendix D. 0D simulation of the interaction of the mixture (Ne + D) with plasma

A 0D model was used to elucidate the main critical parameters of a pellet injection affecting radiation loss. The model explicitly does not use Coronal Equilibrium (CE) because it includes rate equations for ionisation/recombination dynamics and does not assume that ionisation states are in equilibrium. The model calculates the

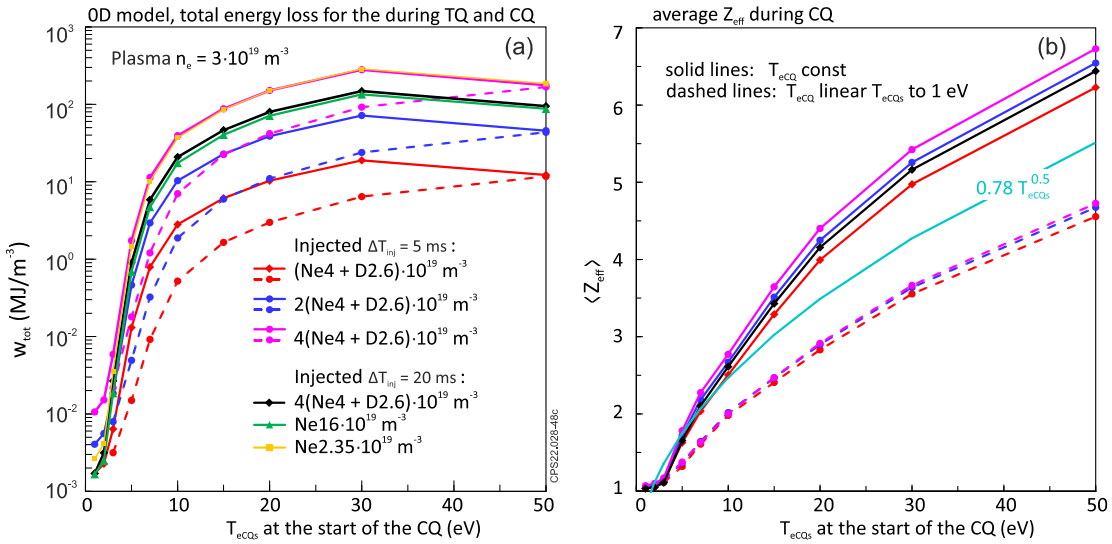

Figure 48. 0D model, dependences on the plasma temperature at the start of CQ (a) of total energy loss for entire TQ and CQ: (b) average Z_{eff} during CQ only. $\langle Z_{eff} \rangle$ increases approximately proportionally to square root of T_{eCQs} during the CQ. Solid lines: T_{eCQ} is constant, dashed lines: T_{eCQ} decreasing linearly from T_{eCQs} to 1 eV. Background plasma with $n_e = 3{\cdot}10^{19}$ m^{-3}.

dynamics of plasma electron energy losses induced by radiating impurities in deuterium plasma. All spatial concentrations in the model are assumed to be uniform. The model solves coupled rate equations for ionization dynamics of all charge states of injected impurities, as well as of both background and injected deuterium. The background D is assumed to be fully ionized initially, while the additional D and impurities are injected as neutral atoms. The model calculates impurity radiation loss (E_{rad}) and total energy loss (E_{tot}) of electrons, which, in addition to radiation, includes binding energy contribution due to ionization. Tabulated rate coefficients as functions of electron temperature and density are provided by ADPAK [81, 82].

The temporal variation of the electron temperature in the model is prescribed, while the electron density is calculated according to the plasma quasi-neutrality condition

$$n_e(t) = Z_{Ne}^{avr}(t){\cdot}n_{Ne}(t) + Z_D^{avr}(t){\cdot}n_D(t), \qquad \text{(D1)}$$

where $Z_{Ne}^{avr}(t)$ is current Ne average charge value, $n_{Ne}(t)$ is current Ne density, $Z_D^{avr}(t)$ is current D average charge value, $n_D(t)$ is current D density.

Time-solved ionization rate equations take into account electron impact ionization, recombination for all charge states of Ne and D, and Charge eXchange (CX) between Ne^{Z+} and D, and also between D and D^+. Available ADPAK files have no data on Ne - Ne^{Z+} CX and it is not included in the calculations.

The rate equations are solved using an explicit first order numerical scheme with time step 1 ns. The radiation and total electron energy losses by Ne and D particles are calculated on each time step and then integrated in time. As a result, the model provides temporal evolution and time-integrated electron energy losses due to Ne and D radiation and ionization.

In these calculations, the electron temperature T_e is set equal to 1300 eV initially, which corresponds to T_e in the centre of the plasma before cooling/TQ for #95150 and #95149 (figure 9). The evolution of T_e over time was not measured during TQ for medium pellet B (#95150) and CQ in all cases. So, T_e in the model is chosen manually, beginning with a phase of exponential decay to a given value T_{eCQs} at the end of the TQ, of duration 0.5 ms, followed by a CQ phase of 24.0 ms duration. The calculations are carried out with two different CQ phases: a constant T_{eCQ} and a linear decrease from T_{eCQs} to 1 eV.

Calculations are conducted at a given background plasma density $n_e = 3{\cdot}10^{19}$ m^{-3}. We assumed that neutral Ne and D with a given ratio of the number of atoms Ne/(Ne+D) = 0.60 are injected at $t = 0$ s during ΔT_{inj} at a fixed rate.

The calculations are also conducted with various values of the parameters T_{eCQ} (plasma electron temperature at the beginning of CQ, i.e. right after TQ and with no MHD phase considered) and n_{Ne0}, n_{D0} (amount of injected Ne and D), to study the sensitivity of the model to the experimentally controlled (amount of injected Ne and D) and unmeasured parameters (T_e during CQ).

Impurities injected into the plasma in the form of neutral atoms create a powerful energy loss channel due to the radiation, W_{rad}, and binding (ionisation), W_{bin}, energy loss, with $W_{tot} = W_{rad} + W_{bin}$. Additionally, the

charge exchange process may contribute to the distribution of impurity ionization states and so can potentially affect both radiation and binding (ionisation) losses.

The simulation results show that radiation and total electron energy losses on D particles are negligible in comparison to those on Ne for T_{eCQ} ~3 eV and above, while both D and Ne losses are small at lower T_{eCQ}. Also, it is found that charge exchange between Ne and D has very small impact on Ne ionization dynamics and therefore on Ne radiation losses. The impact of injected D on the radiation losses, thus, is mainly due to increase of the electron density due to D ionization.

According to the model, the main losses occur during CQ when T_e is relatively small, so radiation losses at TQ are relatively insignificant.

The calculated total losses per unit volume are shown in figure 48(a). There is a very strong dependence of energy loss on the T_{eCQ} at the start of CQ, especially in the for $T_{eCQ} <$ (10–15) eV. The details of time dependency of the T_e during the CQ are also critical. Doubling the amount of injected particles also greatly increases (about 3–5 times) the energy loss in the 0D model.

Most of the calculations were carried out for an impurity injection duration of $\Delta T_{inj} = 5$ ms, which roughly 'corresponds' to pellet C injection, figure 14 left frame. The 0D model shows a slight reduction in total energy loss for $\Delta T_{inj} = 20$ ms compared to $\Delta T_{inj} = 5$ ms, see solid black and magenta lines in figure 48(a). The data with $\Delta T_{inj} = 20$ ms roughly 'corresponds' to pellet B injection, where pellet B is visible during the entire CQ, figure 14 right frame.

Another interesting result of the model is that the $\langle Z_{eff} \rangle$, mean value of Z_{eff} during the CQ, increases roughly in proportion to the square root of T_{eCQ}, however, the proportionality coefficient depends on the details of time dependency of the T_e during the CQ, figure 48(b).

ORCID iDs

S N Gerasimov https://orcid.org/0009-0002-3793-7211
A Boboc https://orcid.org/0000-0001-8841-3309
I S Carvalho https://orcid.org/0000-0002-2458-8377
A Huber https://orcid.org/0000-0002-3558-8129
V Huber https://orcid.org/0000-0002-5213-1841
S Jachmich https://orcid.org/0000-0001-8289-536X
S I Krasheninnikov https://orcid.org/0000-0002-0786-5440
M Lehnen https://orcid.org/0000-0001-6043-8803
M Maslov https://orcid.org/0000-0001-8392-4644
G Sergienko https://orcid.org/0000-0002-1539-4909
S Silburn https://orcid.org/0000-0002-3111-5113
C Stuart https://orcid.org/0000-0002-6790-1706
H Sun https://orcid.org/0000-0003-0880-0013
L E Zakharov https://orcid.org/0000-0002-2355-9144

References

[1] Mirnov S V 2016 V. D. Shafranov and Tokamaks *J. Plasma Phys.* **82** 1–20
[2] Gerasimov S N *et al* 2020 Overview of disruptions with JET-ILW *Nucl. Fusion* **60** 066028
[3] Lehnen M *et al* 2011 Disruption mitigation by massive gas injection in JET *Nucl. Fusion* **51** 123010
[4] Gerasimov S N *et al* 2015 JET and COMPASS asymmetrical disruptions *Nucl. Fusion* **55** 113006
[5] Lehnen M *et al* 2013 Impact and mitigation of disruptions with the ITER-like wall in JET *Nucl. Fusion* **53** 93007–13
[6] Lehnen M, Jachmich S and Kruezi U 2020 The ITER disruption mitigation strategy *Tech. Meet. Plasma Disruptions their Mitig.* (https://conferences.iaea.org/event/217/contributions/17867/attachments/9322/12801/Lehnen_IAEA_TM2020_final.pdf)
[7] Luce T C *et al* 2021 Progress on the ITER DMS design and integration *Proc 28th IAEA Fusion Energy Conf. (FEC 2020)* Contrib. ID 1413 (https://nucleus.iaea.org/sites/fusionportal/Shared%20Documents/FEC%202020/fec2020-preprints/preprint1344.pdf)
[8] Lehnen M *et al* 2015 Disruptions in ITER and strategies for their control and mitigation *J. Nucl. Mater.* **463** 39–48
[9] Commaux N *et al* 2016 First demonstration of rapid shutdown using neon shattered pellet injection for thermal quench mitigation on DIII-D *Nucl. Fusion* **56** 046007
[10] Sweeney RDiii-D Team *et al* 2021 3D radiation, density, and MHD structures following neon shattered pellet injection into stable DIII-D Super H-mode discharges *Nucl. Fusion* **61** 066040
[11] Baylor L R, Meitner S J, Gebhart T E, Caughman J B O, Herfindal J L, Shiraki D and Youchison D L 2019 Shattered pellet injection technology design and characterization for disruption mitigation experiments *Nucl. Fusion* **59** 066008
[12] Gerasimov S N *et al* 2020 Mitigation of disruption electro-magnetic load with SPI on JET-ILW *Tech. Meet. Plasma Disruptions their Mitig.* (ITER Headquarters) (https://conferences.iaea.org/event/217/contributions/17860/attachments/9366/12945/Gerasimov_2020-07-20_ITER_SPI_v3.pdf)
[13] Gerasimov S N *et al* 2021 Mitigation of disruption electro-magnetic load with SPI on JET-ILW *47th EPS Conf. Plasma Physics, EPS 2021* P1.1031, 205–8

[14] Jachmich S et al 2021 Shattered pellet injection experiments at JET in support of the ITER disruption mitigation system design Proc 28th IAEA Fusion Energy Conf. (FEC 2020) 10–5 EX/5-1Ra
[15] Jachmich S et al 2022 Shattered pellet injection experiments at JET in support of the ITER disruption mitigation system design Nucl. Fusion 62 026012
[16] Baylor L R et al 2021 Design and performance of shattered pellet injection systems for JET and KSTAR disruption mitigation research in support of ITER Nucl. Fusion 61 106001
[17] Sheikh U A, Shiraki D, Sweeney R, Carvalho P, Jachmich S, Joffrin E, Lehnen M, Lovell J, Nardon E, Silburn S and JET Contributors 2021 Disruption thermal load mitigation with shattered pellet injection on the Joint European Torus (JET) Nucl. Fusion 61 126043
[18] Reux C et al 2022 Physics of runaway electrons with pellet injection at JET Plasma Phys. Control. Fusion 64 034002
[19] Gerasimov S N, Hender T C, Morris J, Riccardo V and Zakharov L E 2014 Plasma current asymmetries during disruptions in JET Nucl. Fusion 54 073009
[20] Jachmich S et al 2016 Disruption mitigation at JET using massive gas injection 43rd Eur. Phys. Soc. Conf. Plasma Physics, EPS 2016 8–11
[21] Gebhart T E, Baylor L R and Meitner S J 2021 Analysis of the shattered pellet injection fragment plumes generated by machine specific shatter tube designs Fusion Sci. Technol. 77 33–41
[22] Meitner S, Baylor L R, Commaux N, Shiraki D, Combs S, Bjorholm T, Ha T and McGinnis W 2017 Design and commissioning of a three-barrel shattered pellet injector for DIII-D disruption mitigation studies Fusion Sci. Technol. 72 318–23
[23] Gouge M J, Combs S K and Milora S L 1990 A combined microwave cavity and photographic diagnostic for high-speed projectiles Rev. Sci. Instrum. 61 2102–5
[24] Alonso J A et al 2008 Fast visible camera installation and operation in JET AIP Conf. Proc. 988 185–8
[25] Losada U, Manzanares A, Balboa I, Silburn S, Karhunen J, Carvalho P J, Huber A, Huber V, Solano E R and de la Cal E 2020 Observations with fast visible cameras in high power Deuterium plasma experiments in the JET ITER-like wall tokamak Nucl. Mater. Energy 25 100837
[26] De La Cal E et al 2020 Impact of divertor configuration on recycling neutral fluxes for ITER-like wall in JET H-mode plasmas Plasma Phys. Control. Fusion 62 035006
[27] Huber V et al 2017 JUVIL: a new innovative software framework for data analysis of JET imaging systems intended for the study of plasma physics and machine operational safety Fusion Eng. Des. 123 979–85
[28] Angelone M, Pillon M, Marinelli M, Milani E, Prestopino G, Verona C, Verona-Rinati G, Coffey I, Murari A and Tartoni N 2010 Single crystal artificial diamond detectors for VUV and soft x-rays measurements on JET thermonuclear fusion plasma Nucl. Instruments Methods Phys. Res. Sect. A Accel. Spectrometers, Detect. Assoc. Equip. 623 726–30
[29] Boboc A, Gil C, Pastor P, Spuig P, Edlington T and Dorling S 2012 Upgrade of the JET far infrared interferometer diagnostic Rev. Sci. Instrum. 83 10E341
[30] Boboc A, Bieg B, Felton R, Dalley S and Kravtsov Y 2015 Invited article: a novel calibration method for the JET real-time far infrared polarimeter and integration of polarimetry-based line-integrated density measurements for machine protection of a fusion plant Rev. Sci. Instrum. 86 091301
[31] Boboc A, Gelfusa M, Murari A and Gaudio P 2010 Recent developments of the JET far-infrared interferometer-polarimeter diagnostic Rev. Sci. Instrum. 81 1–4
[32] Huber A et al 2007 Improved radiation measurements on JET - First results from an upgraded bolometer system J. Nucl. Mater. 363–365 365–70
[33] De La Luna E, Sánchez J, Tribaldos V, Conway G, Suttrop W, Fessey J, Prentice R, Gowers C and Chareau J M 2004 Electron cyclotron emission radiometer upgrade on the Joint European Torus (JET) tokamak Rev. Sci. Instrum. 75 3831–3
[34] Pasqualotto R, Nielsen P, Gowers C, Beurskens M, Kempenaars M, Carlstrom T and Johnson D 2004 High resolution Thomson scattering for Joint European Torus (JET) Rev. Sci. Instrum. 75 3891–3
[35] Frassinetti L, Beurskens M N A, Scannell R, Osborne T H, Flanagan J, Kempenaars M, Maslov M, Pasqualotto R and Walsh M 2012 Spatial resolution of the JET Thomson scattering system Rev. Sci. Instrum. 83 013506
[36] Lovell J, Reinke M L, Sheikh U A, Sweeney R, Puglia P, Carvalho P and Baylor L 2021 Methods to determine the radiated power in SPI-mitigated disruptions in JET Rev. Sci. Instrum. 92 023502
[37] Lao L L, John H St., Stambaugh R D, Kellman A G and Pfeiffer W 1985 Reconstruction of current profile parameters and plasma shapes in tokamaks Nucl. Fusion 25 1611
[38] Riccardo V, Arnoux G, Collins S, Lomas P, Matthews G, Pace N and Thompson V 2014 Operational impact on the JET ITER-like wall in-vessel components Fusion Eng. Des. 89 1059–63
[39] Matthews G F et al 2016 Melt damage to the JET ITER-like wall and divertor Phys. Scr. 2016 014070
[40] Gerasimov S N et al 2019 Locked mode and disruption in JET-ILW 46th Eur. Phys. Soc. Conf. Plasma Phys. 8–12 P1.1056
[41] Riccardo V, Andrew P, Kaye A and Noll P 2002 Disruption design criteria for JET in-vessel components Proc. 19th IEEE/IPSS Symp. Fusion Eng. 19th SOFE 384–7
[42] ITER 1999 Physics basis, chapter 4 : power and particle control Nucl. Fusion 39 2391–469
[43] Krasheninnikov S, Smolyakov A and Kukushkin A 2020 On the Edge of Magnetic Fusion Devices (Springer Series in Plasma Science and Technology) 978-3-030-49593-0 (https://doi.org/10.1007/978-3-030-49594-7)
[44] Pautasso G et al 2017 Disruption mitigation by injection of small quantities of noble gas in ASDEX upgrade Plasma Phys. Control. Fusion 59 014046
[45] Noll P, Andrew P, Buzio M, Litunovsky R, Rainmondi T, Ricardo V and Verrecchia M 1996 Present understanding of electromagnetic behaviour during disruptions at JET Proc. 19th Symp. Fusion Technol. 16–20
[46] Riccardo V, Noll P and Walker S 2000 Forces between plasma, vessel and TF coils during AVDEs at JET Nucl. Fusion 40 1805–10
[47] Gerasimov S N, Hender T C, Johnson M F and Zakharov L E 2010 Scaling JET disruption sideways forces to ITER 37th Eur. Phys. Soc. Conf. Plasma Phys. 34A, 21–5 P4.121
[48] Myers C E, Eidietis N W, Gerasimov S N, Gerhardt S P, Granetz R S, Hender T C and Pautasso G 2018 A multi-machine scaling of halo current rotation Nucl. Fusion 58 016050
[49] Last J, Bertolini E, Buzio M, Kaye A, Miele P, Noll P, Papastergiou S, Riccardo V, Sannazzaro G and Sjoholm M W R 1999 Raising the JET toroidal field to 4 tesla JET-R(99)10 (https://scipub.euro-fusion.org/archives/jet-archive/raising-the-jet-toroidal-field-to-4-tesla)
[50] Schioler T, Bachmann C, Mazzone G and Sannazzaro G 2011 Dynamic response of the ITER tokamak during asymmetric VDEs Fusion Eng. Des. 86 1963–6
[51] Riccardo V, Walker S and Noll P 2000 Parametric analysis of asymmetric vertical displacement events at JET Plasma Phys. Control. Fusion 42 29–40

[52] Zakharov L E 2008 The theory of the kink mode during the vertical plasma disruption events in tokamaks *Phys. Plasmas* **15** 062507
[53] Riccardo V, Lomas P, Matthews G F, Nunes I, Thompson V and Villedieu E 2013 Design, manufacture and initial operation of the beryllium components of the JET ITER-like wall *Fusion Eng. Des.* **88** 585–9
[54] Jepu I *et al* 2019 Beryllium melting and erosion on the upper dump plates in JET during three ITER-like wall campaigns *Nucl. Fusion* **59** 086009
[55] Lehnen M *et al* 2013 Disruption heat loads and their mitigation in JET with the ITER-like wall *J. Nucl. Mater.* **438** S102–7
[56] Xiong H, Xu G, Wang H, Zakharov L E and Li X 2015 First measurements of Hiro currents in vertical displacement event in tokamaks *Phys. Plasmas* **22** 060702
[57] Artola J Private communication *email to Sergei Gerasimov 2022/09/19*
[58] Schwarz N *et al* 2023 The mechanism of the global vertical force reduction in disruptions mitigated *Nucl. Fusion* **63** 126016
[59] Izzo V A and Parks P B 2010 Comment on 'Plasma current spikes due to internal reconnection during tokamak disruptions *Nucl. Fusion* **50** 058001
[60] Strauss H 2021 Effect of resistive wall on thermal quench in JET disruptions *Phys. Plasmas* **28** 032501
[61] Bardsley O P, Hender T C, Lyons B C, Ferraro N M and Gerasimov S N 2021 Extended-MHD simulations of shattered pellet injection into an Ohmic JET plasma *47th EPS Plasma Physics Virtual Conference* 1 *(21-25 June 2021 UKAEA-CCFE-CP(23) 27* (https://scientific-publications.ukaea.uk/papers/extended-mhd-simulations-of-shattered-pellet-injection-into-an-ohmic-jet-plasma/)
[62] Hu D, Nardon E, Hoelzl M, Wieschollek F, Lehnen M, Huijsmans G T A, van Vugt D C and Kim S-H 2021 Radiation asymmetry and MHD destabilization during the thermal quench *Nucl. Fusion* **61** 026015
[63] Zakharov L E 2010 Reply to comment on 'Plasma current spikes due to internal reconnection during tokamak disruptions *Nucl. Fusion* **50** 058002
[64] Kruezi U *et al* 2009 Massive gas injection experiments at JET - performance and characterisation of the disruption mitigation valve *2009 36th EPS Conf. Plasma Physics, Sofia, Bulg. (29th June–3rd July)* 33 E1, 745–8 (https://scipub.euro-fusion.org/archives/jet-archive/massive-gas-injection-experiments-at-jet-performance-and-characterisation-of-the-disruption-mitigation-valve)
[65] Gebhart T E, Ghiozzi A G, Velez D A, Baylor L R, Chilen C and Meitner S J 2021 Shear strength and release of large cryogenic pellets from the barrel of a shattered pellet injector for disruption mitigation *Fusion Sci. Technol.* **77** 721–7
[66] Gebhart T E, Baylor L R and Meitner S J 2020 Experimental pellet shatter thresholds and analysis of shatter tube ejecta for disruption mitigation cryogenic pellets *IEEE Trans. Plasma Sci.* **48** 1598–605
[67] Gauthier E *et al* 2007 ITER-like wide-angle infrared thermography and visible observation diagnostic using reflective optics *Fusion Eng. Des.* **82** 1335–40
[68] Marot L, Arnoux G, Huber A, Huber V, Mertens P, Sergienko G and Meyer E 2016 Optical coatings as mirrors for optical diagnostics *J. Coat. Sci. Technol.* **2** 72–8
[69] Clever M, Arnoux G, Balshaw N, Garcia-Sanchez P, Patel K, Sergienko G, Soler D, Stamp M F, Williams J and Zastrow K D 2013 A wide angle view imaging diagnostic with all reflective, in-vessel optics at JET *Fusion Eng. Des.* **88** 1342–6
[70] Silburn S *et al* (https://doi.org/10.5281/zenodo.1478554)
[71] Mast K F, Vallet J C, Andelfinger C, Betzler P, Kraus H and Schramm G 1991 A low noise highly integrated bolometer array for absolute measurement of VUV and soft x radiation *Rev. Sci. Instrum.* **62** 744–50
[72] McCormick K, Huber A, Ingesson C, Mast F, Fink J, Zeidner W, Guigon A and Sanders S 2005 New bolometry cameras for the JET enhanced performance phase *Fusion Eng. Des.* **74** 679–83
[73] Murari A, Mast K F, D'Ambra L, Lang P T, Marrelli L, Martin P and Romagnolo A 1995 Multichord calibrated bolometer array for the RFX experiment *Rev. Sci. Instrum.* **66** 665–7
[74] Ingesson L C 1999 Comparison of Methods to Determine the Total Radiated Power in JET *JET-R(99)06* 1–21 (https://scipub.euro-fusion.org/archives/jet-archive/comparison-of-methods-to-determine-the-total-radiated-power-in-jet)
[75] Ferreira D R, Carvalho P J and Fernandes H 2020 Deep learning for plasma tomography and disruption prediction from bolometer data *IEEE Trans. Plasma Sci.* **48** 36–45
[76] Shafranov V D 1967 Electromagnetic waves in a plasma *a Plasma Leontovich M.A. Rev. Plasma Phys. Springer* **3** 1–158
[77] Lohr J 1988 Electron density measurements from cutoff of electron cyclotron emission in the DIII-D tokamak *Rev. Sci. Instrum.* **59** 1608–10
[78] Baranov Y F *et al* 2012 Large ELM-like events triggered by core MHD in JET advanced tokamak plasmas: impact on plasmas profiles, plasma-facing components and heating systems *Nucl. Fusion* **52** 023018
[79] Luhmann N C, Bindslev H, Park H, Sánchez J, Taylor G and Yu C X 2008 Chapter 3: microwave diagnostics *Fusion Sci. Technol.* **53** 335–96
[80] Greenwald M 2002 Density limits in toroidal plasmas *Plasma Phys. Control. Fusion* **44** 1–55
[81] Post D E, Jensen R V, Tarter C B, Grasberger W H and Lokke W A 1977 Steady-state radiative cooling rates for low-density, high-temperature plasmas *At. Data Nucl. Data Tables* **20** 397–439
[82] Hulse R A 1983 Numerical studies of impurities in fusion plasmas *Nucl. Technol.* **3** 259–72